# Ultra-thin intrinsic amorphous silicon (a-Si) hybrid structure with inorganic/organic materials and its applications

by

Jae Yong Lee

A dissertation submitted in partial fulfillment
of the requirements for the degree of
Doctor of Philosophy
(Electrical Engineering)
in the University of Michigan
2014

Doctoral Committee:

Professor L. Jay Guo, Chair
Associate Professor Jinsang Kim
Associate Professor Wei Lu
Professor Jamie D. Phillips

**TO MY FAMILY**

# ACKNOWLEDGEMENTS

First of all, I would like to sincerely express my gratitude to my faculty advisor, Prof. L. Jay Guo, for being such a great mentor and teacher. Encouraged by his guidance and support, I could really enjoy my doctorate research journey and prove myself, as a researcher, to be able to create and study what never existed. He always trusted in me and was patient when I had a hard time failing in a series of experiments. Moreover he provided me with very important insights and suggestions whenever I was puzzled in my life as well as research. Along with supervising my research, he gave me an unforgettable opportunity in practicing and trying to commercialize our technology. That was an epic experience for me, which will eventually guide and shape me to plan my future career more adventurous and exciting. In a nutshell, my PhD years are definitely going to be remembered as not only the happiest, but also the most productive moments, in my life.

I would also like to truthfully thank my committee members, Prof. Jinsang Kim, Prof. Wei Lu, and Prof. Jamie Phillips. They gave me very essential comments when I first proposed my dissertation. Based upon the in-depths remarks, I was able to clarify the unclear explanations of my work. I am grateful that Prof. Kim spent time discussing with me about organic materials and transparent electrodes, which helped me to study them more. I also appreciate that Prof. Lu gave me suggestions regarding device structure and photo-detector characteristics, thus encouraging me to characterize the device more in specific. I remember Prof. Phillips as a teacher as well since he taught me solar cell

devices in a class, which I enjoyed a lot in my first year of PhD. His insightful perspectives on my work directed me to analyze and explain my experimental data better.

If I did not meet with former and present colleagues and friends who I will introduce in the below, I could have not achieved any of my PhD work. Above all, Hui Joon was my senior colleague and mentor when I joined the research group; and he taught me to build my first solar cells. He always motivated me to be a good researcher. Towards blooming my solar cells as decorative power-generating panels, I had a great time working together with Kyu-Tae and Sungyong. We were such an amazing team because we believed that we could make anything work. Jong, Hyoungwon, Moon Kyu, Hongseok, as my senior colleagues, also did not mind discussing with me whenever I had questions and issues regarding my optoelectronic device fabrications. I thank Alex, Drew, Yi-Kuei, Masanori, and Young Jae as well for sharing their idea with me about various possible device designs. I also appreciate Dr. Yan who gave me a chance to get interested in amorphous silicon (a-Si) and try his high quality material in my device structure.

I wish I could spend more time with Ashwin, Taehee, Sangeon, and many other current group members since they are very talented and open-minded researchers, who I would have great time collaborating with. I look forward to having such an opportunity in my future career. My friends, Adrian, Nathan, Kyounghwan, Maesoon, Hyunsoo, and many others who were, and still are, with me at Michigan, made this place to be like home to me, thus helping me to enjoy my life and focus on my research as well. I would like to note that many more people, who I could not list above due to space limit, made my PhD journey exciting. At last, but not least, I dedicate my whole PhD work and dissertation to my family, dad, mom, my sister Jade, and my little two-year old niece

Claire, who make my life full of happiness all the time. Inspired by their full-hearted support and help throughout the years, I could finally complete my PhD journey.

# TABLE OF CONTENTS

# LIST OF FIGURES

## ABSTRACT

# Ultra-thin intrinsic amorphous silicon (a-Si) hybrid structure with inorganic/organic materials and its applications

by

Jae Yong Lee

Chair: L. Jay Guo

The conventional a-Si photovoltaic (PV) has been designed with intrinsic a-Si interfaced with p- and n- type doped layers, total around 40-50 nm. Here, the intrinsic layer needs to be much thicker than the doped layers in order to maximize the conversion of the photogenerated carriers to electric current. Since the dopants, as intentional impurities, annihilate photogenerated carriers, the doped material should be as thin as

possible unless it reduces an internal electric field. Eventually the unwanted carrier recombination with dopants causes light-induced degradation of a-Si PV.

In this dissertation, we present studies suggesting removing dopants in a-Si PV for higher internal quantum efficiency as well as previously undiscovered novel PV applications. We propose intrinsic a-Si hybrid structure with inorganic/organic materials for PVs without any doping. The highest average power conversion efficiency of the a-Si hybrid PV is 6.7% by 180 nm-thick undoped a-Si layer. Its current density-voltage (J-V) curve shows the average short circuit current ($J_{sc}$) of 13.6 mA/cm$^2$, open circuit voltage ($V_{oc}$) of 0.77, and fill factor (FF) of 64 %. We also characterize the hybrid cells by capacitance-voltage (C-V) measurement to identify a built-in potential, from 0.7 V to 0.85 V, according to metal oxide Schottky contact at anode. The built-in potential consequently determines $V_{oc}$ of the hybrid cells.

We exploit the proposed a-Si hybrid device further by running capacitance-frequency (C-f) measurement in order to quantify the interfacial amount of charge annihilation with regard to varied a-Si thicknesses, thereby affecting $V_{oc}$ ranging from 0.6 V to 0.8 V. The $V_{oc}$ change is also evaluated under concentrated sun condition (1 Sun ~ 7 Sun). Since the a-Si hybrid cell shows FF decrease (68 % to 62 %) with increased a-Si thickness (50 nm to 180 nm), we exploit the ambipolar diffusion length (~ 80 nm) by transient photocurrent and photovoltage responses. Notably, we demonstrate the use of the a-Si hybrid cells for decorative colored PV applications by designing a-Si thickness below ~30 nm, even a few nanometers for semi-transparent PVs. We also suggest applying the ultra-thin a-Si hybrid structure for various photo-sensing applications including large area high-speed photo-detectors.

# Chapter 1

# Introduction

## 1.1 Background

Recently, silicon-based photovoltaics (PVs), such as crystalline silicon, poly-silicon, and amorphous silicon, have been deployed in various solar energy generation applications due to attaining competitive power efficiency by relatively low-cost. Among the silicon-based PVs, amorphous silicon (a-Si) PV has been drawn interest in the area of thin-film and flexible applications (Figure 1.1) even though it produces lower power efficiency. Moreover, the a-Si PV has been considered to be scalable in terms of manufacturing with less expensive materials.

For conventional thin-film a-Si PVs, researchers have been working on the optimization of doped a-Si in order to increase its power efficiency [1]-[3]. However the doped a-Si is not a good candidate to reduce the light induced degradation, so called 'Staebler-Wronski effect' [4]-[6], or to manage photons in the photoactive a-Si layer without electric charge annihilation. Reduced a-Si thickness is well known to lessen the light induced degradation; but with the doped layers, the active layer requires the

minimum doped thickness around 40~50 nm [1], which eventually needs several times thicker intrinsic a-Si sandwiched by the doped layers. In terms of the doped layers, there have been a lot of work to determine the thickness of p- and n- doped regions to obtain high enough built-in potential for maximum power efficiency [2]. Thus the doped layers decide the thinnest thickness that the photoactive layer should maintain in conventional p- and n- doped a-Si PVs [7].

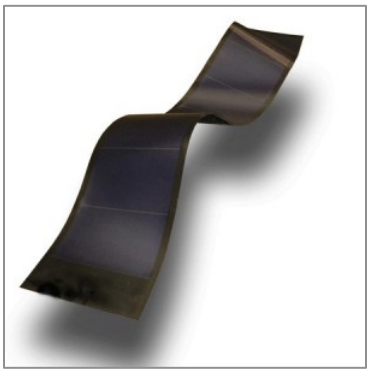

Figure 1.1. Flexible amorphous silicon (a-Si) solar panel generating 68 W electric power. (Source: Former UniSolar, Inc.)

Another drawback by applying the doped layers to a-Si photoactive layer is that the photogenerated charges in the doped layers are subject to be recombined and annihilated by dopants [3]. Since the dopants are just functioning as defects to charge transport processes, the charges generated in the doped regions recombine quickly with the dopants. Regarding photovoltaic devices without doped layers, previously, inorganic n-type crystalline silicon and organic layers (P3HT and PEDOT:PSS) were employed to build hybrid photovoltaic (PV) cells [8], which showed that organic material can effectively work with an inorganic material for photogenerated charge transport. In case of hole extraction process, metal oxide ($MoO_3$) was also exploited for a-Si solar cells

where the other side was n-doped [9]. However, utilizing intrinsic a-Si photoactive layer without any doping for photovoltaics has not been suggested with efficient device structure designs until this study.

## 1.2 Amorphous Silicon (a-Si)

Amorphous silicon (a-Si) has structural defects by deviations in the Si-Si bond lengths and angles, which broaden the electron distribution of states [10]. However the covalent bonds between the silicon atoms are much the same as in crystalline silicon. The disorder causes electron and hole localization as well as carrier scattering as shown in Figure 1.2b. The corresponding electronic states lie in the band gap.

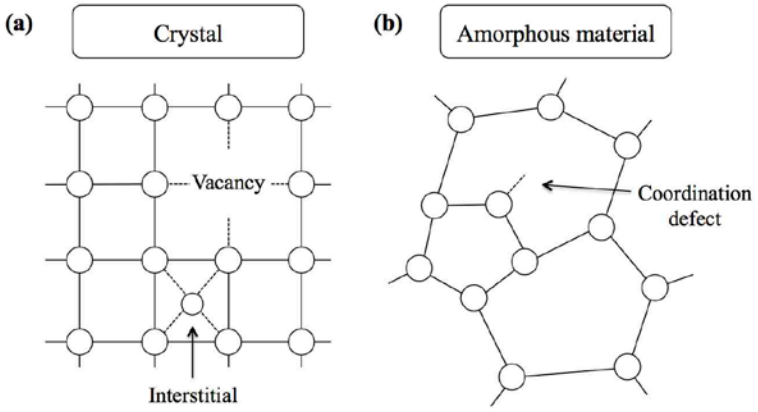


Figure 1.2. An illustration contrasting the different types of simple defects in (a) crystalline and (b) amorphous networks. (Reproduced from ref. [10])

A random network in amorphous silicon structure comprises a specific number of bonds to immediate neighbors, which is called the coordination. Here the Si atom pair distribution function represents the probability of finding an atom at distance R from another atom [10]. Figure 1.3 shows a two-dimensional network with the atoms having different coordination (4, 3, and 1). Even a small concentration of different coordination generates the random network. In Figure 1.2, compared to the crystalline lattice in which impurities are led to have the coordination of the ordered host lattice, amorphous silicon shows distinct difference in the doping and defect properties, in which the elementary defect is the coordination defect.

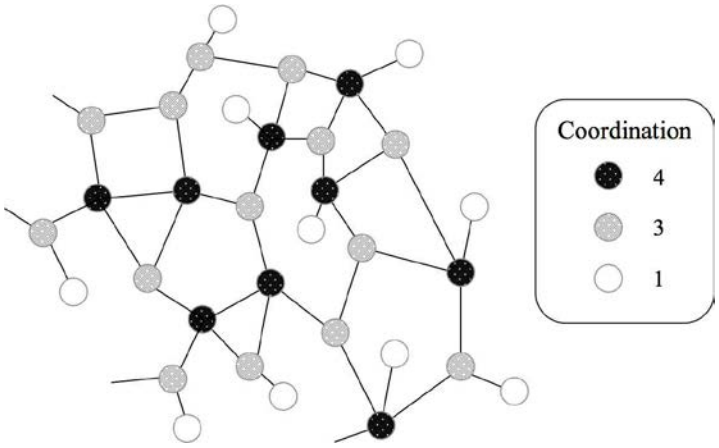


Figure 1.3. An example of a continuous random network containing atoms of different bonding coordination, as indicated. (Reproduced from ref. [10])

Thus, in electronic structure, amorphous silicon has a broadened tail of states extending into the forbidden gap rather than the abrupt band edges of a crystal, which originates from the long-range structural disorder in Figure 1.3. Since electronic transport occurs at the band edge, the band tails play important roles despite their comparably

small concentration. Due to the electronic states deep within the band gap from coordination defects, these defects produce trapping and recombination properties.

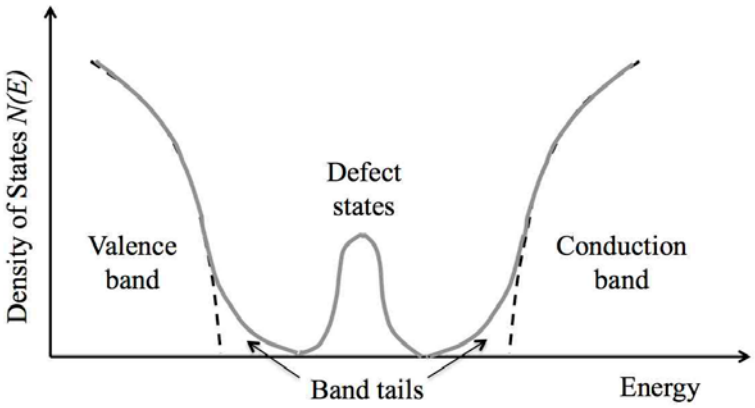


Figure 1.4. Schematic density of states distribution for an amorphous silicon showing the bands, the band tails, and the defect states in the band gap. The dashed curves are the equivalent density of states in a crystal. (Reproduced from ref. [10])

As depicted in Figure 1.4, the amorphous silicon (a-Si) electronic structure comprises the bands, the band tails, and the defect states in the gap [10]. Thus conduction mechanisms are categorized to several ways (Figure 1.5). First, extended state conduction is by thermally activated carriers from the Fermi level to the mobility edge above. Here the separation of the mobility edge from the Fermi level determines the activation energy, which varies from nearly 1 eV in undoped a-Si to 0.1 eV in the n-type. Second, in band tail conduction, hopping from site to site is available at elevated temperatures. Lastly, when the density of states is large enough for electron tunneling, conduction at the Fermi energy occurs, which is known as hopping at the Fermi energy. The hopping states at the Fermi level arise from defects so that the conductivity changes with the defect density. In

order to suppress the Fermi energy hopping conduction, we need to reduce the defect density by adding hydrogen to a-Si empty bonds, called 'dangling bonds' [10].

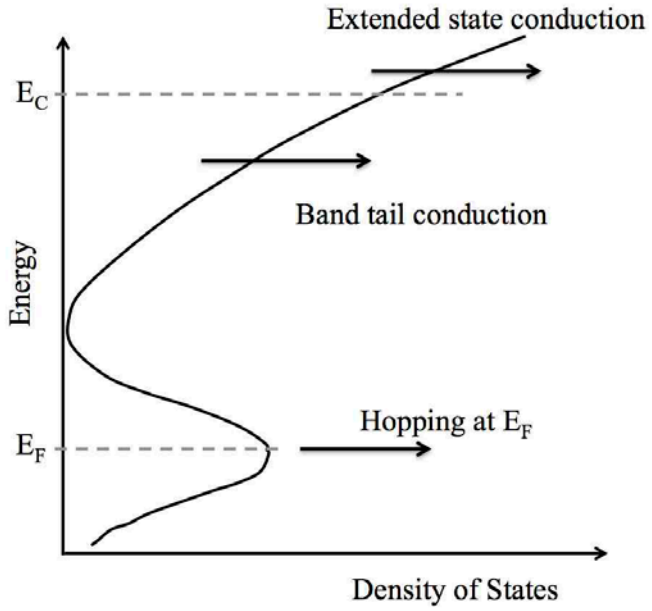


Figure 1.5. Illustration of the three main conduction mechanisms expected in amorphous silicon. (Reproduced from ref. [10])

Although a-Si often has defective conduction, a-Si absorption coefficient is higher than crystalline or microcrystalline silicon above around 2 eV photon energy [2]. The higher coefficient originates from the structural disorder in a-Si material, which 'relaxes' the quantum mechanical selection rules. Mostly the a-Si structural disorder and network is affected by hydrogen content, which is defined at the time of growth during a deposition process. Thus it is well anticipated that the growth condition determines a-Si electronic properties, whose understanding is crucial for the property optimization. Spear and LeComber *et al*. [11] used a silane ($SiH_4$)-based glow discharge generated by radio frequency (RF) voltage in order to prepare a-Si for the first time, which is called plasma

enhanced chemical vapor deposition (PECVD). The 13.56 MHz RF powered PECVD is still widely used for a-Si based materials preparation.

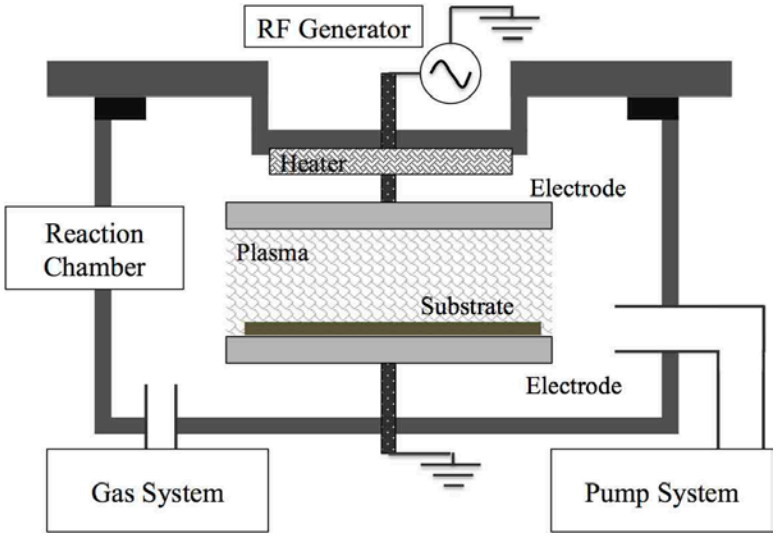


Figure 1.6. Schematic diagram of a typical RF plasma reactor for depositing a-Si. (Reproduced from ref. [2])

A typical RF PECVD chamber and related parts are shown in Figure 1.6 [2]. The RF power is applied between two electrode plates inside of the chamber, into which a silicon containing gas mixture of $SiH_4$ and He flow. In a certain range of gas pressure, plasma gets formed and generates radicals and ions of the gas mixture. As the radicals diffuse on a substrate, a hydrogenated silicon film begins growing. The film growth consists of several steps: source gas diffusion, electron impact dissociation, gas-phase chemical reaction, radical diffusion, and deposition [12]. The deposition conditions need to be well controlled for high quality a-Si. The conditions affect a-Si quality according to the below reasons. First of all, gas pressure determines a mean free path for collisions of the gas molecules; influencing whether the reactions are at the growing surface or in the

gas. Secondly, $SiH_4$ gas flow rate regulates the residence time of the gas species in the reactor: optimum rate can prevent depletion of the gas species. Third, RF power controls the rate of dissociation of the gas, thereby defining both film growth rate and quality. Finally, substrate temperature governs chemical reactions on the growing surface, thus producing hydrogen content ratio from 40 to 8 at%.

Other than hydrogen atoms, the intentional incorporation of atoms like phosphorus and boron in amorphous silicon (a-Si) network, so called 'doping', shifts the Fermi energy of a-Si. The doping process in a-Si works very differently in a-Si than in crystals [2], [10], [12]. Just as is silane, the dopants molecules are dissociated into radicals or ions by the plasma, which bond to the growing surface. For example, n-type doping in a-Si forms both a fourfold coordinated $P_4^+$ and a negatively charged dangling bond $D^-$ very little amount among the most ideal threefold coordinated a-Si [2]. This process does not contribute a "free" electron and the Fermi level shift, leading to very inefficient doping in a-Si. Also, since dopant atom contributing an electron has a dangling bond, defect levels lie in the middle of band gap, which play very negative roles trapping electric charges, especially electrons. As well-balanced bipolar transports of both electrons and holes are essential to complete photovoltaic (PV) energy conversion, the photons absorbed in doped layers do not contribute to electric power generation by solar cells. As we just mentioned, one of major examples of using a-Si in solid-state devices is a solar cell. Therefore understanding how solar cells operate to convert sunlight to electric energy is crucial for designing high-efficiency a-Si based solar cell structures.

## 1.3 Operation of Solar Cells

Let us look at how solar cells operate and potentially what device characteristics the cells need. First of all, solar cell operation determines the most important electric power converting performance of the cell. Here the solar cells provide both a voltage bias and an electric current to the load that usually consumes electric energy. As we anticipate from the electric current and the voltage bias, both electrons and holes need to be provided from the solar cell structure and completed in an outer circuit where the load is mounted. The simplified schematic diagram of very simplified amorphous silicon (a-Si) based solar cells is described in Figure 1.7. The light will be incident on the transparent electrode side and get to the a-Si photoactive layer. The transparent electrode will be employed to conduct one kind of charges, and the other electrode will be used to carry the other kind. In order to transport right sort of charges to respective electrodes, two different charge transport layers play roles for extracting a target charge, but blocking the other charge. The photons absorbed in the a-Si photoactive layer will be converted to both electric charges, if ideal, 100 %.

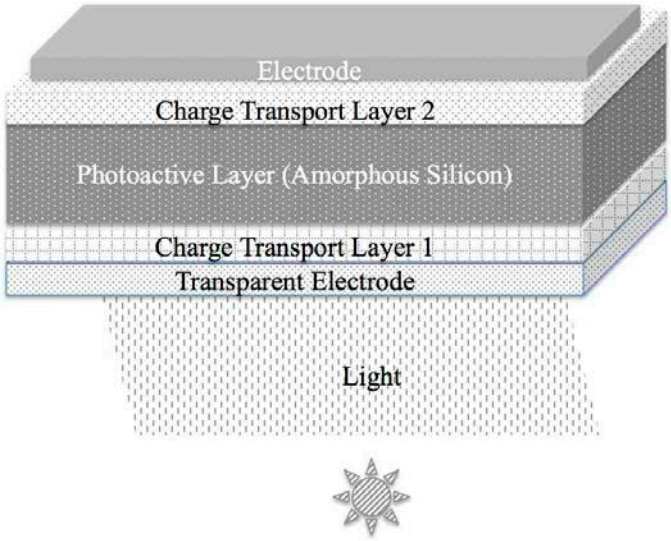


Figure 1.7. Schematic diagram of a simplified a-Si based solar cell.

Based upon the solar cell structure (Figure 1.7), we can model equivalent circuits incorporating diodes under dark and photo conditions as depicted in Figure 1.8. We assume that, under photo condition, a constant current source supplies an electric current to the equivalent circuit, which originates from photogenerated charges in a photoactive layer. Compared to dark condition, the constant current source is the only difference in the circuit model under photo condition, thereby providing Eq. 1.1 in terms of current density (J) in the function of a voltage bias (V). The current density under photo condition is denoted as $J_{photo}$, and dark condition as $J_{dark}$. A short circuit instead of a load induces a short circuit current density ($J_{sc}$) under photo condition.

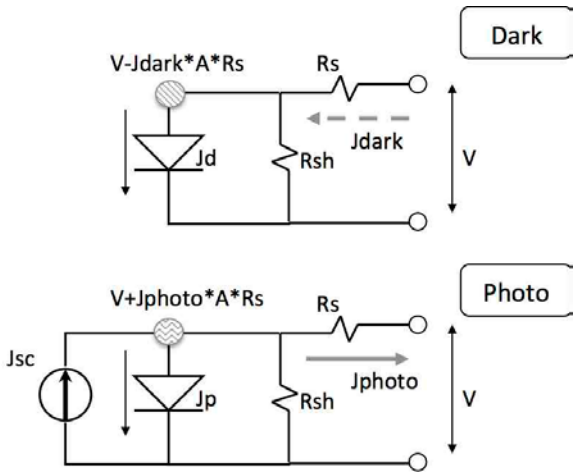


Figure 1.8. Equivalent circuit of solar cell under dark and photo conditions.

$$J_{photo}(V) = J_{sc} - J_{dark}(V) \qquad (1.1)$$

$$J_{dark}(V) = J_0\left(e^{q(V-J_{dark}AR_s)/nkT} - 1\right) + \frac{V-J_{dark}AR_s}{R_{sh}} \qquad (1.2)$$

$$J_{photo}(V) = J_{sc} - \left\{J_0\left(e^{q(V+(J_{photo}-J_{dark})AR_s)/nkT} - 1\right) + \frac{V+(J_{photo}-J_{dark})AR_s}{R_{sh}}\right\} \qquad (1.3)$$

The current densities under dark and photo conditions are expressed in Eq. 1.2 and 1.3, respectively, where $J_0$ is the saturation current density, q the elementary charge, A the solar cell area, $R_s$ the series resistance, $R_{sh}$ the shunt resistance, n the diode ideality factor, and kT the average kinetic energy. Ideally, we design solar cells to have as large shunt resistance and small series resistance as possible in order to maximize the current density versus a voltage bias (V). Figure 1.9 illustrates that how a current density (J) performs according to a voltage (V) under photo condition, which originates from Eq. 1.3. The y-axis cross of the J-V curve represents short circuit current density ($J_{sc}$), and the x-axis cross of the curve indicates open circuit voltage ($V_{oc}$).

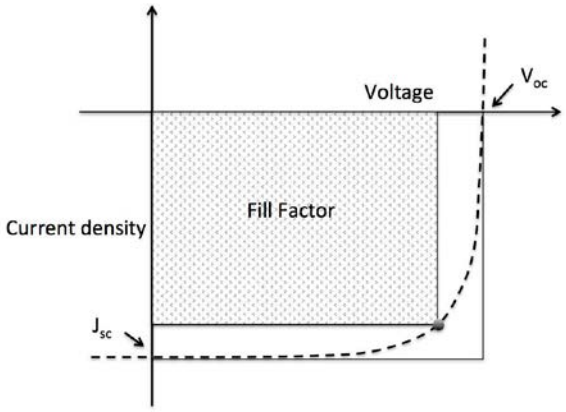


Figure 1.9. Current density-voltage (J-V) characteristics of solar cell.

In order to enhance the solar cell performance, we should maximize the $J_{sc}$ and $V_{oc}$ by designing the cell structure accordingly. The $V_{oc}$ is determined from Eq. 1.4: for example, ideally, a larger photo current density is beneficial for a larger $V_{oc}$. However, due to the J-V diode curve, the maximum power generation point by J multiplied by V is a partial area defined by $J_{sc}$ and $V_{oc}$ as described in Figure 1.9. Here the area ratio is called fill factor, which is calculated by Eq. 1.5. In reality, since we have series resistance ($R_s$) and shunt resistance ($R_{sh}$) that affect slopes at x-axis and y-axis, respectively, those resistances affect the fill factor (FF). The slope change and FF decrease are depicted in Figure 1.10, thus reducing the power conversion efficiency as calculated in Eq. 1.6 where $P_{in}$ implies total input power by AM1.5 sunlight spectrum.

$$V_{oc} = \frac{nkT}{q} ln\left(\frac{J_{photo}}{J_0} + 1\right) \qquad (1.4)$$

$$FF = \frac{J_{mp}V_{mp}}{J_{sc}V_{oc}} \qquad (1.5)$$

$$\eta = \frac{P_{max}}{P_{in}} = \frac{J_{mp}V_{mp}}{P_{in}} = \frac{J_{sc}V_{oc}FF}{P_{in}} \qquad (1.6)$$

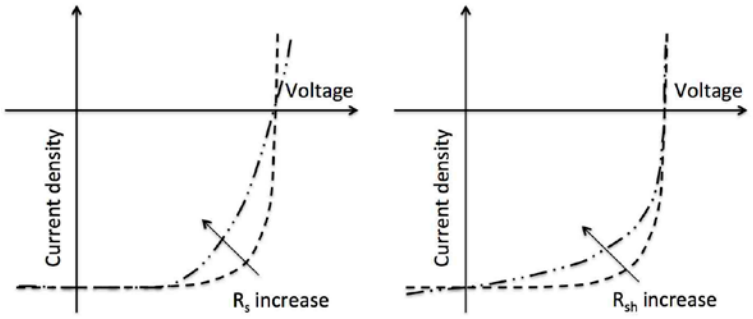


Figure 1.10. Negative effect of (a) series resistance ($R_s$) increase and (b) shunt resistance ($R_{sh}$) increase on power conversion efficiency as well as J-V characteristics of solar cell.

The power conversion efficiency decomposes to external quantum efficiency (EQE) according to the wavelength of absorbed light as shown in Figure 1.11. The dashed line depicts the absorption of photoactive layer, which is mostly larger than EQE since the absorbed photons are not always converted to electron hole charges eventually completed for an electric current in the solar cell structure. At certain wavelength, if we assume charge transport in peripheral circuit is ideal enough to carry all electric charges without loss, we define internal quantum efficiency (IQE) to be the ratio of EQE versus photoactive layer absorption as detailed in Eq. 1.7. If solar cell structure is ideal harvesting every single photon to a complete charge pair, we expect perfect IQE of 100 %. In the next chapter, we will study how amorphous silicon solar cells have been developed in order to address the key factors of the cell operation for power efficiency enhancement, which we introduced above.

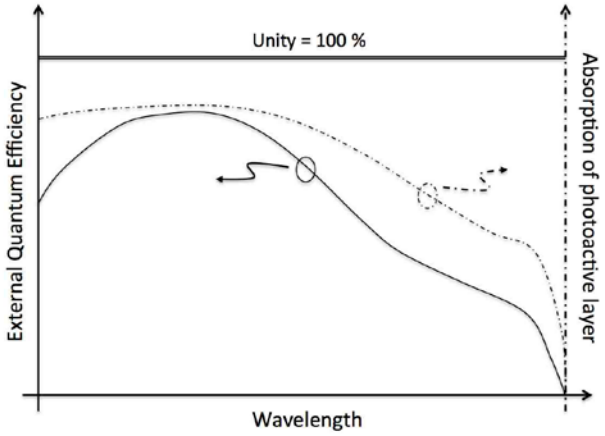


Figure 1.11. Exemplified illustration of External Quantum Efficiency (EQE) and absorption of photoactive layer versus the wavelength of incident light on solar cell.

$$EQE = (Absorption) \times (IQE) \times (Charge\ Transport) \qquad (1.7)$$

## 1.4 Amorphous Silicon (a-Si) Solar Cells

Amorphous silicon (a-Si) solar cells have been designed in various structures to enhance power conversion efficiency [2], [3], [10], [13], [14]. As shown in Figure 1.12, a-Si is p- and n- type doped for p-i-n photodiode including intrinsic (i-) a-Si sandwiched by the doped layers. When a photon is incident to the photodiode, an electron-hole charge pair gets generated, separated, and swept to the respective electrodes through n- and p-doped regions. The p-i-n photodiode based a-Si solar cells have photons incoming from a transparent electrode and p-type doped layer, which is called 'window' layer (Figure 1.12) [2]. The a-Si solar cells are divided two types according to how they are structured according to where glass substrates are located: 'superstrate' and 'substrate' as depicted

in Figure 1.12. Most a-Si solar cell structures have back reflectors so that they can harvest more photons in a-Si photoactive layers [2], [3], [14].

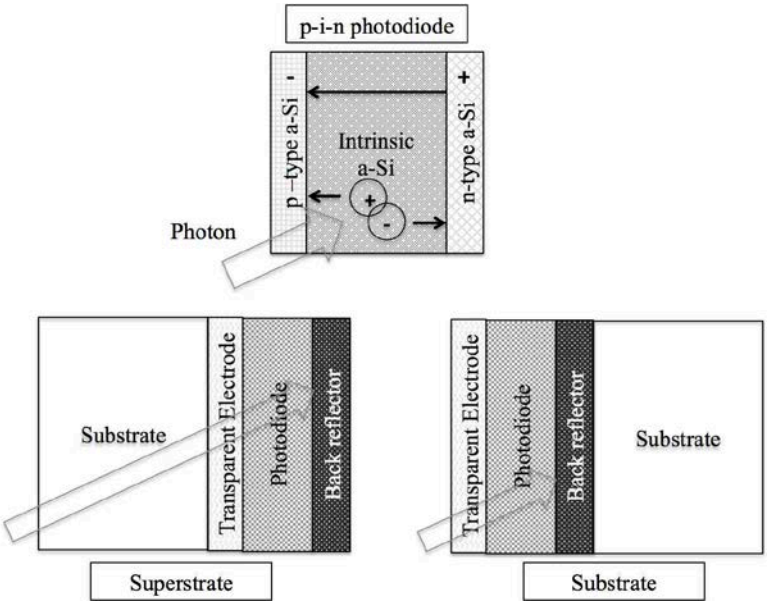


Figure 1.12. p-i-n a-Si structures are incorporated into solar cells in either the superstrate or substrate designs. For a-Si based cells, photons enter through the p-type layer. (Reproduced from ref. [2])

In addition, a-Si photovoltaic (PV) devices are also designed to have 'tandem' structures, which have multiple photoactive materials with different bandgaps [2]. Figure 1.13 shows an example of double photoactive materials (a-Si and a-SiGe) to broaden light absorption, and consequently enhance short circuit current and power efficiency of the a-Si based thin-film PVs. Same as the single layer a-Si cells, the tandem structure has p- and n- doped layers to extract electric charges efficiently from the individual photoactive layer. A transparent electrode also needs to be incorporated in the tandem device. The direction of electric field in the double junctions of the tandem cells should be same in order to maintain and accumulate the flow of electric charges (Figure 1.13).

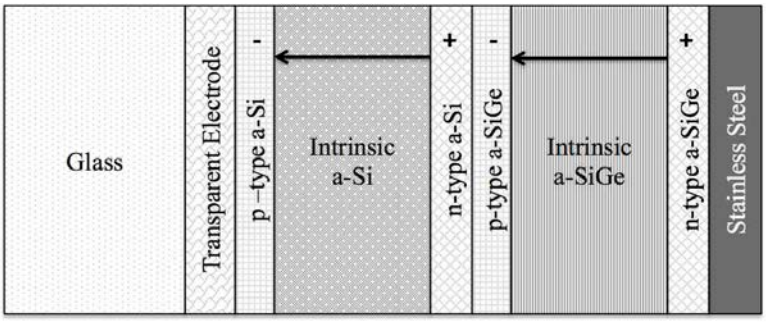


Figure 1.13. A multi-junction solar cell consisting of two p-i-n solar cells deposited in series. Double-junction (or 'tandem' as shown) and triple-junction designs can be significantly more efficient than single-junction designs. (Reproduced from ref. [2])

Amorphous silicon PV researchers also have been working on bandgap engineering of a-Si based materials for modifying bandgaps as described in Figure 1.14 [13]. Here indium-tin oxide (ITO) is used for a transparent electrode through which photons enter into the triple-junction of p-i-n photoactive layers. The first layer is designed to absorb high-energy photons by having largest bandgap. In contrast, the last layer, which is close to a reflector (Ag in this case), has smallest bandgap to harvest the rest of photons not absorbed in the previous junctions. Notably zinc oxide (ZnO) is utilized for an interfacial layer transporting electrons to Ag from the triple-junction. We will introduce more about charge transport materials in Chapter 1.5. In the a-Si based multiple-junction solar cell structures, harvesting similar amount of electric charges in each layer is critical as the electric current from each layer should be well balanced for non-compromised total electric current all throughout the photoactive layers [15], [16].

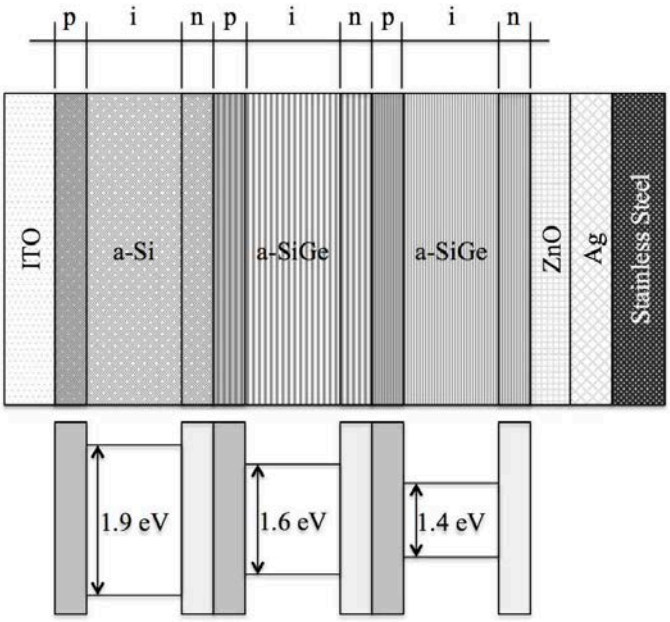


Figure 1.14. Structure of triple-junction p-i-n substrate-type a-Si solar cells. For electron transport, zinc oxide (ZnO) is often used for a-Si solar cells. (Reproduced from ref. [2])

Even if we can enhance the power conversion efficiency of the a-Si based PV cells, there is a potential drawback of multiple photoactive junctions, which is light-induced degradation of a-Si PV in application fields [4], [17], [18]. The power efficiency gradually decreases by up to 15-20 % after being installed in the fields [18]. This is because the unwanted recombination of the generated electric charges in photoactive layer breaks the amorphous bonds in Figure 1.3b [2]. This will cause to generate more dangling bonds that will eventually act as trap sites for newly generated charges. The light-induced degradation is called 'Staebler-Wronski effect' according to their first report [4]. In order to reduce the unavoidable power efficiency decrease, researchers have been trying to minimize the doped layers of a-Si PVs where photogenerated charges get annihilated by intentional dopants [19]. By optically and electrically coupled modeling, they can minimize light absorption in doped regions, which previously turned out not to

contribute electric current generation. Additionally, in order to further increase power efficiency, nanostructured substrates have been recently investigated to enhance the light trapping in a-Si photoactive layers with various transparent charge transport materials combined [19]-[25]. For example, by introducing zinc oxide (ZnO) that is a charge transport material for extracting electrons very efficiently as well as forming nanostructures, high power efficiency a-Si solar cell can be achieved [26]. In the next chapter, we will introduce various types of charge transport layers to study if the materials are appropriate to potentially work with a-Si photoactive layer efficiently.

## 1.5 Charge Transport Layers

Various charge transport materials have been more extensively utilized for organic electronics than a-Si based electronic devices since organic materials are not apt to be doped to form an electric field in a photoactive region [27]. Thus, in this chapter, we will look into a variety of material options for transporting and extracting photogenerated charges in a desirable way. Figure 1.15 depicts the schematic diagrams of the two basic PV structures incorporating organic photoactive materials and respective charge transport layers for electrons and holes [28]. Both structures have a transparent electrode and a metal back reflector, by which photons are guided into photoactive layers effectively. The choice of the structure depends on specific device design and electric charge transport efficiency [29]-[31]. Next we will study what will be important properties of charge transport materials and their roles in solar cells.

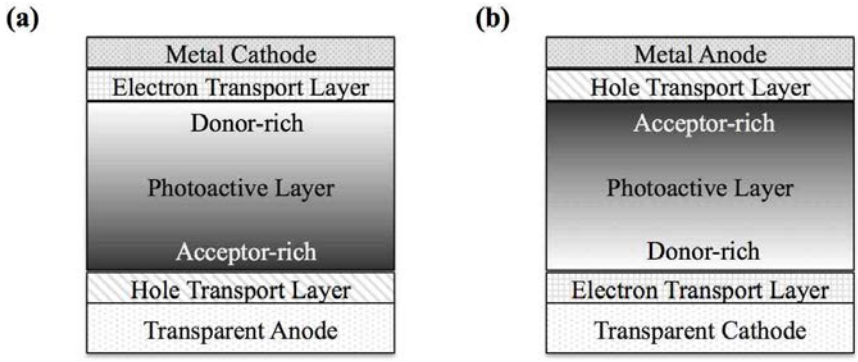


Figure 1.15. Schematic illustration of organic photoactive layers with hole and electron selective layers in (a) conventional organic PV (OPV) and (b) inverted OPV. (Reproduced from ref. [28])

As we search for charge transport materials that can transport electrons and holes selectively, we are encouraged to look at band energy diagrams of the transport materials in Figure 1.16, which are picked from (Yip *et al*.) for possible combination with a-Si [28]. The hole transport materials of PEDOT:PSS [32], graphene oxide [33], nickel oxide ($NiO_x$) [30], and molybdenum oxide ($MoO_3$) [34], having comparable valence energy level to a-Si valence band, can work for extracting hole charges. On the opposite, electron charges can be transported by Indene-$C_{60}$ Bisadduct (ICBA) [35], [6,6]-phenyl-C-61-butyric acid methyl ester (PCBM) [36], titanium oxide ($TiO_2$) [37], and zinc oxide (ZnO) [38]. The hole and electron transport materials should be selective on the charge transport, blocking the other charge efficiently, so that the charges flow to anode and cathode, respectively. The selective bidirectional charge transport will mitigate unwanted bimolecular recombination, thereby enhancing power efficiency [39].

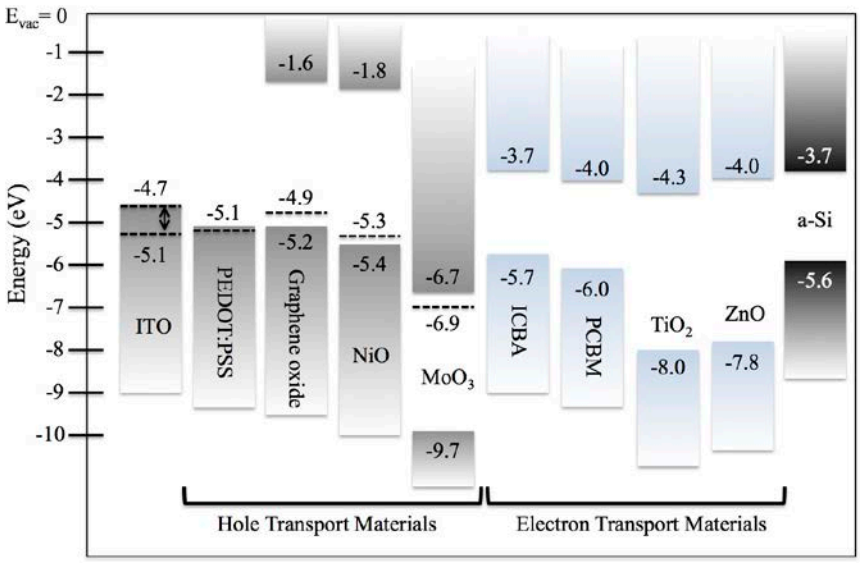


Figure 1.16. Schematic view of the energy gaps and energy levels of several hole and electron transport materials. The dotted lines correspond to the work functions of the materials. (Reproduced from ref. [28])

Figure 1.17 shows the expanded use of charge transport materials to various photoactive materials, for example amorphous/nano-crystalline silicon, organic light absorbing material, and even dyes [40], [41]. Here the most important material selection rule is to design and deposit efficient materials by energy band engineering according to the above introduction [42]. There are various ways for depositing charge transport materials [43]-[46]. The RF powered sputtering method for inorganic materials [44], thermal/e-beam evaporation for both inorganic and organic materials [45], and solution casting process for both ones as well [46], etc. The deposition method is determined by the fabrication restriction factor according to the properties of materials used, substrate handling, surface morphology, and many others.

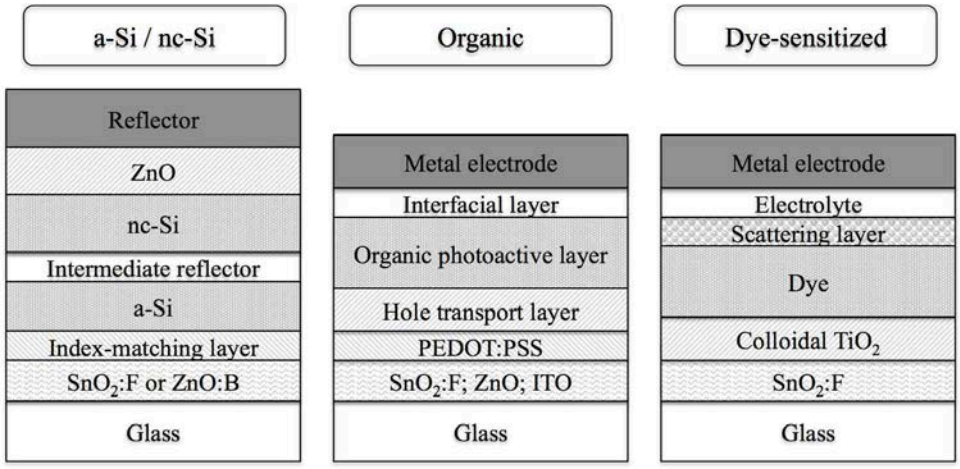


Figure 1.17. The principal types of solar cells that utilize one or more charge transport materials as well as transparent electrodes in their structures. (Reproduced from ref. [40])

We have taken a look at various charge transport materials and their roles in PV devices incorporating a variety of photoactive layers. Here the charge transport materials will always be interfaced with transparent electrodes where light gets through to photoactive layer with minimized photon loss. Thus we need highly transparent electrically conducting layer in the target wavelength, which photoactive material is designed to absorb. However, for the most time, it is challenging to satisfy both optical transparency and electric conductivity to maximize PV power conversion efficiency.

## 1.6 Transparent Electrodes

Transparent conductive electrodes play important roles in optoelectronic devices by transmitting light, mostly in the visible spectral range, and conducting electrical current simultaneously [47]. With the advent of flat-panel display technology, indium-tin

oxide has been widely used for transparent electrodes. However, the increasing demand and cost of raw materials, especially indium, have been encouraging researchers to seek alternatives. Recently various types of transparent electrodes have been designed and implemented for optoelectric solid-state devices: the schematic structures of newly developed electrodes are shown in Figure 1.18 [47]. The current transparent electrodes are mostly categorized in these: the single layer of transparent conductive oxide (TCO) or ultra-thin metal [48]-[52], the dielectric/metal/dielectric multiple layers [53]-[58], periodic metal grid [59], [60], and metal nanowire or carbon nanotube network [61]-[63].

Tobias Schwab *et al.* achieved sheet resistance of 20 Ω/□ and average optical transmittance of 65 % in the 400 to 750 nm spectral range with 5 nm single Ag layer on top of 2 nm Au wetting layer [50]. Similar work was done by Kung-Shih Chen *et al*. by introducing a organic wetting layer of bis-$C_{60}$ salt with ultra-thin Ag [49]: here they also studied a microcavity effect to maximize light absorption in a photoactive layer. In dielectric/metal/dielectric transparent electrode configurations, several dielectric materials have been used: molybdenum oxide [53]-[56], vanadium oxide [57], and tungsten oxide [58]. By utilizing molybdenum oxide and 9 nm Ag, Baolin Tian *et al*. attained maximum transmittance of 80 % in the 400-700 nm, and a low sheet resistance of 9 Ω/□ [56]. With vanadium oxide and 13 nm Ag, Liang Shen *et al*. accomplished maximum transmittance of 90 % in the 400-700 nm range by having 10 and 40 nm vanadium oxides to sandwich the Ag layer [57].

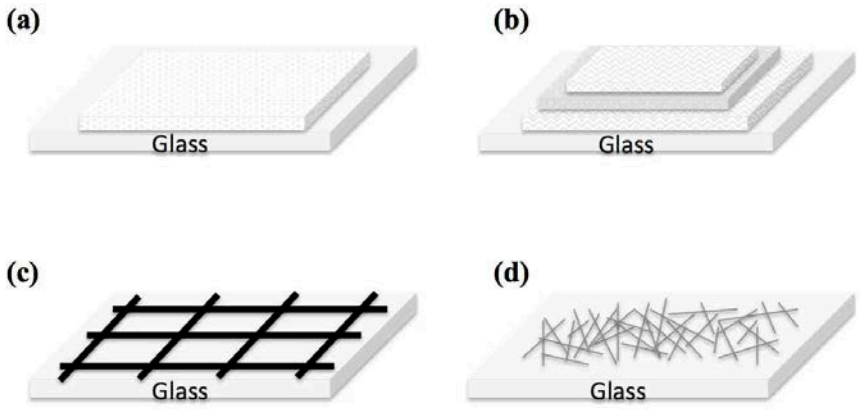


Figure 1.18. Schematic structures of different transparent electrodes on flat glass substrates. (a) Single transparent conductive oxide or metal film, (b) Dielectric/metal/dielectric layer stack, (c) Periodic metal grid, and (d) Metal nanowire (carbon nanotube) network. (Reproduced from ref. [47])

In Figure 1.18, the continuous film deposition of (a) and (b) structures is relatively simpler than the periodic metal grid patterning in (c). Myung-Gyu Kang *et al*. reported above 80 % transmittance throughout from 400 nm to 800 nm and sheet resistance of about 12 Ω/□ by utilizing Cu and Au metal grid with 70 nm line-width and 40 nm thickness [59]. Jorik van de Groep *et al*. achieved even higher maximum transmittance of 91 % and lower sheet resistance of 6.5 Ω/□ using Ag network; they also investigated the excitation of localized surface plasmons on the wires in order to provide metal grid design guidelines [60]. Alternatives to the periodic metal grids have been also studied by introducing the network carbon nanotubes or metal nanowires as shown in Figure 1.18d. Hui Wu *et al*. suggested metal nanotrough networks reaching transmittance of over 80 % in the range 400-1200 nm having sheet resistance around 15 Ω/□ with Cu, Au, and Al nanotrough produced by electrospinning [61]. Yeonwoong Jung *et al*. studied that high-quality metallic single-walled carbon nanotubes (SWNT) were used instead with n-type crystalline silicon (c-Si) to form metal-semiconductor Schottky junction,

thereby leading to over 11 % power conversion efficiency [63]. The solution-processed SWNT network, transferred on top of c-Si as a film, was utilized as another type of transparent electrode.

Based on the above studies, we started wondering if the conventional a-Si solar cells are really ideal structures for converting absorbed photons to electric charges. We also got curious about where the most electric charge loss happens in the a-Si photoactive layer. We believe that how we can reduce the undesirable charge loss will lead us to pursue higher power conversion efficiency eventually. Furthermore the more efficient photon management in the a-Si solar cells is anticipated to open up the novel use of a-Si PVs in various applications once we design a simple but versatile a-Si PV structure.

## 1.7 Outline of Dissertation

In order to develop the idea of new a-Si based devices further from the introductory studies; the outline of my dissertation is organized as follows. Chapter 2 describes the energy band diagram and PV performance of proposed a-Si structure. In order to address the above challenges of a-Si PV, we have been building ultra-thin a-Si PVs without doping, hybrid with efficient electron and hole transport layers instead, organic and inorganic materials, respectively. In Chapter 3, we analyze the electrical performance of the undoped a-Si hybrid device regarding open circuit voltage change and transient photo-response. We have also proposed the a-Si hybrid PV structure for decorative PV applications as well. Chapter 4 introduces various decorative PV

applications, which have been possible due to the unique structure of the proposed a-Si hybrid PVs. Alongside the effort to create the new functionality of a-Si hybrid PVs, as introduced in Chapter 5, we have been working on enhancing the power conversion efficiency of proposed PV device by utilizing nanostructured substrate. Lastly, Chapter 6 suggests that the ultra-thin a-Si device can be a very effective structure for various photo-sensing applications including large area high-speed photo-detectors.

# References


[1] E. A. Schiff, "Low-mobility solar cells: a device physics primer with application to amorphous silicon," *Solar Energy Materials and Solar Cells*, vol. 78, no. 1, pp. 567–595, Jul. 2003.

[2] X. Deng and E. A. Schiff, "Amorphous Silicon–based Solar Cells," *Handbook of Photovoltaic Science and Engineering (Edited by A. Luque and S. Hegedus)*, pp. 505–565, Mar. 2003.

[3] A. V. Shah, H. Schade, M. Vanecek, J. Meier, E. Vallat-Sauvain, N. Wyrsch, U. Kroll, C. Droz, and J. Bailat, "Thin-film silicon solar cell technology," *Prog. Photovolt: Res. Appl.*, vol. 12, pp. 113–142, 2004.

[4] D. L. Staebler and C. R. Wronski, "Reversible conductivity changes in discharge-produced amorphous Si," *Appl. Phys. Lett.*, vol. 31, no. 4, p. 292, 1977.

[5] H. M. Branz, "Hydrogen collision model: Quantitative description of metastability in amorphous silicon," *Phys. Rev. B*, vol. 59, no. 8, pp. 5498–5512, 1999.

[6] D. E. Carlson and C. R. Wronski, "Amorphous silicon solar cell," *Appl. Phys. Lett.*, vol. 28, no. 11, p. 671, 1976.

[7] T. Söderström, F. J. Haug, X. Niquille, and C. Ballif, "TCOs for nip thin film

silicon solar cells," *Prog. Photovolt: Res. Appl.*, vol. 17, no. 3, pp. 165–176, May 2009.

[8] S. Avasthi, S. Lee, Y.-L. Loo, and J. C. Sturm, "Role of Majority and Minority Carrier Barriers Silicon/Organic Hybrid Heterojunction Solar Cells," *Adv. Mater.*, vol. 23, no. 48, pp. 5762–5766, Nov. 2011.

[9] S. Il Park, S. Jae Baik, J.-S. Im, L. Fang, J.-W. Jeon, and K. Su Lim, "Towards a high efficiency amorphous silicon solar cell using molybdenum oxide as a window layer instead of conventional p-type amorphous silicon carbide," *Appl. Phys. Lett.*, vol. 99, no. 6, p. 063504, 2011.

[10] R. A. Street, *Hydrogenated Amorphous Silicon*. Cambridge: Cambridge University Press, 2010.

[11] W. E. Spear and P. G. Le Comber, "Investigation of the localised state distribution in amorphous Si films," *Journal of Non-Crystalline Solids*, vol. 8-10, pp. 727–738, 1972.

[12] E. A. Schiff, S. Hegedus, and X. Deng, "Chapter 12. Amorphous Silicon-based Solar Cells," *Handbook of Photovoltaic Science and Engineering, 2nd Edition (Edited by A. Luque and S. Hegedus)*, pp. 487–505, 2011.

[13] M. Zeman, "Chapter 7. Thin-film Si solar cells," pp. 1–30, Jun. 2006.

[14] C.-H. Yang, C.-Y. Hsueh, D.-J. Yeh, C.-I. Ho, C.-M. Leu, Y.-H. Yeh, and S.-C. Lee, "Hydrogenated Amorphous Silicon Solar Cells on Textured Flexible Substrate Copied From a Textured Glass Substrate Template," *IEEE Electron Device Lett.*, vol. 32, no. 9, pp. 1254–1256.

[15] F. J. Haug, T. Söderström, M. Python, V. Terrazzoni-Daudrix, X. Niquille, and C. Ballif, "Development of micromorph tandem solar cells on flexible low-cost plastic substrates," *Solar Energy Materials and Solar Cells*, vol. 93, no. 6, pp. 884–887, Jun. 2009.

[16] T. Söderström, F. J. Haug, V. Terrazzoni-Daudrix, and C. Ballif, "Flexible micromorph tandem a-Si/μc-Si solar cells," *J. Appl. Phys.*, vol. 107, no. 1, p. 014507, 2010.

[17] S. Guha, "On light-induced effect in amorphous hydrogenated silicon," *J. Appl. Phys.*, vol. 52, no. 2, p. 859, 1981.

[18] D. E. Carlson, K. Rajan, and D. Bradley, "Irreversible light-induced degradation in amorphous silicon solar cells," *26th IEEE PVSC,* pp. 595–598, 1997.

[19] M. G. Deceglie, V. E. Ferry, A. P. Alivisatos, and H. A. Atwater, "Design of Nanostructured Solar Cells Using Coupled Optical and Electrical Modeling," *Nano Lett.*, vol. 12, no. 6, pp. 2894–2900, Jun. 2012.

[20] H. Tan, R. Santbergen, A. H. M. Smets, and M. Zeman, "Plasmonic Light Trapping in Thin-film Silicon Solar Cells with Improved Self-Assembled Silver Nanoparticles," *Nano Lett.*, vol. 12, no. 8, pp. 4070–4076, Aug. 2012.

[21] X. Chen, B. Jia, J. K. Saha, B. Cai, N. Stokes, Q. Qiao, Y. Wang, Z. Shi, and M. Gu, "Broadband Enhancement in Thin-Film Amorphous Silicon Solar Cells Enabled by Nucleated Silver Nanoparticles," *Nano Lett.*, vol. 12, no. 5, pp. 2187–2192, May 2012.

[22] C. Battaglia, C.-M. Hsu, K. Söderström, J. Escarré, F.-J. Haug, M. Charrière, M. Boccard, M. Despeisse, D. T. L. Alexander, M. Cantoni, Y. Cui, and C. Ballif, "Light Trapping in Solar Cells: Can Periodic Beat Random?," *ACS Nano*, vol. 6, no. 3, pp. 2790–2797, Mar. 2012.

[23] Y. Wang, T. Sun, T. Paudel, Y. Zhang, Z. Ren, and K. Kempa, "Metamaterial-Plasmonic Absorber Structure for High Efficiency Amorphous Silicon Solar Cells," *Nano Lett.*, vol. 12, no. 1, pp. 440–445, Jan. 2012.

[24] V. E. Ferry, M. A. Verschuuren, M. C. V. Lare, R. E. I. Schropp, H. A. Atwater, and A. Polman, "Optimized Spatial Correlations for Broadband Light Trapping Nanopatterns in High Efficiency Ultrathin Film a-Si:H Solar Cells," *Nano Lett.*, vol. 11, no. 10, pp. 4239–4245, Oct. 2011.

[25] C. Battaglia, J. Escarré, K. Söderström, M. Charrière, M. Despeisse, F.-J. Haug, and C. Ballif, "Nanomoulding of transparent zinc oxide electrodes for efficient light trapping in solar cells," *Nature Photonics*, vol. 5, no. 9, pp. 535–538, Aug. 2011.

[26] C. Battaglia, J. Escarré, K. Söderström, L. Erni, L. Ding, G. Bugnon, A. Billet, M. Boccard, L. Barraud, S. De Wolf, F.-J. Haug, M. Despeisse, and C. Ballif, "Nanoimprint Lithography for High-Efficiency Thin-Film Silicon Solar Cells," *Nano Lett.*, vol. 11, no. 2, pp. 661–665, Feb. 2011.

[27] H. Ma, H.-L. Yip, F. Huang, and A. K. Y. Jen, “Interface Engineering for Organic Electronics,” *Adv. Funct. Mater.*, vol. 20, no. 9, pp. 1371–1388, Apr. 2010.

[28] H.-L. Yip and A. K. Y. Jen, “Recent advances in solution-processed interfacial materials for efficient and stable polymer solar cells,” *Energy Environ. Sci.*, vol. 5, no. 3, pp. 5994–6011, 2012.

[29] C.-H. Chou, W. L. Kwan, Z. Hong, L.-M. Chen, and Y. Yang, “A Metal-Oxide Interconnection Layer for Polymer Tandem Solar Cells with an Inverted Architecture,” *Adv. Mater.*, vol. 23, no. 10, pp. 1282–1286, Sep. 2010.

[30] Z. Y. Wang, S.-H. Lee, D.-H. Kim, J.-H. Kim, and J.-G. Park, “Effect of NiOx thin layer fabricated by oxygen-plasma treatment on polymer photovoltaic cell,” pp. 1–6, Jul. 2010.

[31] J. Zou, H.-L. Yip, Y. Zhang, Y. Gao, S.-C. Chien, K. O'Malley, C.-C. Chueh, H. Chen, and A. K. Y. Jen, “High-Performance Inverted Polymer Solar Cells: Device Characterization, Optical Modeling, and Hole-Transporting Modifications,” *Adv. Funct. Mater.*, vol. 22, no. 13, pp. 2804–2811, Mar. 2012.

[32] B. Friedel, P. E. Keivanidis, T. J. K. Brenner, A. Abrusci, C. R. McNeill, R. H. Friend, and N. C. Greenham, “Effects of Layer Thickness and Annealing of PEDOT:PSS Layers in Organic Photodetectors,” *Macromolecules*, vol. 42, no. 17, pp. 6741–6747, Sep. 2009.

[33] Y. Gao, H.-L. Yip, S. K. Hau, K. M. O'Malley, N. C. Cho, H. Chen, and A. K. Y. Jen, “Anode modification of inverted polymer solar cells using graphene oxide,” *Appl. Phys. Lett.*, vol. 97, no. 20, p. 203306, 2010.

[34] M. Kröger, S. Hamwi, J. Meyer, T. Riedl, W. Kowalsky, and A. Kahn, “Role of the deep-lying electronic states of MoO[sub 3] in the enhancement of hole-injection in organic thin films,” *Appl. Phys. Lett.*, vol. 95, no. 12, p. 123301, 2009.

[35] Y. He, H.-Y. Chen, J. Hou, and Y. Li, “Indene−C 60Bisadduct: A New Acceptor for High-Performance Polymer Solar Cells,” *J. Am. Chem. Soc.*, vol. 132, no. 4, pp. 1377–1382, Feb. 2010.

[36] S. K. Hau, K. M. O'Malley, Y.-J. Cheng, H.-L. Yip, H. Ma, and A. K. Y. Jen,

"Optimization of Active Layer and Anode Electrode for High-Performance Inverted Bulk-Heterojunction Solar Cells," *IEEE J. Select. Topics Quantum Electron.*, vol. 16, no. 6, pp. 1665–1675.

[37] G. Kron, T. Egerter, J. H. Werner, and U. Rau, "Electronic Transport in Dye-Sensitized Nanoporous TiO2 Solar Cells Comparison of Electrolyte and Solid-State Devices," *J. Phys. Chem. B*, vol. 107, no. 15, pp. 3556–3564, Apr. 2003.

[38] J. Loffler, R. Groenen, J. L. Linden, M. C. M. van de Sande, and R. E. I. Schropp, "Amorphous silicon solar cells on natively textured ZnO grown by PECVD," *Thin Solid Films*, vol. 392, pp. 315–319, 2001.

[39] B. C. O'Regan and F. Lenzmann, "Charge Transport and Recombination in a Nanoscale Interpenetrating Network of n-Type and p-Type Semiconductors: Transient Photocurrent and Photovoltage Studies of TiO 2/Dye/CuSCN Photovoltaic Cells," *J. Phys. Chem. B*, vol. 108, no. 14, pp. 4342–4350, Apr. 2004.

[40] A. E. Delahoy and S. Guo, "Chapter 17. Transparent Conducting Oxides for Photovoltaics," *Handbook of Photovoltaic Science and Engineering, 2nd Edition (Edited by A. Luque and S. Hegedus)*, pp. 716–796, 2011.

[41] M. Grätzel, "Recent Advances in Sensitized Mesoscopic Solar Cells," *Acc. Chem. Res.*, vol. 42, no. 11, pp. 1788–1798, Nov. 2009.

[42] J. Y. Lee, T. Lee, H. J. Park, and L. J. Guo, "Improved solar cell performance by adding ultra-thin Alq3 at the cathode interface," *Organic Electronics*, vol. 15, no. 11, pp. 2710–2714, Nov. 2014.

[43] Y. Zhou, C. Fuentes-Hernandez, J. Shim, J. Meyer, A. J. Giordano, H. Li, P. Winget, T. Papadopoulos, H. Cheun, J. Kim, M. Fenoll, A. Dindar, W. Haske, E. Najafabadi, T. M. Khan, H. Sojoudi, S. Barlow, S. Graham, J. L. Bredas, S. R. Marder, A. Kahn, and B. Kippelen, "A Universal Method to Produce Low-Work Function Electrodes for Organic Electronics," *Science*, vol. 336, no. 6079, pp. 327–332, Apr. 2012.

[44] Y. J. Park, K. S. Ryu, N.-G. Park, Y.-S. Hong, and S. H. Chang, "RF-Sputtered Vanadium Oxide Films," *J. Electrochem. Soc.*, vol. 149, no. 5, pp. A597–A602, 2002.

[45] G. Li, C. W. Chu, V. Shrotriya, J. Huang, and Y. Yang, "Efficient inverted polymer solar cells," *Appl. Phys. Lett.*, vol. 88, no. 25, p. 253503, 2006.

[46] K. X. Steirer, P. F. Ndione, N. E. Widjonarko, M. T. Lloyd, J. Meyer, E. L. Ratcliff, A. Kahn, N. R. Armstrong, C. J. Curtis, D. S. Ginley, J. J. Berry, and D. C. Olson, "Enhanced Efficiency in Plastic Solar Cells via Energy Matched Solution Processed NiOx Interlayers," *Adv. Energy Mater.*, vol. 1, no. 5, pp. 813–820, Jul. 2011.

[47] K. Ellmer, "Past achievements and future challenges in the development of optically transparent electrodes," *Nature Photonics*, vol. 6, pp. 809–817, Nov. 2012.

[48] J. Zou, C.-Z. Li, C.-Y. Chang, H.-L. Yip, and A. K. Y. Jen, "Interfacial Engineering of Ultrathin Metal Film Transparent Electrode for Flexible Organic Photovoltaic Cells," *Adv. Mater.*, vol. 26, no. 22, pp. 3618–3623, Mar. 2014.

[49] K.-S. Chen, H.-L. Yip, J.-F. Salinas, Y.-X. Xu, C.-C. Chueh, and A. K. Y. Jen, "Strong Photocurrent Enhancements in Highly Efficient Flexible Organic Solar Cells by Adopting a Microcavity Configuration," *Adv. Mater.*, vol. 26, no. 20, pp. 3349–3354, Mar. 2014.

[50] T. Schwab, S. Schubert, L. Müller-Meskamp, K. Leo, and M. C. Gather, "Eliminating Micro-Cavity Effects in White Top-Emitting OLEDs by Ultra-Thin Metallic Top Electrodes," *Advanced Optical Materials*, vol. 1, no. 12, pp. 921–925, Oct. 2013.

[51] Y. Zhu, Z. Sun, Z. Yan, Z. Jin, and J. M. Tour, "Rational Design of Hybrid Graphene Films for High-Performance Transparent Electrodes," *ACS Nano*, vol. 5, no. 8, pp. 6472–6479, Aug. 2011.

[52] B. O'Connor, C. Haughn, K.-H. An, K. P. Pipe, and M. Shtein, "Transparent and conductive electrodes based on unpatterned, thin metal films," *Appl. Phys. Lett.*, vol. 93, no. 22, p. 223304, 2008.

[53] G. H. Jung, K. Hong, W. J. Dong, S. Kim, and J.-L. Lee, "BCP/Ag/MoO3 Transparent Cathodes for Organic Photovoltaics," *Adv. Energy Mater.*, vol. 1, no. 6, pp. 1023–1028, Sep. 2011.

[54] D. T. Nguyen, S. Vedraine, L. Cattin, P. Torchio, M. Morsli, F. Flory, and J. C.

Bernède, “Effect of the thickness of the MoO3 layers on optical properties of MoO3/Ag/MoO3 multilayer structures,” *J. Appl. Phys.*, vol. 112, no. 6, p. 063505, 2012.

[55] L. Cattin, M. Morsli, F. Dahou, S. Y. Abe, A. Khelil, and J. C. Bernède, “Investigation of low resistance transparent MoO3/Ag/MoO3 multilayer and application as anode in organic solar cells,” *Thin Solid Films*, vol. 518, no. 16, pp. 4560–4563, Jun. 2010.

[56] B. Tian, G. Williams, D. Ban, and H. Aziz, “Transparent organic light-emitting devices using a MoO3/Ag/MoO3 cathode,” *J. Appl. Phys.*, vol. 110, no. 10, p. 104507, 2011.

[57] L. Shen, Y. Xu, F. Meng, F. Li, S. Ruan, and W. Chen, “Semitransparent polymer solar cells using V2O5/Ag/V2O5 as transparent anodes,” *Organic Electronics*, vol. 12, no. 7, pp. 1223–1226, Jul. 2011.

[58] K. Hong, K. Kim, S. Kim, I. Lee, H. Cho, S. Yoo, H. W. Choi, N.-Y. Lee, Y.-H. Tak, and J.-L. Lee, “Optical Properties of WO 3/Ag/WO 3Multilayer As Transparent Cathode in Top-Emitting Organic Light Emitting Diodes,” *J. Phys. Chem. C*, vol. 115, no. 8, pp. 3453–3459, Mar. 2011.

[59] M.-G. Kang, H. J. Park, S. H. Ahn, T. Xu, and L. J. Guo, “Toward Low-Cost, High-Efficiency, and Scalable Organic Solar Cells with Transparent Metal Electrode and Improved Domain Morphology,” *IEEE J. Select. Topics Quantum Electron.*, vol. 16, no. 6, pp. 1807–1820.

[60] J. van de Groep, P. Spinelli, and A. Polman, “Transparent Conducting Silver Nanowire Networks,” *Nano Lett.*, vol. 12, no. 6, pp. 3138–3144, Jun. 2012.

[61] H. Wu, D. Kong, Z. Ruan, P.-C. Hsu, S. Wang, Z. Yu, T. J. Carney, L. Hu, S. Fan, and Y. Cui, “A transparent electrode based on a metal nanotrough network,” *Nature Nanotechnology*, vol. 8, no. 6, pp. 421–425, May 2013.

[62] Y. Jia, A. Cao, X. Bai, Z. Li, L. Zhang, N. Guo, J. Wei, K. Wang, H. Zhu, D. Wu, and P. M. Ajayan, “Achieving High Efficiency Silicon-Carbon Nanotube Heterojunction Solar Cells by Acid Doping,” *Nano Lett.*, vol. 11, no. 5, pp. 1901–1905, May 2011.

[63] Y. Jung, X. Li, N. K. Rajan, A. D. Taylor, and M. A. Reed, “Record High

Efficiency Single-Walled Carbon Nanotube/Silicon p –n Junction Solar Cells," *Nano Lett.*, vol. 13, no. 1, pp. 95–99, Jan. 2013.

# Chapter 2

# Proposed Amorphous Silicon Photovoltaic (PV) Structure

## 2.1 Introduction

Chapter 2 describes the energy band diagram and PV performance of proposed structure. In order to address the above challenges of amorphous silicon (a-Si) PV introduced in Chapter 1, we have been building ultra-thin a-Si photoactive layer without doping, helped by efficient electron and hole transport layers instead, as depicted in Figure 2.1. Studying the proposed device structures, we have experimentally found that the performance factors of the ultra-thin a-Si photovoltaic cells varied according to the property and thickness of multiple layers including a-Si, which has been first extensively studied in this dissertation. The improved cathode contact, frequently described throughout the dissertation, has been reported in the journal paper, J. Y. Lee *et al*., "Improved solar cell performance by adding ultra-thin $Alq_3$ at the cathode interface," *Organic Electronics*, vol. 15, pp. 2710–2714, 2014.

## 2.2 Energy Band Diagram of Proposed Structure

We propose to build an undoped amorphous silicon (a-Si) photoactive layer with electron and hole transport layers (Figure 2.1), via which we can design to extract photogenerated charges in the a-Si photoactive layer efficiently. The electron transport layer is built with an organic interfacial layer, one of three possible candidates ($C_{60}$, PCBM, and ICBA) [1]. Since indene-$C_{60}$ bisadduct (ICBA) LUMO (Lowest Unoccupied Molecular Orbital) aligns well with a-Si conduction energy level and Al/LiF/$Alq_3$ cathode work function [2], [3], it forms best Ohmic contact with least series resistance (Figure 2.2). The Al/LiF/$Alq_3$ cathode configuration has been proved to work very well with phenyl-C61-butyric acid methyl ester (PCBM) and $C_{60}$ charge transport layer regardless of photoactive layers, which can be either a polymer material or a-Si [2]. In case of PCBM and $C_{60}$, their LUMO levels are lower than the cathode work function and a-Si conduction level, thereby trapping electrons occur due to energy loss during the transport process.

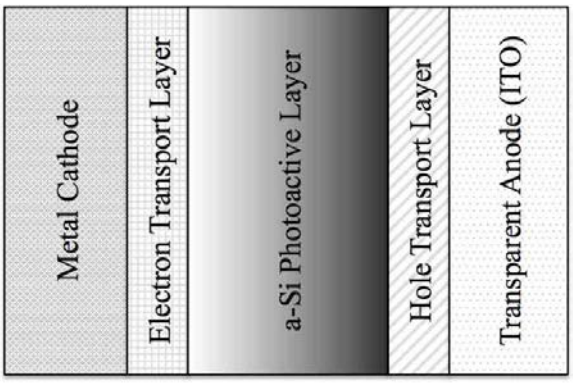


Figure 2.1. Undoped amorphous silicon (a-Si) photoactive layer is built to interface with electron and hole transport layers for efficient charge extraction to metal cathode and transparent anode, respectively.

The organic interfacial layer operates for hole blocking purpose as well because HOMO (Highest Occupied Molecular Orbital) is lower than a-Si valence energy level in Figure 2.2. As a hole extraction layer, we employed metal oxide, such as vanadium(V) oxide ($V_2O_5$) with high work function in order to maximize work function difference between cathode and anode [4]. Electrons are injected from ITO anode to the lower conduction level of $V_2O_5$ so that photogenerated holes from a-Si recombine with the supplied electrons very efficiently (Figure 2.2).

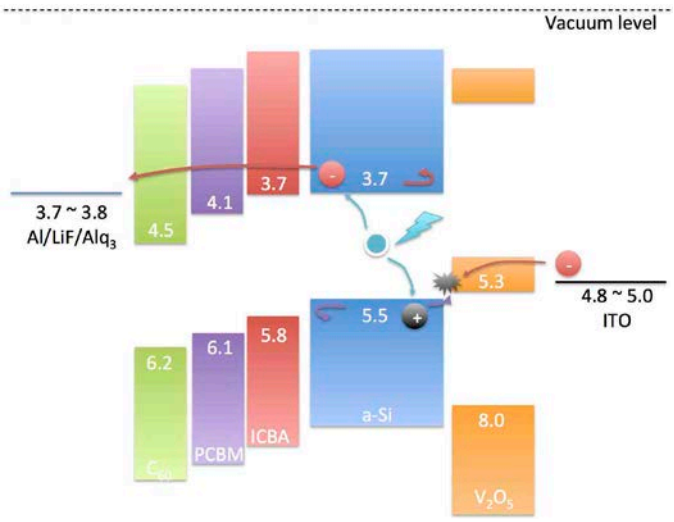


Figure 2.2. Energy band diagram of amorphous silicon (a-Si) hybrid cells with three different organic interfacial layers ($C_{60}$, PCBM, ICBA) and vanadium pentoxide ($V_2O_5$).

Among several metal oxides, $V_2O_5$ is also known for having an empty band in d-bands above conduction energy level (Figure 2.2 and 2.3) [5]. Thus, the empty energy gap allows $V_2O_5$ to prevent photogenerated electrons from being lost to anode.

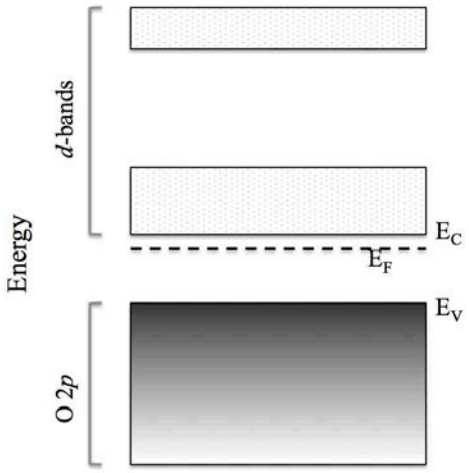


Figure 2.3. Empty band above conduction energy level for $V_2O_5$: d-bands have an energy gap empty. (Reproduced from ref. [5])

## 2.3 PV Performance of Proposed Device

Conventional thin film a-Si photovoltaic cells have doped layers to build an internal electric field inside of undoped a-Si. The doped layers typically require certain thickness for a sufficient built-in potential, which have been optimized for many years. However the doped layers do not contribute to electric charge generation since photogenerated charges in doped a-Si are recombined by dopants, so called defects. Also the inevitably thick a-Si active layer is subject to light-induced degradation, which traditional a-Si solar cells have been suffering in practical applications. In order to address the seemingly unsolvable issues, we have been trying to build a-Si photovoltaic cells incorporating undoped a-Si without any doping. In terms of fabrication process, it will be also beneficial if we are able to remove two extra depositions of n- and p- doped layers. Without doped regions in a-Si active layer, in conventional knowledge, the

photovoltaic (PV) performance is expected to be inefficient. The PV performance is assessed by the current density-voltage (J-V) characterization, whose setup diagram is illustrated in Figure 2.4.

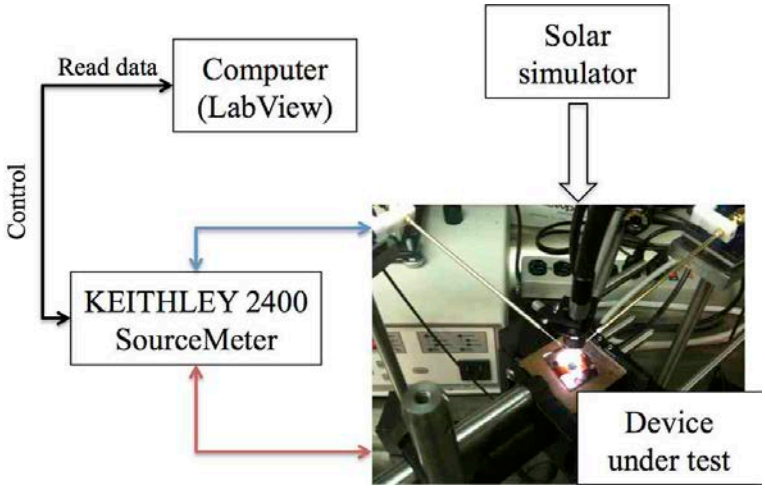


Figure 2.4. A schematic diagram of current density-voltage (J-V) characterization setup: A solar simulator, a source meter, a computer equipped with LabView hardware/software, and a device on an optical stage.

In the J-V characterization setup, a solar simulator is for the simulated 1 sun or the concentrated sun illumination to a device under test. Here the computer equipped with LabView hardware/software controls a source meter in order to operate voltage bias sweep and collect photocurrent data from the source meter. The device is set up on a properly implemented optical stage and probed with xyz-positioned manipulators for cathode and anode contacts.

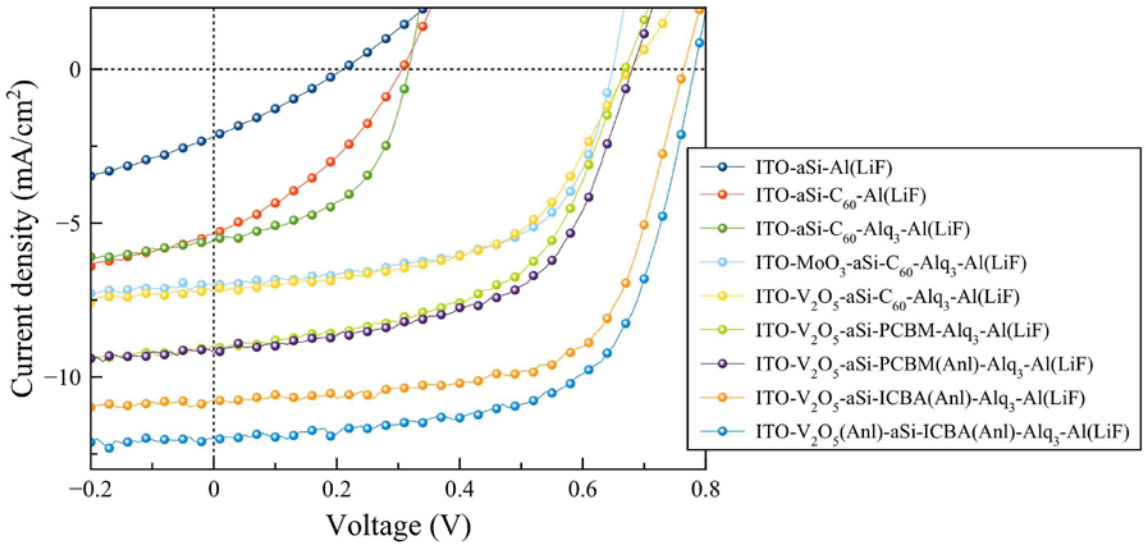


Figure 2.5. Current density-voltage (J-V) performance improvement according to the material selection as well as the optimization of our hybrid a-Si photovoltaic cells where a-Si thickness is 50 nm.

In the J-V characteristics of the undoped a-Si cells, for instance, the poor photovoltaic performance of a basic device structure, ITO (transparent anode)/undoped a-Si/aluminum (Al) with LiF (metal cathode), is shown in Figure 2.5. Even though the basic undoped a-Si photovoltaic cells have a small open circuit voltage and a little short circuit current due to the work function difference between ITO and Al/LiF, it is obvious that the cells are required to have much higher internal electric field so as to perform much better as solar cells. As a solution for attaining higher built-in potential, an efficient Schottky contact (anode) can be considered in our undoped a-Si structure. At the same time, a very effective Ohmic contact is desirable on the other side (cathode) for facilitating photogenerated charge extraction. In Figure 2.5, we show how enormously the appropriately designed anode and cathode electrical contacts influence the power efficiency of our undoped a-Si hybrid structures. We name the structures as hybrid

devices due to inorganic metal oxides used for hole transport (anode) and organic materials for electron transport (cathode). In the present study, metal oxides molybdenum ($MoO_3$) or $V_2O_5$ form high work function Schottky contact in anode, and *Tris*(8-hydroxyquinoline) aluminum ($Alq_3$), $C_{60}$, $PC_{60}BM$, or ICBA organic materials for Ohmic contact in cathode.

Very thin undoped a-Si active layer, around 50 nm in this characterization, is utilized to achieve about 6 % power conversion efficiency on flat substrate as demonstrated by the best performance in Figure 2.5. We strongly propose that broader material search and more optimization need to be done for performance improvement from the present power efficiency. Moreover, thin-film a-Si photovoltaic cells are generally built on light scattering substrate to enhance light absorption in active layer. We believe the light scattering effect will be more advantageous to the hybrid cells than the typical active layer, including doped region, since the photogenerated charges can be extracted without severe recombination by dopants. Considering the light scattering effect, the present power efficiency is available to be further increased benefited by the enhanced light absorption in the undoped active layer, which will be discussed more in Chapter 5.

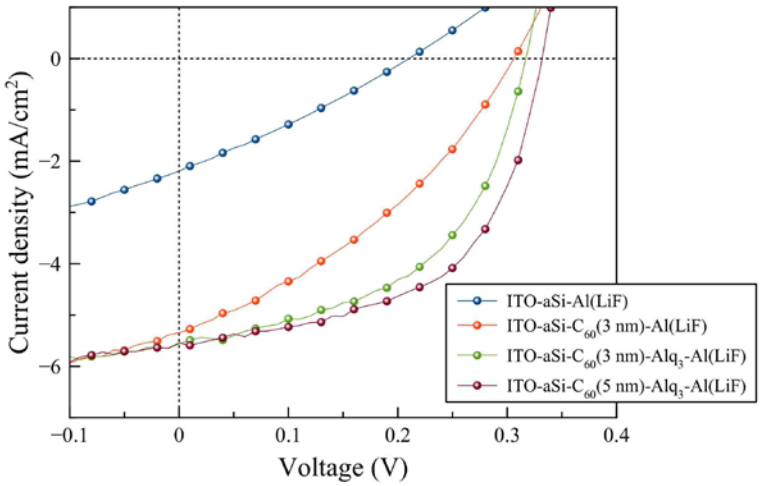


Figure 2.6. Performance enhancement by $Alq_3$ and $C_{60}$ applied to cathode for Ohmic contact.

Since the a-Si hybrid cells are lack of highly doped regions in the active layer, Ohmic contact at one electrode is crucial to extract photogenerated charges efficiently. In Figure 2.6, applying $C_{60}$ small molecules and $Alq_3$ organic materials between undoped a-Si and aluminum (Al) metal electrode is proved to be very effective to improve power efficiency. We attribute the improvement to the electron transporting property of $C_{60}$ material and the reduced contact resistance by $Alq_3$ interfacing with Al electrode [2]. However, as there is difference between a-Si conduction band level (~ 3.7 eV) and lowest unoccupied molecular orbital (LUMO) of $C_{60}$ (4.3 ~ 4.5 eV) [2], it should be noted that much better Ohmic contact is achievable by energy band level alignment.

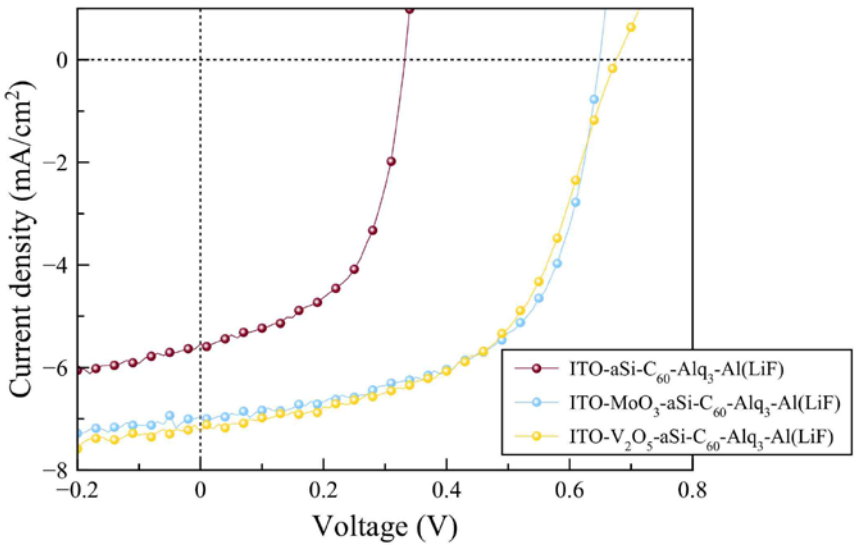


Figure 2.7. Metal oxides form Schottky contacts at anode for power efficiency improvement.

At anode, direct contact of undoped a-Si with ITO (~ 4.8 eV work function) is replaced with high work function (5.2 ~ 5.4 eV work function) metal oxide Schottky contact as depicted in Figure 2.7 [4], [6], [7]. We experimentally observe very large amount of open circuit voltage increase, which is believed to be due to more efficient Schottky contact by high work function metal oxides. The metal oxides ($V_2O_5$ and $MoO_3$) utilized in a-Si hybrid cells are known for good hole transporting materials as well [8], [9]. Here the metal oxides are deposited at 0.2Å$s^{-1}$ by thermal evaporation in base pressure $1\times10^{-6}$ mbar high vacuum chamber. In Figure 2.7, interestingly, $V_2O_5$ cell holds higher open circuit voltage than $MoO_3$ cell even though electron and hole charge extraction imbalance is noted (a little S-shaped on x-axis) [10]-[12]. In order to verify the difference of $V_2O_5$ and $MoO_3$ anode cells, we compare the capacitance responses to small perturbation voltage (10 mV @ 10 kHz) at forward bias in Figure 2.8. The capacitance-

voltage (C-V) characterization uses very similar set up to the one in Figure 2.4, but KEITHLEY 4200 semiconductor characterization system does data acquisition instead.

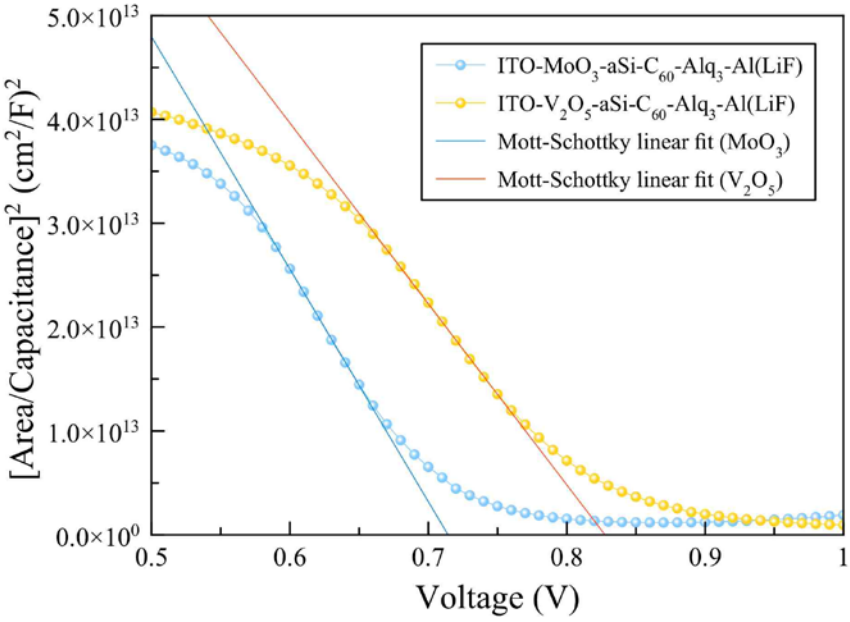


Figure 2.8. Potentially more efficient $V_2O_5$ than $MoO_3$ for Schottky contact according the Mott-Schottky analysis of hybrid a-Si cells.

By fitting Mott-Schottky linear analysis (Eq. 2.1) on capacitance characteristics in Figure 2.8, we extrapolate larger built-in potential by $V_2O_5$ than $MoO_3$ anode referring to the voltage axis intercepts [2], [13]-[16].

$$\frac{A^2}{C^2} = \left(\frac{2}{q\varepsilon_s N}\right)\left\{\left(V_{bi} - \frac{kT}{q}\right) - V\right\} \qquad (2.1)$$

Here, C and V are the capacitance and voltage between the anode and cathode, respectively, A the active area for the device, q the elementary charge, $\varepsilon_s$ the relative dielectric constant, N the effective doping density, and $V_{bi}$ the built-in potential.

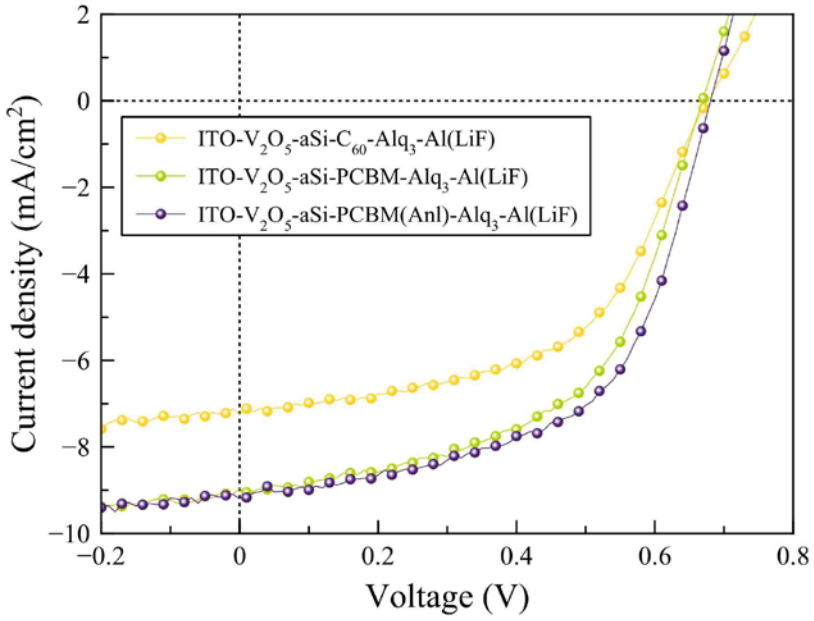


Figure 2.9. Better Ohmic contact and improved short circuit current by replacing small molecule $C_{60}$ with polymer $PC_{60}BM$, further enhanced by annealing (Anl) process.

In order to address the existing charge extraction imbalance, we select better energy level aligning material for more efficient Ohmic contact in cathode. Firstly, we applied $PC_{60}BM$ (~ 4.0 eV LUMO) closer aligning to undoped a-Si conduction band (~ 3.7 eV) (Figure 2.9) [1], [2]. We observe that short circuit current is improved hugely and the S-shaped curve at the voltage axis is also removed. Further performance improvement is possible by annealing the hybrid cells after polymer solution casting, which is expected to eliminate residual solvent in the polymer layer. The thermal annealing of the organic electron transport layer was executed for 5 minutes on a hot plate at 110 °C. Here the

device substrates were put on a silicon wafer for uniform heat distribution through out the annealing area.

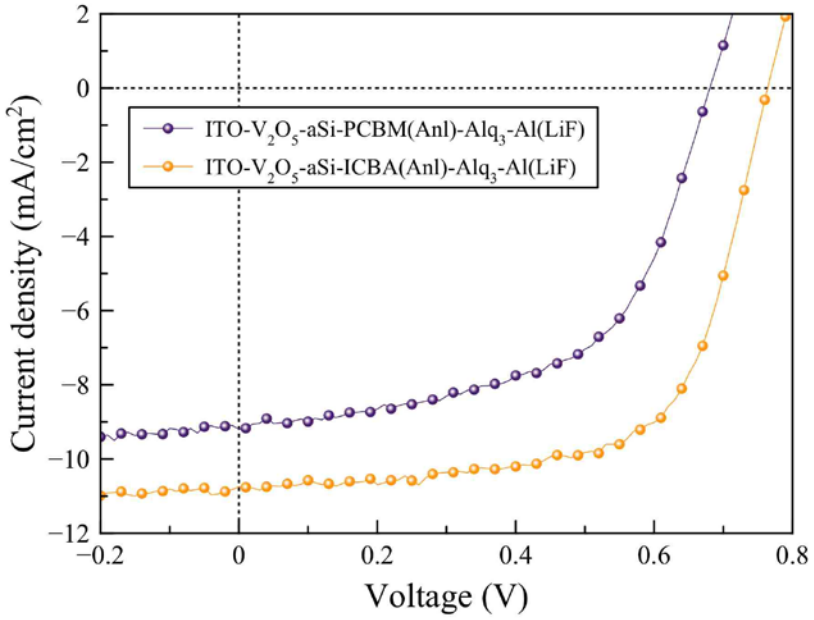


Figure 2.10. Enhanced performance by ICBA cathode contact compared to $PC_{60}BM$ due to better alignment in LUMO level of the polymer and a-Si conduction band.

The better LUMO and conduction band energy level aligning by incorporating ICBA (~ 3.7 eV LUMO) enhances the power efficiency of our hybrid cells further as described in Figure 2.10. Here the ICBA was spin-casted for 60 seconds at 2000 rpm in a 0.23 wt% solution with chlorobenzene, stirred for at least 1 hour at ~60 °C, expected to form around 5 nm-thick film on top of a-Si layer. Experimentally, the optimized thermal annealing (Anl) process on metal oxide layer at anode is also confirmed to be beneficial for electric power generating performance improvement (Figure 2.11). The metal oxide annealing process was performed in a rapid thermal annealing (RTA) tool with a gas mixture of 80 % nitrogen ($N_2$) and 20 % oxygen ($O_2$) at 300 °C for 10 minutes. After the

annealing of $V_2O_5$, we can observe film color change, which represents the $VO_x$ phase change, thereby inducing conductivity variation and work function shift accordingly [17].

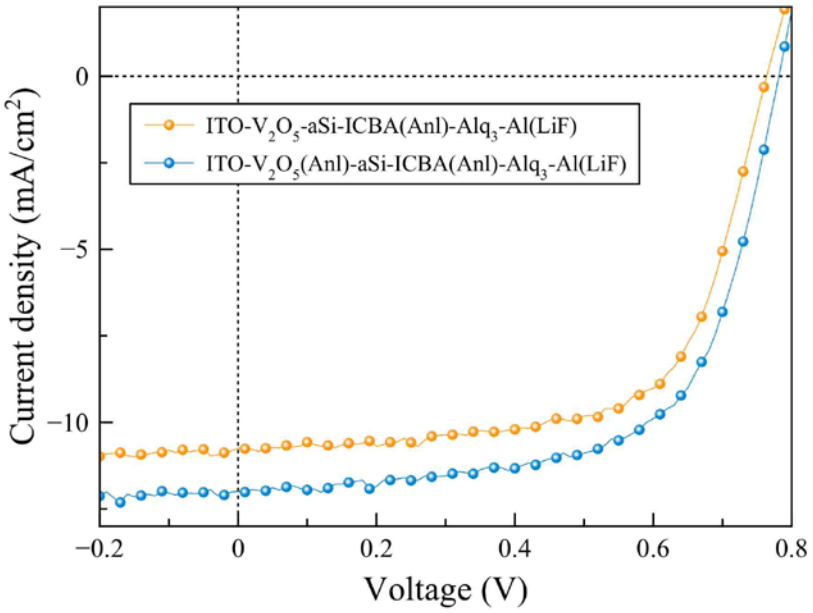


Figure 2.11. Experimentally verified power efficiency increase by metal oxide ($V_2O_5$) annealing process.

In this dissertation, we have worked on undoped a-Si photoactive material; but we are certain that our hybrid device model can be applied to other undoped inorganic photoactive materials, such as a-SiGe, a-Ge, or even GaAs, etc. Also our inorganic and organic charge transport material selection can be a design guide for various hybrid solar cells incorporating undoped photoactive materials.

## 2.4 Conclusion

To conclude, we have proposed to build an undoped amorphous silicon (a-Si) photoactive layer with electron and hole transport layers. As the energy band levels of materials are important to be considered for charge transport and electrode contacts, we have studied a band diagram incorporating undoped a-Si, charge transport materials, and both electrodes (cathode and anode). Here photogenerated charges in undoped a-Si active layer are extracted via electron and hole transport layers. The electron transport layer is built with an organic interfacial layer, indene-$C_{60}$ bisadduct (ICBA), since the lowest unoccupied molecular orbital (LUMO) of ICBA aligns well with a-Si conduction energy level and Al/LiF/$Alq_3$ cathode work function. For a hole transport layer, we employed metal oxide, such as vanadium(V) pentoxide ($V_2O_5$) with high work function in order to maximize work function difference between cathode and anode. Both transport materials block the other charge efficiently to maximize selective charge transport for photovoltaic (PV). We name the structures as hybrid devices due to inorganic metal oxides used for hole transport (anode) and organic materials for electron transport (cathode). The PV performance of the proposed a-Si hybrid devices is assessed by the current density-voltage (J-V) characterization. We experimentally showed how the designed anode and cathode electrical contacts play important roles in influencing the power efficiency of the hybrid structures. At cathode, the performance is highly dependent on Ohmic contact quality, while in anode an efficient Schottky contact with metal oxides is critical. Both cathode and anode interfacial layers have been thermally annealed for performance

improvement. As a result, we could achieve about 6 % power conversion efficiency by around 50 nm undoped a-Si on a flat glass substrate.

# References


[1] H.-L. Yip and A. K. Y. Jen, "Recent advances in solution-processed interfacial materials for efficient and stable polymer solar cells," *Energy Environ. Sci.*, vol. 5, no. 3, pp. 5994–6011, 2012.

[2] J. Y. Lee, T. Lee, H. J. Park, and L. J. Guo, "Improved solar cell performance by adding ultra-thin Alq3 at the cathode interface," *Organic Electronics*, vol. 15, no. 11, pp. 2710–2714, Nov. 2014.

[3] Y. He, H.-Y. Chen, J. Hou, and Y. Li, "Indene−C 60Bisadduct: A New Acceptor for High-Performance Polymer Solar Cells," *J. Am. Chem. Soc.*, vol. 132, no. 4, pp. 1377–1382, Feb. 2010.

[4] J. Meyer, K. Zilberberg, T. Riedl, and A. Kahn, "Electronic structure of Vanadium pentoxide: An efficient hole injector for organic electronic materials," *J. Appl. Phys.*, vol. 110, no. 3, p. 033710, 2011.

[5] M. T. Greiner, "Universal energy-level alignment of molecules on metal oxides," *Nature Materials*, vol. 11, no. 1, pp. 76–81, Nov. 2011.

[6] S. Krishnakumar and C. S. Menon, "Optical and electrical properties of vanadium pentoxide thin films," *Phys. Stat. Sol*, vol. 153, pp. 439–444, 1996.

[7] G. Li, C. W. Chu, V. Shrotriya, J. Huang, and Y. Yang, "Efficient inverted polymer solar cells," *Appl. Phys. Lett.*, vol. 88, no. 25, p. 253503, 2006.

[8] D. T. Nguyen, S. Vedraine, L. Cattin, P. Torchio, M. Morsli, F. Flory, and J. C. Bernède, "Effect of the thickness of the MoO3 layers on optical properties of MoO3/Ag/MoO3 multilayer structures," *J. Appl. Phys.*, vol. 112, no. 6, p. 063505, 2012.

[9] C.-H. Chou, W. L. Kwan, Z. Hong, L.-M. Chen, and Y. Yang, "A Metal-Oxide

Interconnection Layer for Polymer Tandem Solar Cells with an Inverted Architecture," *Adv. Mater.*, vol. 23, no. 10, pp. 1282–1286, Sep. 2010.

[10] J. C. Wang, X. C. Ren, S. Q. Shi, C. W. Leung, and P. K. L. Chan, "Charge accumulation induced S-shape Jâ€"V curves in bilayer heterojunction organic solar cells," *Organic Electronics*, vol. 12, no. 6, pp. 880–885, Jun. 2011.

[11] W. Tress, A. Petrich, M. Hummert, M. Hein, K. Leo, and M. Riede, "Imbalanced mobilities causing S-shaped IV curves in planar heterojunction organic solar cells," *Appl. Phys. Lett.*, vol. 98, no. 6, p. 063301, 2011.

[12] A. Kumar, S. Sista, and Y. Yang, "Dipole induced anomalous S-shape I-V curves in polymer solar cells," *J. Appl. Phys.*, vol. 105, no. 9, p. 094512, 2009.

[13] K. M. O'Malley, C.-Z. Li, H.-L. Yip, and A. K.-Y. Jen, "Enhanced Open-Circuit Voltage in High Performance Polymer/Fullerene Bulk-Heterojunction Solar Cells by Cathode Modification with a C60 surfactant," *Adv. Energy Mater.*, vol. 2, pp. 82–86, 2012.

[14] M. Mingebach, C. Deibel, and V. Dyakonov, "Built-in potential and validity of the Mott-Schottky analysis in organic bulk heterojunction solar cells," *Phys. Rev. B*, vol. 84, no. 15, p. 153201, Oct. 2011.

[15] J. Kong, J. Lee, Y. Jeong, M. Kim, S.-O. Kang, and K. Lee, "Biased internal potential distributions in a bulk-heterojunction organic solar cell incorporated with a TiOx interlayer," *Appl. Phys. Lett.*, vol. 100, no. 21, p. 213305, 2012.

[16] T. Kirchartz, W. Gong, S. A. Hawks, T. Agostinelli, R. C. I. MacKenzie, Y. Yang, and J. Nelson, "Sensitivity of the Mott–Schottky Analysis in Organic Solar Cells," *J. Phys. Chem. C*, vol. 116, no. 14, pp. 7672–7680, Apr. 2012.

[17] M. H. Yoon and S. Im, "Electrical characteristics of V2O5 thin films formed on p-Si by sputter-deposition and rapid thermal annealing," *Applied Surface Science*, vol. 244, no. 1, pp. 444–448, May 2005.

# Chapter 3

# Electrical Performance Characterization of a-Si Hybrid Device

## 3.1 Introduction

In Chapter 3, we analyze the electrical performance of the undoped a-Si hybrid device discussing open circuit voltage change and transient photo-response. Also we exploit how the intrinsic a-Si thickness in the undoped hybrid structure affects photovoltaic performance and why a-Si thickness needs to be optimized properly with charge transport materials. In specific, the fill factor (FF) of the hybrid PV is examined according to different a-Si thicknesses, further supported by higher solar concentration experiment. In order to attain the evidence of a-Si thickness being very critical for FF in the hybrid PV, we investigate charge transport dynamics in the hybrid structure. By exploring the transient photocurrent and photovoltage characteristics of the hybrid PV at open circuit as well as short circuit condition, we have obtained the ambipolar diffusion length of photo-carriers.

## 3.2 Open Circuit Voltage Change in Ultra-thin a-Si Regime

The ultra-thin amorphous silicon (a-Si) photovoltaic cells are able to operate without doped layers as they have efficient electron and hole transport layers, for cathode and anode, respectively. In order to form high work function electrode for the anode, we used vanadium(V) oxide ($V_2O_5$) [1], with indium-tin oxide (ITO) and glass substrate. The cathode begins with a thin organic layer, indene-$C_{60}$ bisadduct (ICBA) [2], for Ohmic contact extracting photogenerated electrons efficiently. The Ohmic contact is completed by *tris*(8-hydroxyquinoline) aluminum ($Alq_3$) and LiF [3], interfaced with low work function metal aluminum (Al) as described in Figure 3.1. Since the two electrodes, cathode and anode, have work function difference, we anticipate a built-in potential in the undoped a-Si photoactive layer. Here we interestingly found out the photovoltaic operation range varied based on the a-Si thickness. In our experiments, we investigated three different thicknesses, 15, 30, and 180 nm. Here we consider 180 nm-thick a-Si hybrid cell as a reference so that we compare the ultra-thin (15 and 30 nm) cells with.

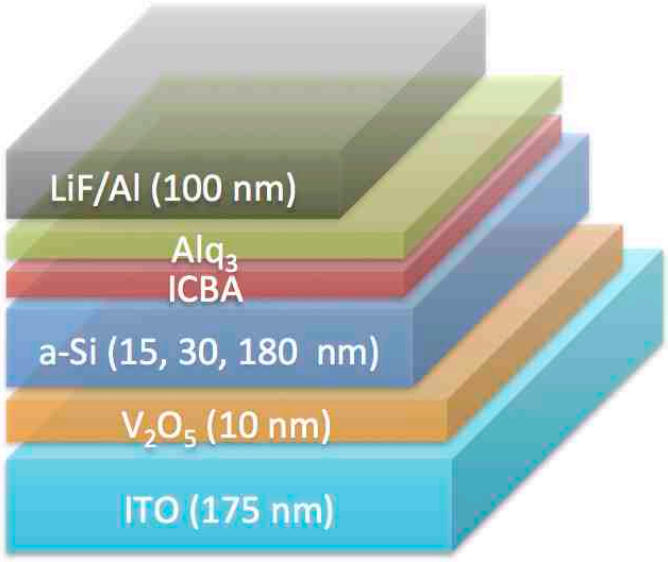


Figure 3.1. Device structure of a-Si hybrid photovoltaic cells: A schematic diagram of proposed structure. The structure comprises cathode, anode, and undoped a-Si. The cathode is composed of aluminum and organic layers, and ITO/$V_2O_5$ for the anode. The undoped a-Si layer thicknesses investigated are 15, 30, and 150 nm.

We explored current density-voltage (J-V) performances under AM 1.5 (1 sun) illumination and dark conditions; later in this thesis, we will also describe the effect of higher sun concentration to the hybrid cells. In J-V characteristics of the undoped a-Si hybrid cells, under 1 sun illumination, as the a-Si photoactive layer gets thinner, the open circuit voltage ($V_{oc}$) of the undoped a-Si hybrid cells decreases in Figure 3.2.

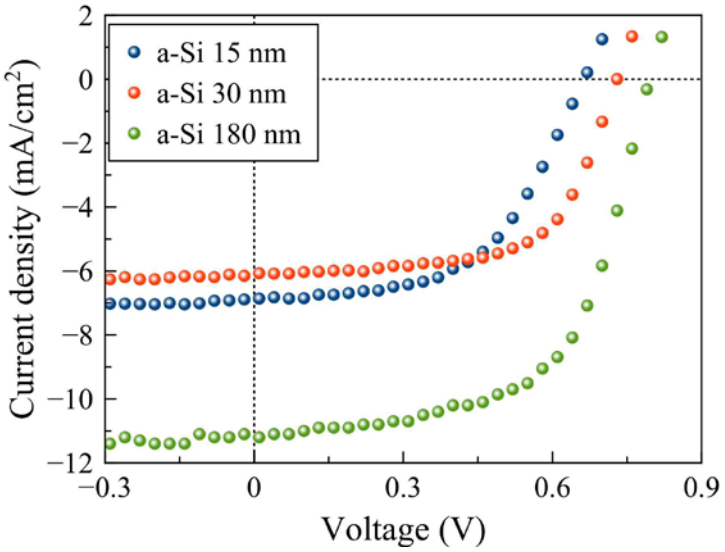


Figure 3.2. Electrical performance of a-Si hybrid photovoltaic cells: Current density-voltage (J-V) characteristics of the hybrid cells with three different a-Si thicknesses under AM1.5 (1 Sun) illumination condition.

The series resistance increases by the a-Si thickness decrease as well. This performance difference is also shown in the J-V curves under dark condition as shown in Figure 3.3.

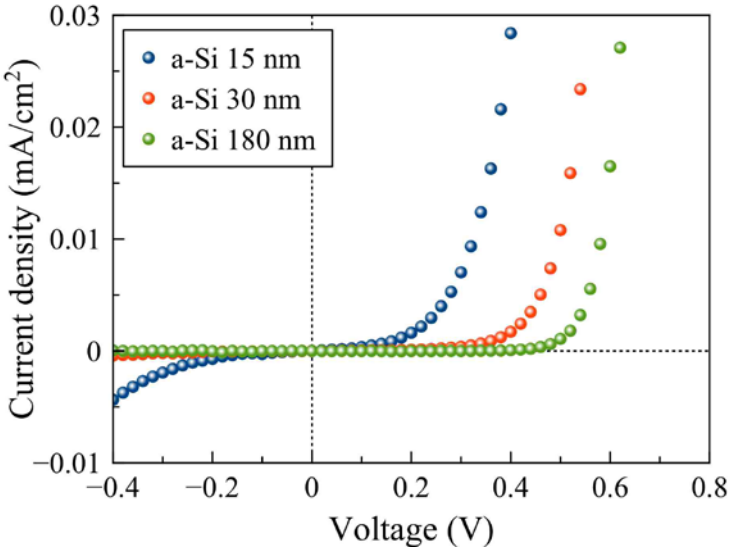


Figure 3.3. Electrical performance of a-Si hybrid photovoltaic cells: Current density-voltage (J-V) characteristics of the hybrid cells under dark condition.

The thinner a-Si cells turn on earlier in forward bias due to larger saturation current density in reverse bias. The larger saturation current density ($J_S$) is also attributed to the $V_{oc}$ decrease under 1 sun condition regarding to Eq. 3.1 where larger saturation current density gives smaller $V_{oc}$.

$$V_{OC} = (nkT/q)\times\ln\left(J_{SC}/J_S + 1\right) \qquad (3.1)$$

Here, $n$ is ideality factor, $kT$ the thermal energy at room temperature, $q$ the elementary charge, and $J_{SC}$ the short circuit current density. The J-V characteristics under dark condition are determined by saturation current density ($J_S$) and ideality factor ($n$) (Eq. 3.2). Especially ideality factor is obtainable by the slope in the log scale current density versus voltage bias ($V$) curve as shown in Figure 3.4.

$$\ln(J/J_S - 1) = (1/n) \times (q/kT) \times V \qquad (3.2)$$

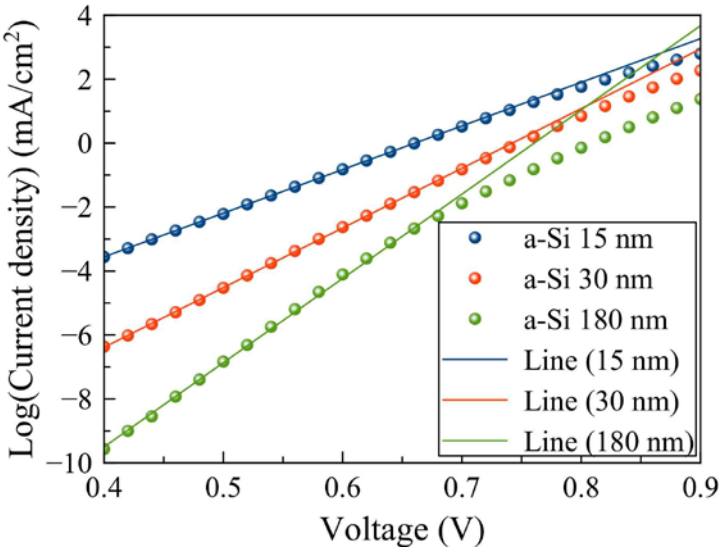


Figure 3.4. Electrical performance of a-Si hybrid photovoltaic cells: The dark J-V curves in the log scale of current density where linear lines are fitted.

We observed that the thinner a-Si hybrid cells have larger ideality factor compared to the thick a-Si (180 nm) reference cell. It is well known that the ideality factor represents internal resistance, accounting for photogenerated charge recombination. Since the thinner a-Si hybrid cells have larger series resistance, we experimentally propose that the larger ideality factor explains the series resistance increase in photovoltaic operation as the a-Si thickness decreases. The possible higher inter-band defect density is anticipated based on the above J-V characteristics; thus will be investigated further by capacitance-frequency (C-f) and capacitance-voltage (C-V) measurements in the later part of this chapter. The $V_{oc}$ variation according to different a-Si thickness, as observed in Figure 3.2, needs to be explained. Thus we exploited the $V_{oc}$ change of the a-Si hybrid cells under different solar concentration ($C$) condition. As the

ideality factor determines the amount of $V_{oc}$ change with regard to the solar concentration variation as depicted in Eq. 3.3, the different ideality factors of the hybrid cells with various thicknesses can be discussed.

$$V_{OC}(C) \approx V_{OC}(1) + (nkT/q)\times\ln(C) \qquad (3.3)$$

The larger ideality factor for the thinner a-Si hybrid cell is confirmed according to the $V_{oc}$ changes in Figure 3.5, which is consistent with the above J-V curves under dark condition. In J-V curves around $V_{oc}$ under different sun concentration (Figure 3.6-3.8), for 15 nm thick a-Si hybrid cells, $V_{oc}$ increased by around 0.12 V when the concentration increased from 1 sun to 7 sun, 0.07 V for 30 nm thick cell, and only 0.04 V for 180 nm cell.

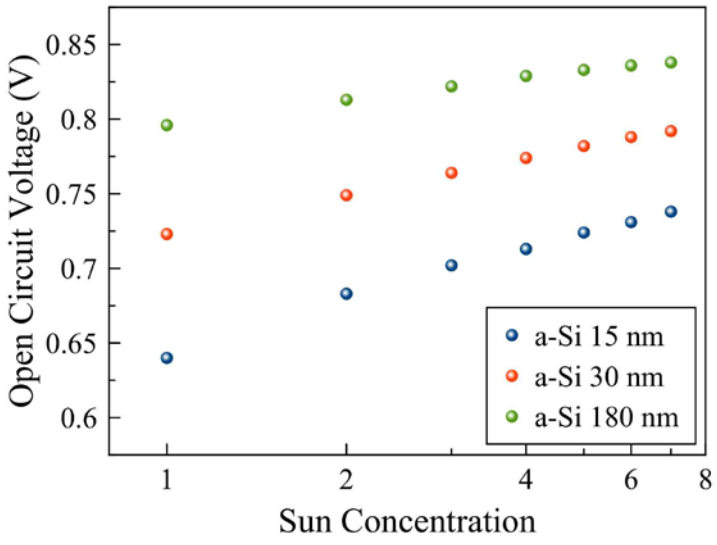


Figure 3.5. Current density-voltage (J-V) characteristics under concentrated sun illumination conditions: Open circuit voltage ($V_{oc}$) of the a-Si hybrid cells with different a-Si thicknesses (15, 30, 150 nm) varies linearly according to the concentrated illumination in log scale.

Based upon the slopes of J-V curves, we also obtain interesting findings that series resistance decreases as the sun concentration increases from 1 sun condition to 7 sun. We assume that the reduced series resistance is an indirect evidence for the existence of possible inter-band defects, getting saturated more by the increased photogenerated charges in higher sun concentration. The more defects get filled by the photogenerated charges, the less internal resistance is opposed to charge extraction due to the reduced charge trapping.

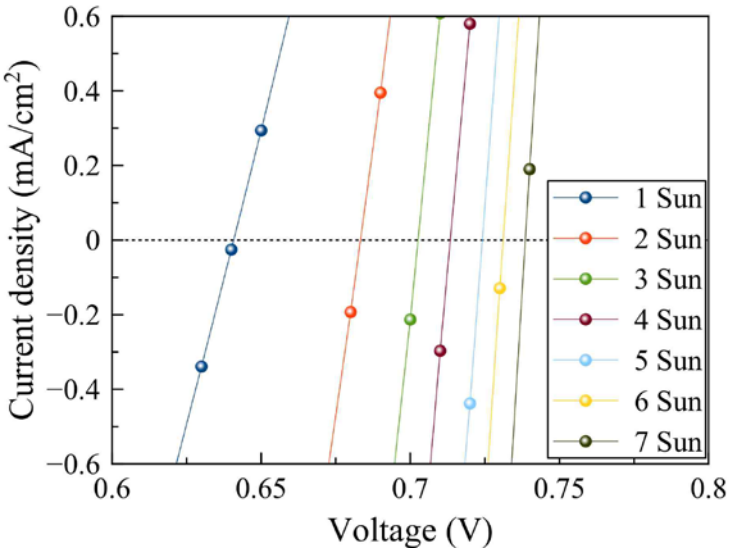


Figure 3.6. Current density-voltage (J-V) characteristics under concentrated sun illumination conditions: $V_{oc}$ increase of 0.12 V for 15 nm thick cell with regard to sun concentration increment from 1 Sun to 7 Sun.

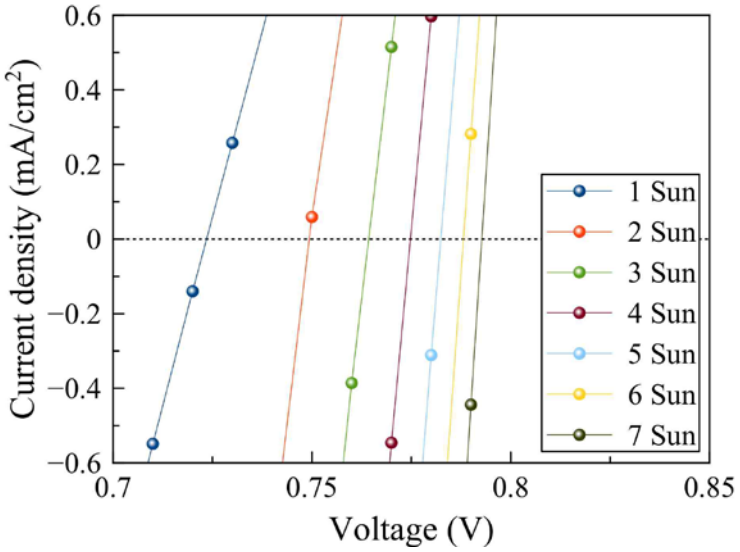


Figure 3.7. Current density-voltage (J-V) characteristics under concentrated sun illumination conditions: $V_{oc}$ increase of 0.07 V for 30 nm thick cell with regard to sun concentration increment from 1 Sun to 7 Sun.

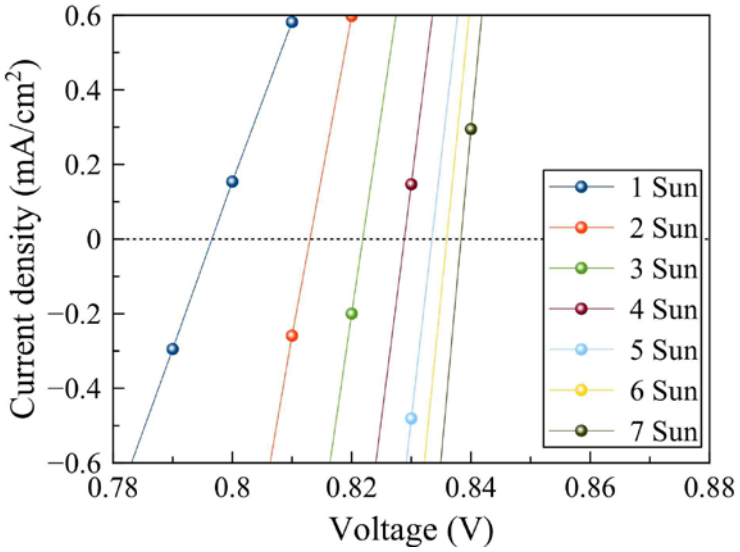


Figure 3.8. Current density-voltage (J-V) characteristics under concentrated sun illumination conditions: $V_{oc}$ increase of 0.04 V for 180 nm thick cell with regard to sun concentration increment from 1 Sun to 7 Sun.

While tracing the cause of the higher ideality factor in the thinner undoped a-Si thickness, we found that how well electric charges get trapped in inter-band defects are closely related to the ideality factor [4], [5]. In order to further study the electrically interactive areal defect density, we characterized our a-Si hybrid cells by capacitance-frequency (C-f) as shown in Figure 3.9. By applying 1 kHz to 1 MHz frequency of 10 mV perturbation signals to the hybrid cells at zero bias, we measured capacitance between cathode and anode using Keithley 4200 equipment. Based on Eq. 3.4, we can get inter-band areal defect density of states (DOS), via which electric charges get trapped and de-trapped, for the hybrid cells with three different thickness a-Si hybrid cells.

$$g_t(E_\omega) = -(V_{FB}/qwkT)\times(dC(\omega)/d\ln\omega)\times thickness, E_\omega = kT\times\ln(\omega_0/\omega) \quad (3.4)$$

Here, $g_t(E_\omega)$ is the areal DOS of defects where charge trapping occurs, $E_\omega$ the energy level offset from conduction band ($E_C$) or valence band ($E_V$), $V_{FB}$ the flat band potential (~ 0.9 V), $\omega$ the angular frequency of the small signal voltage perturbation, $C(\omega)$ the capacitance at the perturbation frequency, $\omega_0$ an attempt-to-escape angular frequency (~ $10^{12}$ $s^{-1}$), and $w$ the depletion width. In terms of the depletion width, we assumed that 15, 30 nm thick cells are totally depleted, and for fair comparison, 30 nm depletion for 180 nm thick cell as well. The defect DOS versus energy level in the bandgap is shown in Figure 3.9. The 15 nm thick a-Si hybrid cells have the highest defect density level, the 180 nm the lowest, and the 30 nm in the middle. In this characterization, we comparably obtained the amount of defects with regard to a-Si thickness, and found

out that the thinner thickness induced the photoactive layer interface to induce higher areal density of electric charge trapping at inter-band defects.

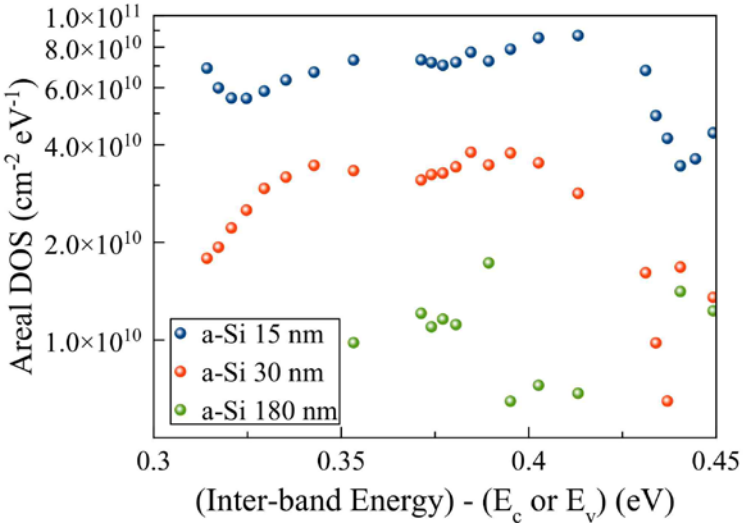


Figure 3.9. Density of states (DOS), in which electric charge trapping occurs at the areal defects, are obtained from the capacitance response to small voltage perturbation with different frequencies; and depicted for three different a-Si thickness hybrid cells.

We also measured capacitance-voltage (C-V) of the hybrid cells in order to investigate any difference on the capacitance response regarding to reverse or forward voltage bias to the electrodes. The same voltage perturbation of 10 mV was applied to the cells at 1 kHz frequency. The C-V curves are depicted in Figure 3.10. The common behavior is, regardless of a-Si thickness in hybrid cells, capacitance starts increasing around built-in potential even though there is a difference in the slope. However, when we take a look at the capacitance around zero bias closely, the thinner a-Si hybrid cells have the capacitance increasing gradually compared to the thicker one that sustains quite constant value. For the further study on the above different capacitance response versus applied voltage bias, we pursued theoretical analysis on the suggested a-Si photovoltaic

device structures. We believe that our analysis will provide future design guide for such an undoped PV structure in ultra-thin photoactive layer regime.

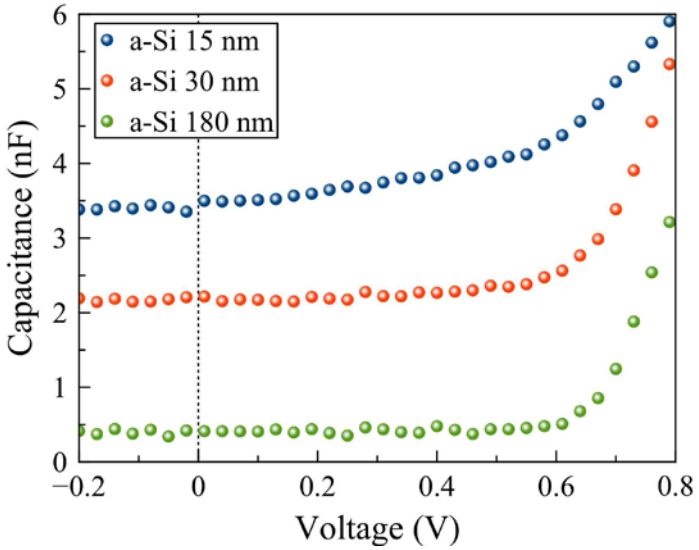


Figure 3.10. Capacitance responses of the a-Si hybrid cells to small voltage signal perturbation with different voltage biases: Capacitance-voltage (C-V) characteristics of the hybrid cells with different a-Si thicknesses.

In the theoretical analysis, we investigated image charge effect on the ultra-thin a-Si hybrid cells since the thinner film reduces the distance between image charges. The capacitance-voltage characteristics according to the image charge effect was exploited as well to find the influence of the previously studied interfacial defects. The energy band diagram of the hybrid cells is changed by the additional electric field of newly formed image charges at the interface between a-Si active layer and anode electrode as shown in Figure 3.11.

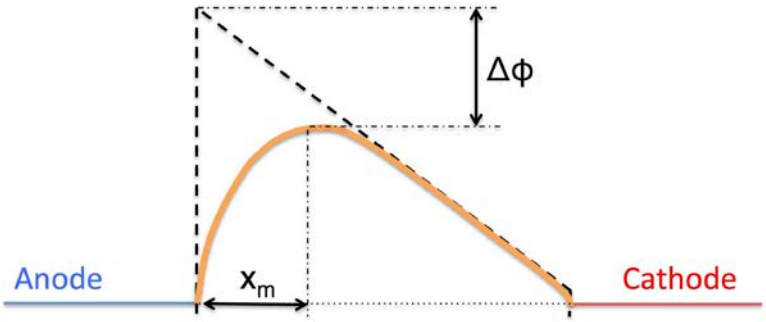


Figure 3.11. Theoretical analysis of the undoped a-Si hybrid cells by investigating energy band diagrams and capacitance-voltage characteristics: Image charge effect at the anode of the hybrid cell with thinner a-Si thickness induces larger energy barrier reduction ($\Delta\phi$).

If the charges are closer across the interface, there will be larger modification of the band diagram due to higher electric field according to the below calculation, eventually reducing energy barrier at the anode. Without considering the image charge effect, we assume the original energy band diagram follows Eq. 3.5 because a-Si that we use is intrinsic or low n-doped if any.

$$dV/dx = -\left(\left(V_{FB} - V_{applied}\right)/w\right) \quad (3.5)$$

The total energy band within the device active layer ($x$) is modified by the image charge effect as Eq. 3.6.

$$E_{total} = -q\left(\left(V_{FB} - V_{applied}\right)/w\right)x - q^2/16\pi\varepsilon_0\varepsilon_r x \qquad (3.6)$$

Since we propose that $V_{FB}$ is same around ~ 0.9 V for the hybrid cells regardless of different a-Si thicknesses based upon the experimental C-V characteristics, we are able

to obtain energy barrier reduction range $x_m$ and the amount of reduction $\Delta\phi$ according to $dE_{total}/dx = 0$ and $V_{applied} = 0$ (zero bias) conditions as shown in Eq. 3.7:

$$x_m = \sqrt{qw/16\pi\varepsilon_0\varepsilon_r V_{FB}}\ ,\ \Delta\phi = \sqrt{qV_{FB}/4\pi\varepsilon_0\varepsilon_r w} \qquad (3.7)$$

Depending on the above calculations, we have larger barrier reduction ($\Delta\phi$) in narrower range ($x_m$) at the anode by creating a shorter depletion width ($w$). Since we assume the 15 nm and 30 nm hybrid cells are completely depleted, we attain around 0.1 V of $\Delta\phi$ and 0.7 nm of $x_m$ for the 15 nm cell, 0.06 V and 1.0 nm, respectively, for the 30 nm cell. The amount of barrier reduction is large enough to affect the device operation of the ultra-thin hybrid cells. We already experimentally demonstrated the performance variation regarding the different a-Si thicknesses in Figure 3.2-3.3.

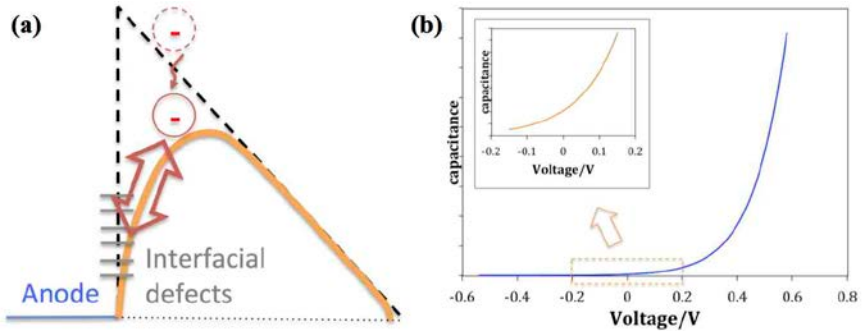


Figure 3.12. Theoretical analysis of the undoped a-Si hybrid cells by investigating energy band diagrams and capacitance-voltage characteristics: (a) Interfacial defects at the anode contribute the capacitance response to the small voltage signal perturbation due to charge capturing and emitting processes by the defects. (b) Theoretical capacitance-voltage characteristics according to the image charge effect and interfacial defects.

In addition, from the C-f characterization (Figure 3.9), we experimentally observed that the thinner film induces more electric charge interaction with interfacial defect density. Since the defects are located at the anode interface where charges to be injected and extracted, if the same voltage perturbation is applied, the total capacitance is influenced by the amount of charges being captured and emitted from the defects (Figure 3.12a). Here we consider not only the barrier reduction by the image charge effect above but also the amount of areal defects ($A_d$) for the calculation of charge concentration ($N$) at the interface:

$$N = C_1 \times e^{C_2\left(V_{applied} + \sqrt{q(V_{FB} - V_{applied})/4\pi\varepsilon_0\varepsilon_r w}\right)} \times A_d \qquad (3.8)$$

The charge capture process should depend on the amount of defects as depicted in Eq. 3.8. As the capacitance is based on the measured AC impedance by small signal voltage perturbation in Keithley 4200 equipment, which is proportional to $dN/dV_{applied}$, we can draw theoretical C-V characteristics as shown in Figure 3.12b. In ultra-thin active layer regime assuming complete depletion in the a-Si layer, the thinner a-Si hybrid cells have shorter depletion width $w$ and larger interactive interfacial defects $A_d$. Thus, the thinner hybrid cells induce the non-ideal larger capacitance increment at zero bias (Figure 3.12b), which supports the experimental result in Figure 3.10. However, for thicker hybrid cells, ideal Mott-Schottky analysis still works since Schottky barrier capacitance mostly follows the depletion region variation but less affected by the interfacial defects. The larger interfacial defect density and the smaller energy barrier at the anode by our theoretical analysis also qualitatively explain the more non-ideal characteristics of the

thinner a-Si hybrid cells in the ultra-thin regime. The experimentally obtained larger ideality factor in the thinner a-Si hybrid cells implies more interfacial recombination during charge extraction due to the larger charge trapping density of defects and barrier reduction.

## 3.3 Transient Photovoltage and Photocurrent

Since the undoped a-Si hybrid PV is firstly demonstrated structure in this dissertation, we began looking into charge transport dynamics by characterizing the transient responses of the hybrid PVs under a light-emitted diode illumination pulse. The schematic diagram of the transient characterization is described in Figure 3.13.

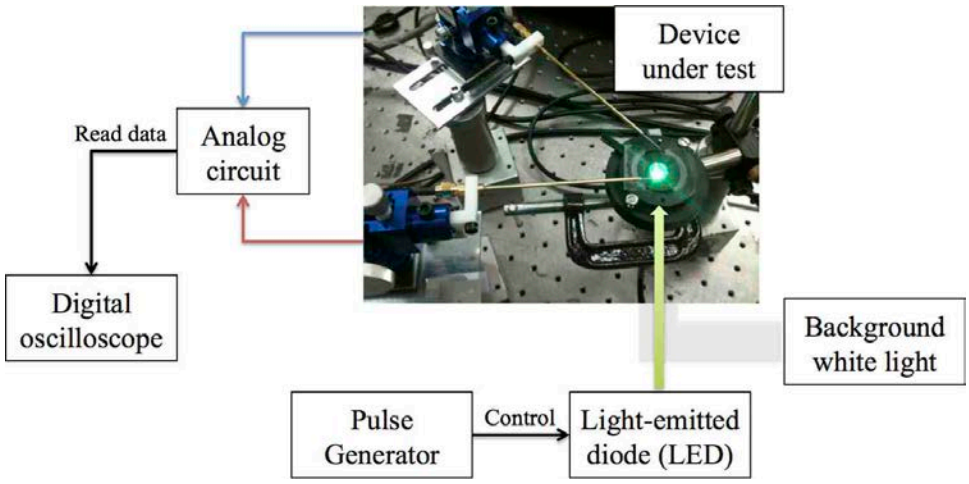


Figure 3.13. A schematic diagram of transient characterization setup: A light-emitted diode (LED), a pulse generator that controls the LED illumination pulse, a background white light for simulating photo condition and helping to find open circuit voltage bias, an analog circuit converting photocurrent and photovoltage to a voltage data for a digital oscilloscope, and a device on an optical stage.

In the transient characterization, a light-emitted diode (LED) pulse illumination is used with a background white light as shown in Figure 3.13. The background white light simulates a steady state photo condition; and the LED pulse gives smaller amplitude perturbation signal to the a-Si hybrid device [6]. Here a pulse generator controls the LED pulse period, duty cycle, and amplitude modulation. In order to acquire transient photocurrent and photovoltage, we use an analog circuit that converts the retrieved signal to a voltage data, which can be eventually read and plotted by a digital oscilloscope. Also the circuit is used to voltage bias the device for open circuit condition with help from the background white light. Lastly, the device is set up on a properly implemented optical stage and probed with xyz-positioned manipulators for cathode and anode contacts. In terms of the device to test, we test the undoped a-Si hybrid PV structure, which is composed of intrinsic a-Si, inorganic metal oxide for hole transport, organic layer for electron, and two electrodes as described in Figure 3.14.

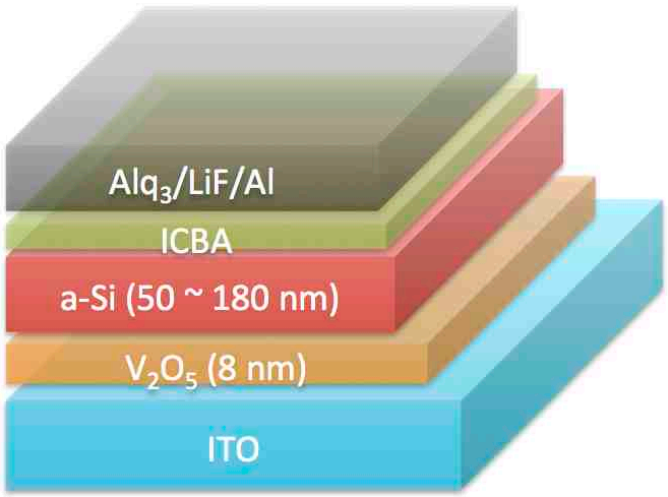


Figure 3.14. Undoped a-Si solar cells with inorganic/organic hybrid charge transport layers: Device structure of a-Si (50~180 nm) hybrid cell with ICBA and $V_2O_5$ for electron and hole charge transports, respectively.

For investigating different charge transport dynamics, the intrinsic a-Si thickness was designed to range from 50 nm to 180 nm to be evaluated by the PV power efficiency characterization in this study (Figure 3.14). For the hole transporting metal oxide, we utilize high work function vanadium(V) pentoxide ($V_2O_5$) [1]. In order to build efficient electron transport, the $C_{60}$ derivative, indene-$C_{60}$ bisadduct (ICBA), is employed at cathode side for Ohmic contact [2]. The cathode is completed with $Alq_3$/LiF/Al configuration as experimentally proved to be effective low work function electrode in our previous report [3]. The simulated sunlight from 1 sun to 7 sun is illuminated to indium-tin oxide (ITO) anode in the device. The concentrated sunlight increases the amount of photogenerated carriers in the hybrid cell, which will be visited later in this chapter.

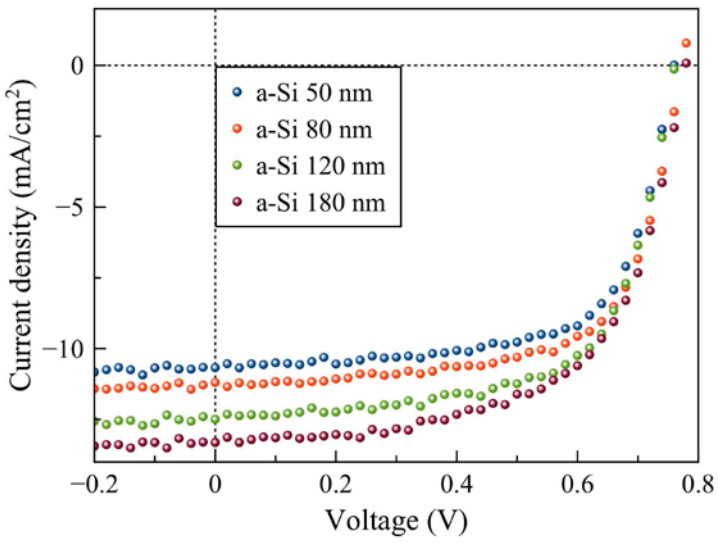


Figure 3.15. Current density-voltage (J-V) characteristics of the hybrid PVs with the different thicknesses of undoped a-Si (50~180 nm) while the other layers remain unchanged in the structure (Figure. 3.13).

Short circuit current density ($J_{sc}$) of the a-Si hybrid cell increases according to the varied a-Si thickness increment with open circuit voltage remained similar (Figure. 3.15). Here what we should note is fill factor (FF) decrease is observed when the a-Si photoactive layer gets thicker. Table I summarizes the PV power efficiency performance with regard to the a-Si thickness. The FF decreases from 68 % down to 62 % in the a-Si thickness change from 50 nm to 180 nm, thereby sacrificing power conversion efficiency improvement.

Table 3.I. Power efficiency performance is summarized for the undoped a-Si hybrid PVs, in which a-Si photoactive layer thickness varies from 50 nm to 180 nm.

| a-Si | $J_{sc}$ [$mA/cm^2$] | $V_{oc}$ [V] | Fill Factor | PCE [%] |
|---|---|---|---|---|
| 50 nm | 10.7 | 0.76 | 0.68 | 5.5 |
| 80 nm | 11.2 | 0.77 | 0.67 | 5.8 |
| 120 nm | 12.5 | 0.76 | 0.65 | 6.2 |
| 180 nm | 13.4 | 0.77 | 0.62 | 6.4 |

In order to verify whether the increased amount of photogenerated charge by the thicker a-Si affects the FF decrease, we apply higher solar concentration to ultra-thin a-Si (30 nm) device and the thick (180 nm) as shown in Figure 3.16.

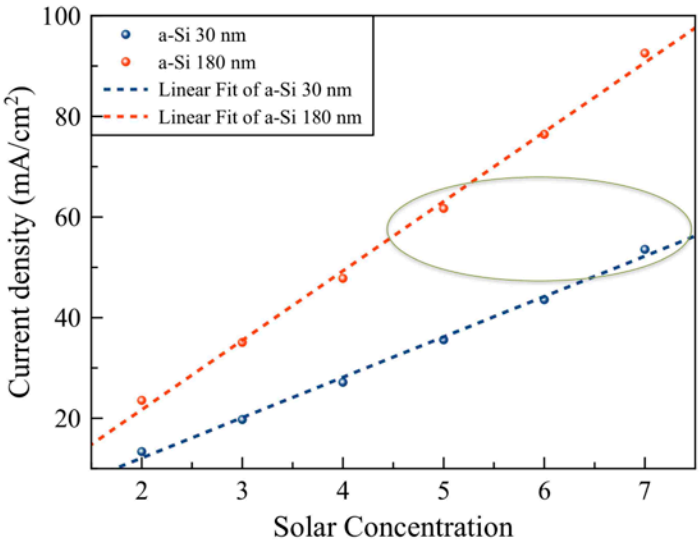


Figure 3.16. Higher solar concentration on the ultra-thin (30 nm) and thick (180 nm) a-Si hybrid cells and its influence on PV performance: Current density of the hybrid cells according to solar concentration. The current density of about 60 mA/cm$^2$ is achieved by 7 sun on a-Si 30 nm devices and 5 sun on a-Si 180 nm as indicated in a elliptical mark.

Figure 3.16 proves that short circuit current density ($J_{sc}$) increment linearly according to the solar concentration. However, in Figure 3.17, we can observe a big difference in FF decrement rate. Up to 7 sun, about 4 % FF decrease, in the a-Si 30 nm device, is less than a half of ~10 % FF reduction in the a-Si 180 nm one. More notably, at the similar $J_{sc}$ level, around 60 mA/cm$^2$, highlighted in Figure 3.16, the a-Si 30 nm device outperforms in FF, bringing about 6 % FF advantage over the a-Si 180 nm, indicated in Figure 3.17. Here we claim that the FF decrease with a-Si thickness increase is not solely caused by the photocurrent increase, but concluding the possible effect from photogenerated carrier dynamics in the hybrid cell, such as bulk recombination rate.

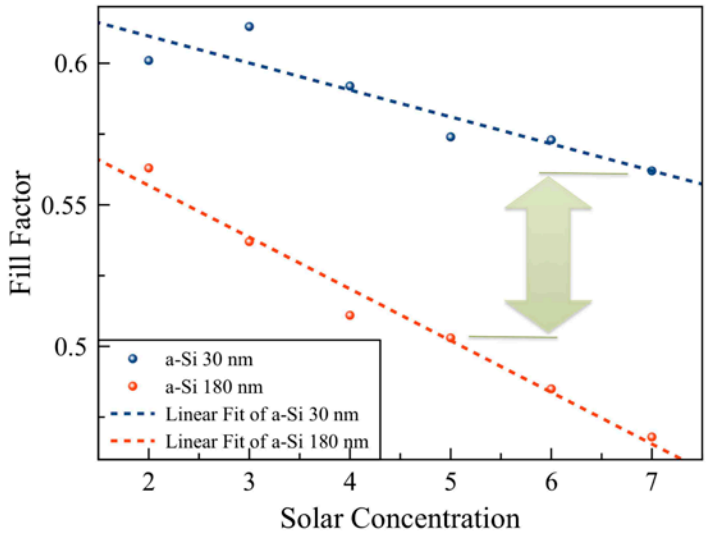


Figure 3.17. Higher solar concentration on the ultra-thin (30 nm) and thick (180 nm) a-Si hybrid cells and its influence on PV performance: Fill factor of both hybrid cells in terms of the concentration. The fill factor decrease in a-Si 180 nm hybrid cell is much more significant than a-Si 30 nm one. The big difference in fill factor, highlighted by a block arrow, is observed with regard to the same current density level (~ 60 mA/cm$^2$) found in Figure 3.16.

As higher photogenerated charge concentration in a unit volume of photoactive layer is not a cause of the reduced fill factor, we presume that the potential high bulk recombination rate can be ascribed to the slow diffusion-based photo-carrier transport without internal electric field [7], [8]. Here we assume that the interfacial surface recombination rate is unvaried to the a-Si thickness change since the a-Si photoactive layer is thick enough as we experimentally discussed in Chapter 3.1.

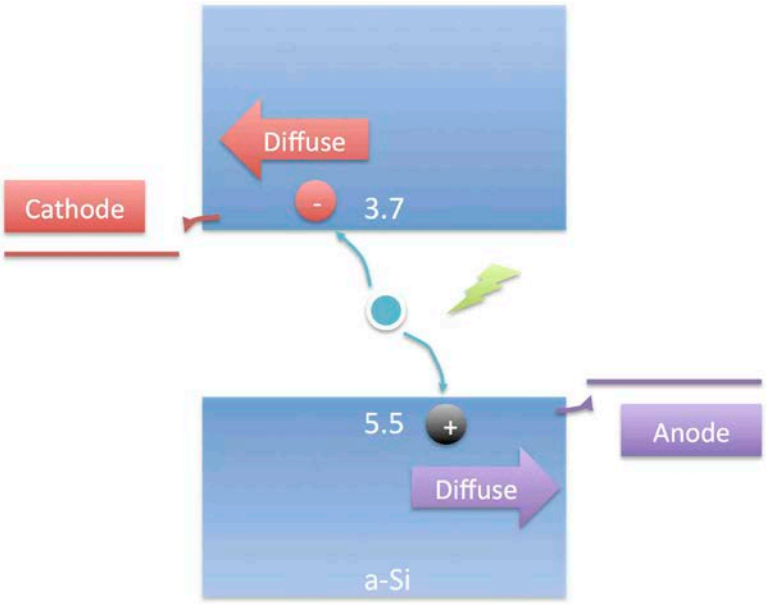


Figure 3.18. Schematics of transient photocurrent upon the photogenerated charge creation at photovoltaic open circuit condition: Photogenerated electrons and holes diffuse to cathode and anode, respectively, thereby producing transient current variation.

Therefore the transient photo-response of our hybrid PVs at open circuit condition is investigated as illustrated in the simplified intrinsic a-Si energy band (Figure 3.18 and 3.19). Upon the short period light pulse perturbation, photogenerated carriers diffuse to respective electrodes (Figure 3.18). We believe that the photocurrent relaxation time by the diffusion process implies a carrier lifetime as well as a diffusion coefficient [8], [9]. Due to Fermi energy level splitting by the light stimulation, the photogenerated charges accumulated in conduction and valence bands induce photovoltage to vary as well (Figure 3.19). The photovoltage response is considered to represent a photo-carrier lifetime in our a-Si hybrid PV since it provides charge annihilation time without an internal electric field at open circuit condition [8], [10].

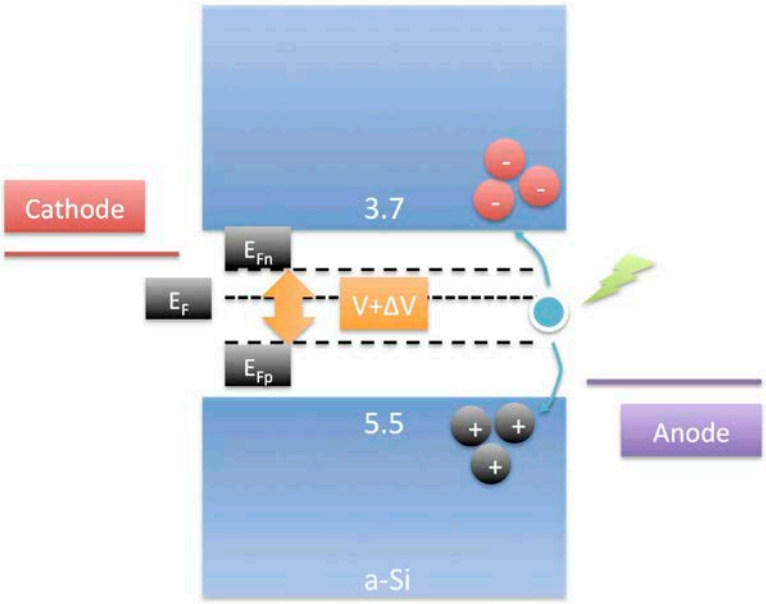


Figure 3.19. Schematics of transient photovoltage upon the photogenerated charge creation at photovoltaic open circuit condition: The photogenerated charges induce Fermi energy level split for transient voltage deviation.

Therefore we are able to exploit an ambipolar diffusion length of our novel a-Si hybrid structure for the first time by investigating the transient photovoltage and photocurrent behaviors [11]-[15]. The ambipolar diffusion length can be inferred as effective diffusion length, or average distance traveled by both carriers before recombination [15], [16]. For the transient characterization, we apply a 500 ns green light-emitted diode (LED) pulse (520 nm peak wavelength) with a white background light to 100 nm-thick a-Si hybrid PVs (Figure 3.19). The white light (Figure 3.13) is selected to be 1 sun-simulated light to emulate the environment of power efficiency measurement [15], and utilized to set a bias voltage for open circuit condition [11]. Here the LED pulse amplitude is designed to be around 20 times smaller than the bias light [15], [17]. With the much lower intensity of green LED light, we minimize the

perturbation amount, thus ensuring mono-exponential decay kinetics in the PV structure [15].

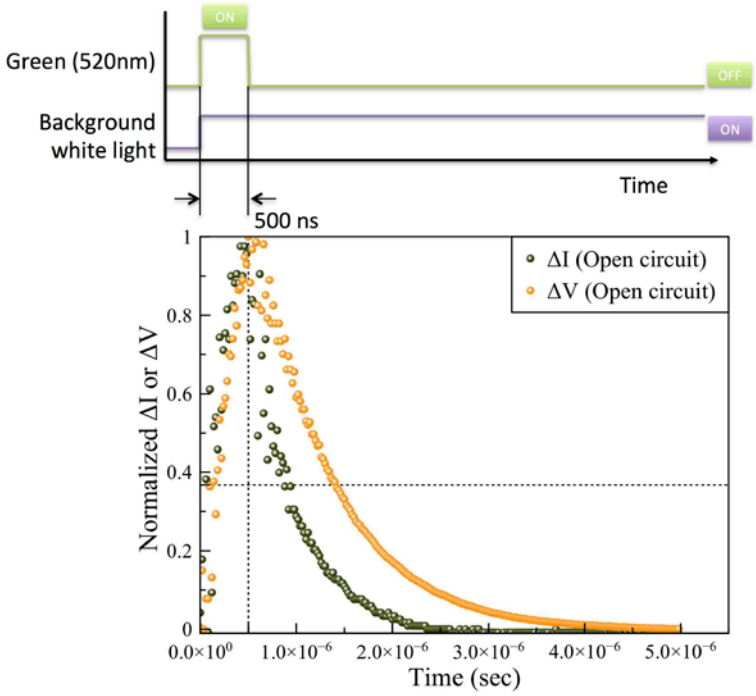


Figure 3.20. The normalized transient current and voltage response of a-Si (100 nm) hybrid cells to green LED source (pulse width of 500 ns) and background white light, which is not only for setting open circuit condition but saturating charge trap sites in the cells. At open circuit condition, the photocurrent relaxation time (blue dots) is shorter than the charge carrier lifetime (red dots).

In order to eliminate the effect of internal electric field, we perform the transient measurement at open circuit condition in the transient response curves as shown in Figure 3.20. All the photovoltage and photocurrent transients are normalized to the same unity value at time 500 ns when peak amplitude reached, which is followed by green LED turn-off. The falling transients of photovoltage and photocurrent are fitted to mono-exponential decay curves, thus showing the time constants of 830 ns and 460 ns,

respectively. From the photovoltage relation with charge density change (Figure 3.19), i.e. electron charge in the a-Si hybrid structure, we can derive Eq. (3.9)

$$n + \Delta n = n_i exp\left(\frac{q(V+\Delta V)}{2kT}\right) \quad (3.9)$$

where $n$ is the initial charge density, $\Delta n$ the additional charge density, $n_i$ the intrinsic charge density, $q$ the elementary charge, $V$ the initial photovoltage, and $\Delta V$ the additional photovoltage. Since we deal with time domain transient responses, the time derivative of the additional charge density is calculated as in Eq. (3.10)

$$\frac{d\Delta n}{dt} = (n + \Delta n) \times \frac{q}{2kT} \times \frac{d\Delta V}{dt} = \frac{nq}{2kT} \times \frac{d\Delta V}{dt}, \qquad \Delta n \ll n \qquad (3.10)$$

Here what we measure experimentally is the additional photovoltage transient, which can be expressed with time constant $\tau$ in Eq. (3.11)

$$\frac{d\Delta V}{dt} \propto \frac{d\Delta n}{dt} = -k_r \Delta n = -\frac{\Delta n}{\tau} \qquad (3.11)$$

where $k_r$ is regarded as charge recombination rate. The time constant in the photovoltage decay represents the lifetime of photogenerated charge without any internal electric field, average 830 ns before recombination. As we have already obtained photogenerated charge lifetime from the photovoltage transient, now the ambipolar diffusion coefficient $D$ can be estimated from the photocurrent relaxation time (460 ns) as depicted in the continuity equation of Eq. (3.12)

$$\frac{d\Delta n}{dt} = D\frac{d^2\Delta n}{dx^2} - \frac{\Delta n}{\tau} \qquad (3.12)$$

Here we note that shorter lifetime of photogenerated carriers induce faster photocurrent relaxation, which will be explained more in Figure 3.21 and 3.22. The further derivation of Eq. (3.12) by analytical solution can be found in Leng *et al*. [13], where we assume Ohmic contact for both charges at respective electrodes. The photocurrent relaxation time $\tau_j$ is described as in Eq. (3.13)

$$\tau_j = \left(\frac{\pi^2 D}{4d^2} + \frac{1}{\tau}\right)^{-1} \qquad (3.13)$$

thus giving the diffusion coefficient in Eq. (3.14)

$$D = \frac{d^2}{2.47}\left(\frac{1}{\tau_j} - \frac{1}{\tau}\right) \qquad (3.14)$$

where $d$ is the a-Si photoactive layer thickness, 100 nm in our measurement. With the single carrier diffusion coefficient and lifetime, we finally calculate the ambipolar diffusion length $L_{amb}$ in the a-Si hybrid structure as shown in Eq. (3.15)

$$L_{amb} = \sqrt{D \times 2\tau} \qquad (3.15)$$

which is around 80 nm by treatment of $2\tau$ lifetime for both carriers (electron and hole) [15], accordingly explaining the FF decrease in our hybrid structure when a-Si gets thicker as experimentally observed in Table 3.I and Figure 3.15. This result potentially implies that intrinsic a-Si property improvement creating the longer carrier diffusion can enhance FF, thus achieving the higher hybrid PV power efficiency. Also the experimentally measured diffusion length can provide a design rule for an undoped photoactive layer in hybrid PV device structures.

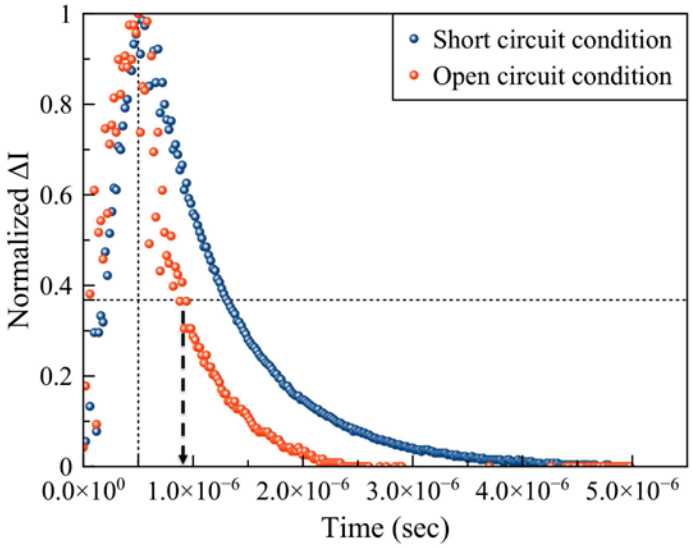


Figure 3.21. The transient response of photocurrent of a-Si hybrid cells at the short and open circuit conditions, which is normalized to peak value at 500 ns: Photocurrent at open circuit is relaxed faster than short circuit condition due to more photogenerated charge recombination loss without any internal electric field for carrier separation. Thus we employ the photocurrent relaxation time at open circuit condition, which only contains the information of carrier diffusion and lifetime, by eliminating the electric field-driven carrier transport.

As previously confirmed, in order to attain diffusion length accurately without internal electric field effect, the transient responses have been measured at open circuit

condition. For further verification of the measured transients, we have pursued the transient characteristics at short circuit condition of the a-Si hybrid PVs as well as compared in Figure 3.21 and 3.22. In Figure 3.21, the photocurrent relaxation is depicted to be slower at short circuit condition than open circuit. We presume that bimolecular recombination in the a-Si photoactive layer is suppressed by the internal electric field at short circuit. The mitigated recombination provides the longer photo-carrier lifetime, thereby elongating the photocurrent relaxation time.

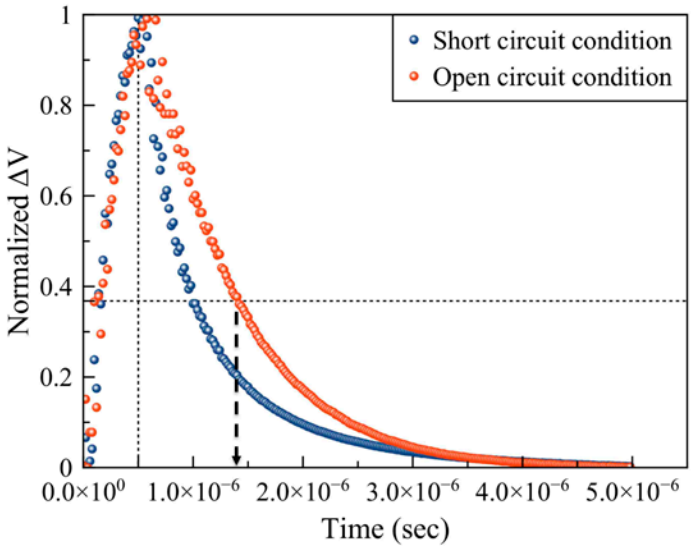


Figure 3.22. The transient response of photovoltage of a-Si hybrid cells at the short and open circuit conditions, which is normalized to peak value at 500 ns: Transient photovoltage response represents carrier lifetime in undoped a-Si active layer. However, at short circuit condition, the photogenerated charges are affected by internal electric field and extracted quickly to respective electrodes, thereby inducing faster carrier loss in the active layer. For accurate carrier lifetime measurement, we attain the response time at open circuit condition.

On the other hand, the photovoltage decays faster at short circuit condition compared to open circuit (Figure 3.22). We should note that photogenerated charges are

swept away and lost out of the a-Si photoactive layer due to the electric field, thereby causing faster photovoltage decrease. Therefore the transient dynamics characterized at open circuit are proved to be right choices for carrier lifetime without unwanted external effect. As a result, according to the extensive electrical performance characterization in this chapter, we investigated and provided what need to be ground rules to design undoped a-Si hybrid PV cells operating for the highest power efficiency.

## 3.4 Conclusion

In conclusion, we have investigated the open circuit voltage change of amorphous silicon (a-Si) hybrid photovoltaic cells with different undoped a-Si thickness down to a few tens of nanometers. The thinner a-Si layer turned out to have higher areal inter-band defect density of states (DOS), thereby deriving larger ideality factor for the thinner a-Si hybrid cells in ultra-thin a-Si regime. We further confirmed the larger ideality factor of the ultra-thin cells by observing larger $V_{oc}$ change under varied sun concentration. According to our theoretical analysis, image charge effect causes energy barrier reduction at the anode, inducing the thinner hybrid cells to turn on at earlier forward bias under dark condition, and to contain larger saturation current at reverse bias. This analysis has been further supported by the empirical characteristics of capacitance-voltage (C-V). We also have reported that a-Si thickness affects photovoltaic power efficiency, especially fill factor in the proposed a-Si hybrid solar cell structure. Larger decrease of fill factor has been observed in a-Si 180 nm device compared to a-Si 30 nm one towards higher solar

concentration up to 7 sun. The fill factor difference attained has been experimentally proved not to be dependent upon the volume density of photogenerated charges. The a-Si thickness dependence on fill factor is further explained by ambipolar carrier diffusion length (around 80 nm) characteristic by transient response at open circuit condition. We believe that our study on the undoped a-Si hybrid cells in ultra-thin a-Si regime provides guidelines how to design the hybrid cells for better performance by incorporating the newly discovered characteristics.

# References


[1] J. Meyer, K. Zilberberg, T. Riedl, and A. Kahn, "Electronic structure of Vanadium pentoxide: An efficient hole injector for organic electronic materials," *J. Appl. Phys.*, vol. 110, no. 3, p. 033710, 2011.

[2] Y. He, H.-Y. Chen, J. Hou, and Y. Li, "Indene−C 60Bisadduct: A New Acceptor for High-Performance Polymer Solar Cells," *J. Am. Chem. Soc.*, vol. 132, no. 4, pp. 1377–1382, Feb. 2010.

[3] J. Y. LEE, T. Lee, H. J. Park, and L. J. Guo, "Improved solar cell performance by adding ultra-thin Alq3 at the cathode interface," *Organic Electronics*, vol. 15, no. 11, pp. 2710–2714, Nov. 2014.

[4] Y. Jia, A. Cao, X. Bai, Z. Li, L. Zhang, N. Guo, J. Wei, K. Wang, H. Zhu, D. Wu, and P. M. Ajayan, "Achieving High Efficiency Silicon-Carbon Nanotube Heterojunction Solar Cells by Acid Doping," *Nano Lett.*, vol. 11, no. 5, pp. 1901–1905, May 2011.

[5] S. Avasthi, S. Lee, Y.-L. Loo, and J. C. Sturm, "Role of Majority and Minority Carrier Barriers Silicon/Organic Hybrid Heterojunction Solar Cells," *Adv. Mater.*, vol. 23, no. 48, pp. 5762–5766, Nov. 2011.

[6] C. R. McNeill, I. Hwang, and N. C. Greenham, "Photocurrent transients in all-

polymer solar cells: Trapping and detrapping effects," *J. Appl. Phys.*, vol. 106, no. 2, p. 024507, 2009.

[7] H. J. Snaith, A. J. Moule, C. Klein, K. Meerholz, R. H. Friend, and M. Grätzel, "Efficiency Enhancements in Solid-State Hybrid Solar Cells via Reduced Charge Recombination and Increased Light Capture," *Nano Lett.*, vol. 7, no. 11, pp. 3372–3376, Nov. 2007.

[8] B. C. O'Regan and F. Lenzmann, "Charge Transport and Recombination in a Nanoscale Interpenetrating Network of n-Type and p-Type Semiconductors: Transient Photocurrent and Photovoltage Studies of TiO 2/Dye/CuSCN Photovoltaic Cells," *J. Phys. Chem. B*, vol. 108, no. 14, pp. 4342–4350, Apr. 2004.

[9] J. van de Lagemaat and A. J. Frank, "Nonthermalized Electron Transport in Dye-Sensitized Nanocrystalline TiO 2Films: Transient Photocurrent and Random-Walk Modeling Studies," *J. Phys. Chem. B*, vol. 105, no. 45, pp. 11194–11205, Nov. 2001.

[10] B. C. O'Regan, K. Bakker, J. Kroeze, H. Smit, P. Sommeling, and J. R. Durrant, "Measuring Charge Transport from Transient Photovoltage Rise Times. A New Tool To Investigate Electron Transport in Nanoparticle Films," *J. Phys. Chem. B*, vol. 110, no. 34, pp. 17155–17160, Aug. 2006.

[11] C. G. Shuttle, B. O'Regan, A. M. Ballantyne, J. Nelson, D. D. C. Bradley, J. de Mello, and J. R. Durrant, "Experimental determination of the rate law for charge carrier decay in a polythiophene: Fullerene solar cell," *Appl. Phys. Lett.*, vol. 92, no. 9, p. 093311, 2008.

[12] S. Grebner, F. Wang, R. Schwarz, Q. Gu, and E. A. Schiff, "Non-Gaussian Transport Measurements and the Einstein Relation in Amorphous Silicon," *Phys. Rev. Lett.*, vol. 76, no. 17, pp. 3196–3199, 1996.

[13] W. H. Leng, P. R. F. Barnes, M. Juozapavicius, B. C. O'Regan, and J. R. Durrant, "Electron Diffusion Length in Mesoporous Nanocrystalline TiO 2Photoelectrodes during Water Oxidation," *J. Phys. Chem. Lett.*, vol. 1, no. 6, pp. 967–972, Mar. 2010.

[14] X. Wang, S. Karanjit, L. Zhang, H. Fong, Q. Qiao, and Z. Zhu, "Transient

photocurrent and photovoltage studies on charge transport in dye sensitized solar cells made from the composites of TiO[sub 2] nanofibers and nanoparticles," *Appl. Phys. Lett.*, vol. 98, no. 8, p. 082114, 2011.

[15] J. Melas-Kyriazi, I.-K. Ding, A. Marchioro, A. Punzi, B. E. Hardin, G. F. Burkhard, N. Tétreault, M. Grätzel, J.-E. Moser, and M. D. McGehee, "The Effect of Hole Transport Material Pore Filling on Photovoltaic Performance in Solid-State Dye-Sensitized Solar Cells," *Adv. Energy Mater.*, vol. 1, no. 3, pp. 407–414, Apr. 2011.

[16] N. Kopidakis, E. A. Schiff, N. G. Park, J. van de Lagemaat, and A. J. Frank, "Ambipolar Diffusion of Photocarriers in Electrolyte-Filled, Nanoporous TiO 2†," *J. Phys. Chem. B*, vol. 104, no. 16, pp. 3930–3936, Apr. 2000.

[17] B. C. O'Regan and F. Lenzmann, "Charge Transport and Recombination in a Nanoscale Interpenetrating Network of n-Type and p-Type Semiconductors: Transient Photocurrent and Photovoltage Studies of TiO 2/Dye/CuSCN Photovoltaic Cells," *J. Phys. Chem. B*, vol. 108, no. 14, pp. 4342–4350, Apr. 2004.

# Chapter 4

# Decorative PV Applications by Ultra-thin a-Si

## 4.1 Introduction

As lower costs and higher efficiencies have driven PV product decisions, present day panels are rigid and heavy while lacking any form of aesthetics. As a result they are primarily installed on rooftops in order to minimize their negative effect on the building's appearance. This type of application excludes an exorbitant amount of surface area that has the potential to increase the building's electric power generation. In Chapter 4, we propose the a-Si hybrid PV structure for decorative PV applications based on low cost materials and scalable manufacturing. This chapter introduces various decorative PV applications, which have been possible due to the unique structure of the proposed a-Si hybrid PVs. The novel hybrid device structure has allowed us to use very thin a-Si layer below 30 nm thickness, which not only satisfies the requirement for semi-transparent color generation and reflective colors, but also minimizes the photo-carrier recombination. The suppressed carrier recombination leads to high quantum efficiency of the device. Moreover the created colors can also be combined to create patterns and logos providing visual options limited only by your imagination. For instance, the semi-

transparent or colored panels can be used as power generating glass facades in building lobbies, windows, or sunshade products. More detail colored PV studies can be found in the following journal papers, J. Y. Lee, K.-T. Lee *et al*., "Decorative power generating panels creating angle insensitive transmissive colors," *Sci. Rep.*, vol. 4, p. 4192, 2014 and K.-T. Lee, J. Y. Lee *et al*., "Colored ultrathin hybrid photovoltaics with high quantum efficiency," *Light: Science & Applications*, vol. 3, p. e215, 2014.

## 4.2 Transmissive Colored PV

The ultra-thin a-Si/organic hybrid solar cells are built on fused silica substrates, comprising an anode, an ultra-thin a-Si layer, and a cathode (Figure 4.1) [1]. The anode structure is designed to transmit a wide range of wavelengths. The electrodes are derived from the dielectric-metal-dielectric (DMD) structures that were developed as ITO-free transparent electrodes [2], [3]. For the anode, the metal and dielectrics are silver (Ag), tungsten trioxide ($WO_3$) and vanadium(V) pentoxide ($V_2O_5$). In particular $V_2O_5$ is interfaced with a-Si and utilized as a transporting layer for the photogenerated holes due to its high work function [4]. A thin Ag (11 nm) is sandwiched between the two dielectric layers in the anode; here the Ag thickness determines the conductivity of the electrode, of which a sheet resistance below 10 ohm/□ is obtained. Perylenetetracarboxylic bis-benzimidazole (PTCBI) [5] is used as a wetting layer underneath the Ag in order to form a smooth and continuous Ag thin film. We did not use Ge as the wetting layer for Ag due to its strong absorption in the visible range [6].

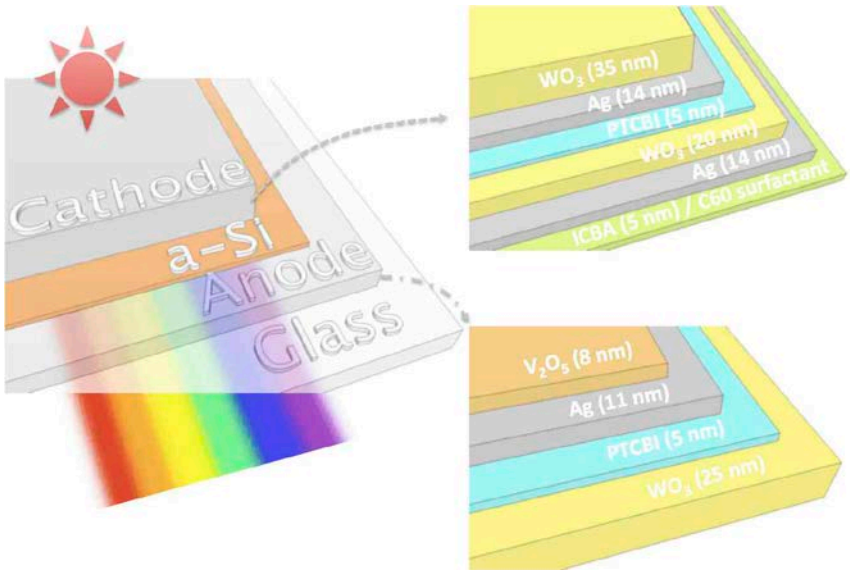


Figure 4.1. A schematic diagram of proposed structure. The structure comprises cathode, anode, and ultra-thin undoped a-Si. The cathode is composed of dielectric-metal-dielectric (DMD) and organic layers, and only DMD structure for the anode. The ultra-thin a-Si layer thickness is 6, 11, and 31 nm for blue, green, and red, respectively [1].

The cathode begins with a thin organic layer, indene-$C_{60}$ bisadduct (ICBA) [7], which operates as a very efficient photogenerated electron transport layer since its lowest unoccupied molecular orbital (LUMO) level is well aligned with a-Si conduction energy band. The ICBA is followed by another organic material of bis-adduct fullerene surfactant ($C_{60}$ surfactant) [8], which effectively lowers the Ag work function and forms ohmic contact for the electrons. The cathode is completed with the combination of Ag and $WO_3$ with different thicknesses according to our theoretical calculation (Figure 4.1). All the anode and cathode materials, except ICBA and $C_{60}$ surfactant, were thermally evaporated consecutively without breaking the vacuum (base pressure $1\times10^{-6}$ mbar). The ICBA and $C_{60}$ surfactant were spin casted all in the same conditions as well. The undoped a-Si layers were deposited by using a plasma enhanced chemical vapor deposition

(PECVD) tool. To produce the blue, green and red colors, 6, 11, and 31 nm of a-Si were deposited, respectively.

In our anode design, a thin Ag layer is also utilized to increase the reflection at the interface with $V_2O_5$, consequently enhancing a quality factor (Q-factor), which yields a narrow resonance bandwidth. Ag is selected for both top and bottom electrode since Ag has the highest reflectivity and the lowest absorption at visible frequencies. A strong resonance behavior arises from the cavity comprising a highly lossy material, a-Si, sandwiched by the two electrodes. Though ICBA, $C_{60}$ surfactant, and $V_2O_5$ layers can contribute to the resonance, we found that the resonance is primarily determined by the a-Si layer due to the high refractive index of a-Si.

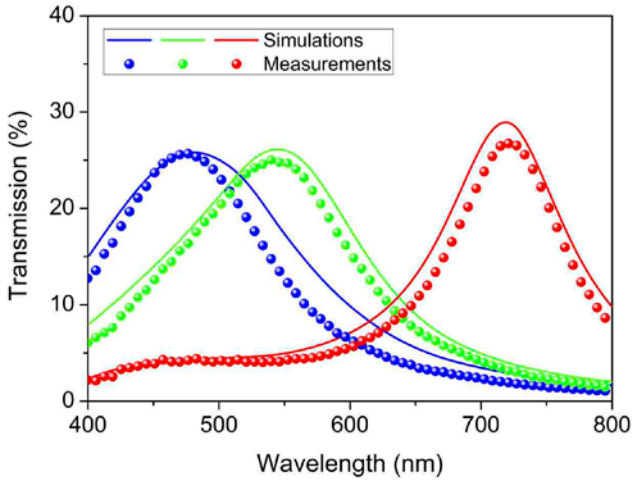


Figure 4.2. Calculated and measured transmission spectra of individual colors (blue, green, and red) at normal incidence.

The calculated (solid line) and the measured (dotted line) transmission spectra of individual colors of devices with varied a-Si thickness at the normal incidence are depicted in Figure 4.2. We performed all the optical simulation by using a transfer matrix method based on the measured refractive index of each material. The experimental spectra show an excellent agreement with the simulated profiles. The a-Si thicknesses of 6 nm, 11 nm, and 31 nm determine the transmission peaks located at 478 nm (blue), 542 nm (green), and 720 nm (red), respectively, while the thicknesses of all other layers remain the same for all devices.

Figure 4.3. Photographs of distinct blue, green, and red colors by the fabricated devices.

The photograph images of fabricated samples are shown in Figure 4.3. It is obvious to see the water fountain and buildings through our devices with distinct colors. It is noteworthy to mention that there is no change in color even with oblique angles of incidence, which will be discussed more in detail in the following section. This simple fabrication process involving only film deposition can be easily scaled to large area substrate for industry level production.

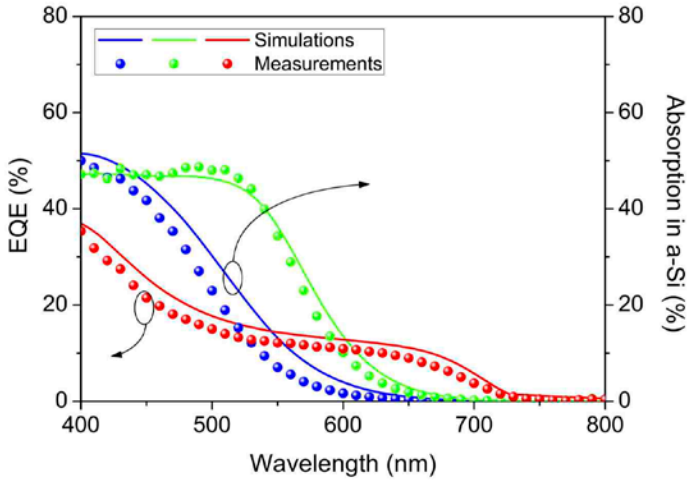


Figure 4.4. Numerical simulation for a-Si absorption and electrical performance of the hybrid cells: Comparison of calculated incident light absorption profiles by ultra-thin a-Si layer and measured external quantum efficiency (EQE) spectra for three different types of devices (blue, green, and red).

For the blue, green, and red device types (Figure 4.3), absorption spectra of a-Si active layers versus wavelength were calculated as shown in Figure 4.4. Remarkably, the electrically measured external quantum efficiency (EQE) profiles are well matched with the calculated absorption spectra. The EQE characterization set up will be discussed in Chapter 5. The EQE spectrum represents actual incident photon-to-charge conversion efficiency and is determined by the light absorption by the active layer and the internal quantum efficiency of the photoactive/transporting layers. The close match between the calculated a-Si absorption and the measured EQE curves implies that the internal quantum efficiency is approaching 100 %. This can be attributed to the strongly suppressed electron-hole recombination in our ultra-thin a-Si hybrid cells.

Regardless of device types (blue, green, or red), the a-Si layer thickness is much thinner than the typical charge diffusion length in a-Si [9], [10] so most photogenerated charges are extracted to the metal contacts through the electron and hole transporting layers. Furthermore the suppressed charge recombination can significantly mitigate the light-induced degradation, which is a drawback of traditional a-Si solar cells [11]-[13]. Many previous studies have focused on optimizing p- and n- layer thicknesses to lessen the charge loss in the doped regions without sacrificing an internal electric field [14]. Our devices with undoped a-Si active layer do not suffer from the charge recombination with p- and n- dopants as in the traditional a-Si PV, which is one of major charge loss mechanism in p-i-n a-Si solar cells [14]-[16].

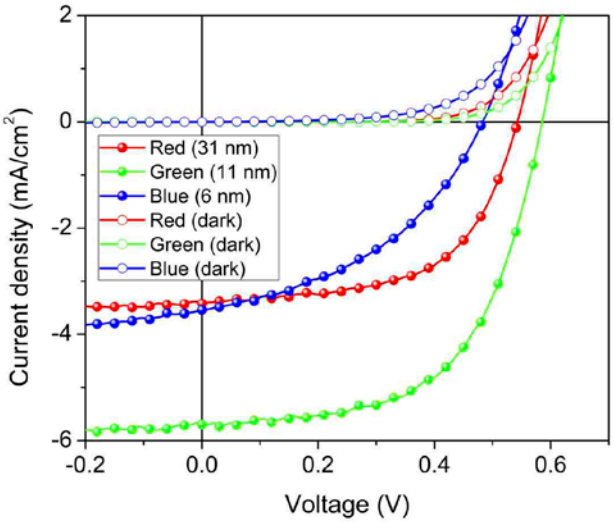


Figure 4.5. Current density-voltage (J-V) characteristics of the hybrid cells, transmitting blue, green, and red colors, under AM1.5 illumination and dark conditions.

Because the EQE of our devices directly correlates with the calculated light absorption in a-Si layer, we can estimate the electric current from the simulated optical

absorption spectrum in an active layer with good accuracy. As the total number of photons absorbed in the active layer is very similar to the total extracted charges, we can design the electric current performance of the solar cells simply based on the optical calculation before fabricating devices. Based on this understanding, an interesting finding is that we expect to obtain higher photocurrent from the green color cell than the red cell (Figure 4.4), even though the a-Si layer thickness for the former (11 nm) is much thinner than that of the latter (31 nm).

To verify this prediction, we measured current density-voltage characteristics under AM1.5 illumination and dark conditions. The device measured has a diameter of 1 mm as in EQE characterization. The current density-voltage curves in Figure 4.5 show the average efficiency performance of multiple devices for each type (red, green, or blue). As we expected from the calculated light absorption in the a-Si layer and EQE spectra previously, the green device has much higher current density (5.69 $mA/cm^2$) than the red one (3.42 $mA/cm^2$) with comparable fill factor (58~59 %). The green color device generates almost 2 % power efficiency by only 11 nm of a-Si active layer. This is a remarkable result if comparing with the ~10 % efficiency obtained in traditional a-Si PV with more than twenty folds a-Si thickness [17].

Most prominently, the blue color device with only 6 nm of a-Si active layer operated well as a solar cell even though the fill factor of the blue device is lower than the other types of devices. We presume that a few nanometer a-Si active layer of the blue device induces more electric charge leaking paths in the device area, thereby reducing

shunt resistance of the solar cell compared to the red and green devices that have thicker a-Si active layers. Therefore, in terms of open circuit voltage ($V_{oc}$), the blue color device has smaller one than the others. The red color device with the thickest a-Si (31 nm), however, has lower $V_{oc}$ than the green color one (a-Si 11 nm) due to much lower photogenerated charge density in the a-Si photoactive layer. Such reduced photocurrent density causes lower photocurrent density in Eq. 1.4, as discussed in Chapter 1.3, consequently suppressing $V_{oc}$. Overall, experimentally, we confirmed that three types of devices (red, green, and blue) worked well for electric power efficiency, generating short circuit current density as designed in our optical simulation. Other thin-film inorganic materials can potentially borrow this novel concept of our hybrid cells for higher power efficiency, filtering various colors based on appropriate photon management in their active layers.

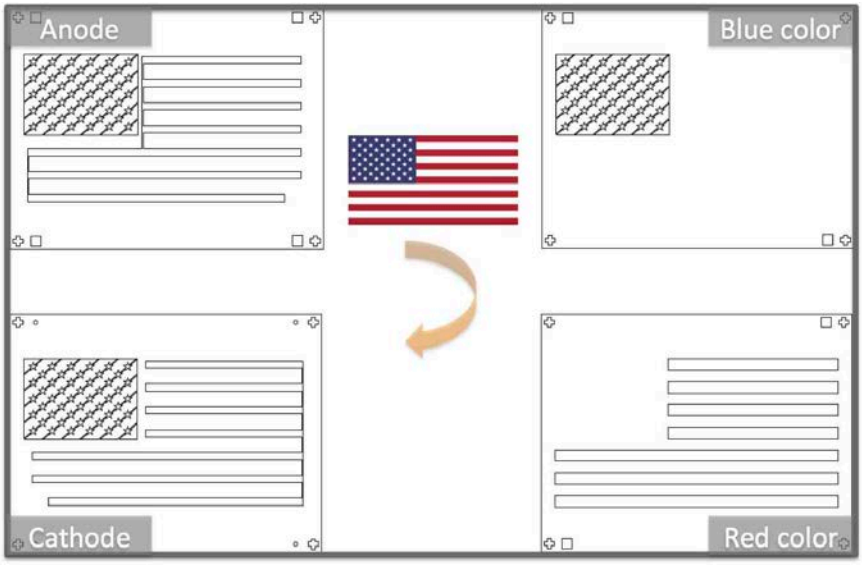


Figure 4.6. Four different shadow masks designs for anode, blue color region, red color region, and cathode, combined to fabricate the power-generating U.S flag photovoltaics.

As a further demonstration, we fabricated a 3 in × 2.3 in power-generating sample in the form of the national flag of the United States (U.S. flag) by designing 4 different shadow masks shown in Figure 4.6. The blue and red regions of the flag use a-Si thickness of 6 nm and 31 nm, respectively, same as in the individual colored samples discussed earlier. The overlapped shadow masks are depicted to predict an overall design of the power-generating U.S. flag in Figure 4.7.

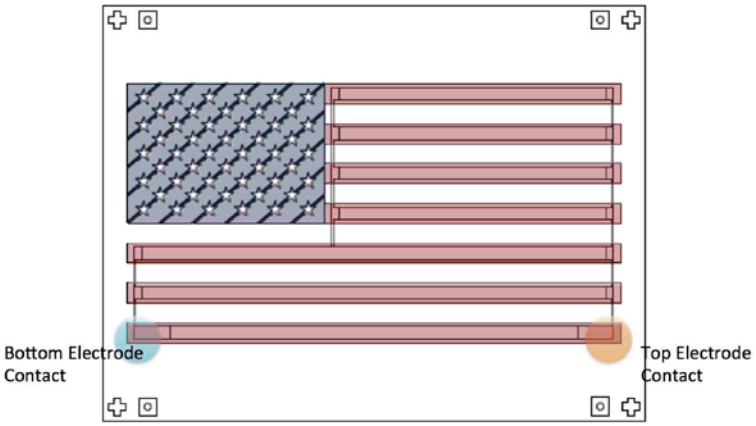


Figure 4.7. The overlapped shadow masks to emulate an overall design when the power-generating U.S. flag is fabricated to operate as a solar panel.

The real fabricated power-generating U.S. flag shows blue and red patterns clearly in Figure 4.8. Since the U.S. flag solar panel provides transmissive colors, we see the colors with bright background such as skylight (Figure. 4.8)

Figure 4.8. The demonstration of the electric power-generating national flag of the United States of America (U.S. flag): Photograph of the U.S. flag taken at the University of Michigan campus shows distinct blue (6 nm) and red (31 nm) color patterns.

In addition, an angle of incidence is changed from normal to 60° in order to verify the angle invariance performance of the power-generating U.S. flag. Indeed, the distinct blue background of the stars and the red stripes in the U.S. flag can maintain their respective colors at oblique angles of incidence as described in Figure 4.9.

Figure 4.9. The demonstration of the electric power-generating national flag of the United States of America (U.S. flag): According to angle insensitive property, the U.S. flag maintains its colors at oblique angles of incidence up to about 60°, manually controlled.

The angle robustness of our devices is due to the use of ultra-thin a-Si, which results in relatively insignificant phase change accumulated as light propagates through the ultra-thin a-Si layer as compared to the phase shift upon reflection at the interface. Thus the resonance can remain fairly unvaried as the angle of incidence increases due to negligible phase shift. The angle robustness and wide angle acceptance is also beneficial for the solar panel deployment in which no external sun tracking systems are needed [18], [19].

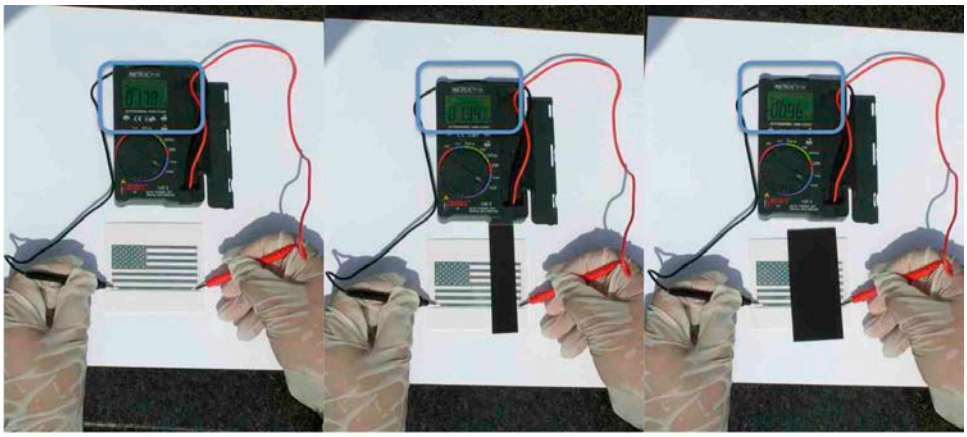

Figure 4.10. The demonstration of the electric power-generating national flag of the United States of America (U.S. flag): The U.S. flag generates electric current as well under outdoor sunlight (less than AM1.5). The electric current level decreases as the U.S. flag gets covered more by a piece of black paper.

In terms of electric power performance, the total colored regions (~1.5 $in^2$) of the U.S. flag generates almost 2 mA electric current under real outdoor sunlight (less than AM1.5) with full light exposure to the flag (Figure 4.10). When the flag is partially covered by a piece of black paper, the current level evidently drops by the ratio of the unblocked flag area.

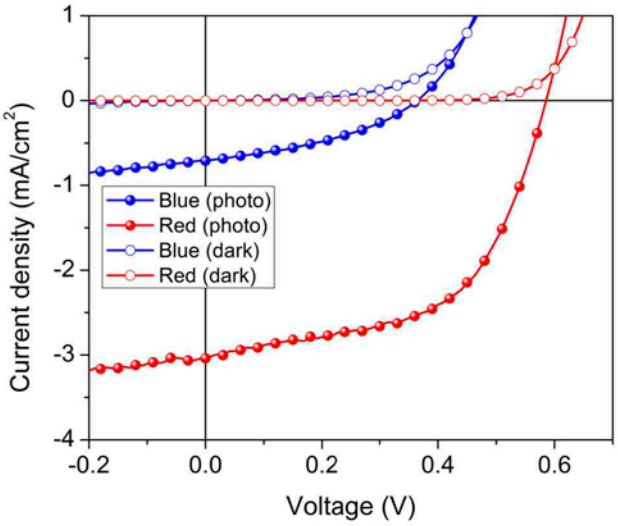


Figure 4.11. The demonstration of the electric power-generating national flag of the United States of America (U.S. flag): Current density-voltage (J-V) performances of blue and red colored 1 mm diameter devices under AM1.5 illumination.

We also measured current density-voltage characteristics by 1 mm diameter devices in the same U.S. flag sample (Figure 4.11). We note that the other transmission colors can be readily realized by simply tuning the a-Si layer thickness.

## 4.3 Reflective Colored PV

The reflective colored a-Si/organic hybrid solar cells are built on transparent fused silica substrates. The main components of the hybrid cells are an anode, an ultra-thin a-Si layer, and a cathode with thick silver (Ag) as shown in Figure 4.12. For the anode, a dielectric-metal structure (i.e. tungsten trioxide ($WO_3$)-Ag) is used in order to produce a relatively high transmission. Following the anode, a high work function vanadium(V) pentoxide ($V_2O_5$) [4] is introduced as a hole transporting layer for the undoped a-Si, which simultaneously blocks electrons. Following a-Si layer deposition, a thin organic layer, indene-$C_{60}$ bisadduct (ICBA) [7] is deposited to serve as an electron transporting layer for a-Si because its lowest unoccupied molecular orbital (LUMO) is well aligned with a-Si conduction energy band. Another organic material of bis-adduct fullerene surfactant ($C_{60}$ surfactant) [8] is spin casted on top of the ICBA, which makes the Ag work function lower, thus forming Ohmic contact between ICBA and thick Ag cathode.

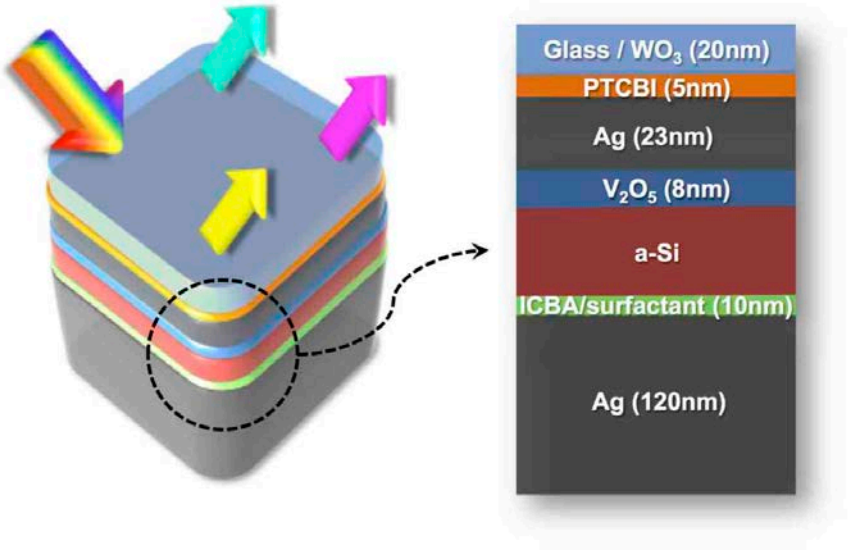


Figure 4.12. A device structure of proposed reflective colored hybrid cells. A cathode comprises thick silver (Ag) and an organic layer, and dielectric-metal structure is for an anode. Between the two electrodes, an ultra-thin a-Si layer is located.

We design a-Si ultra-thin in the hybrid structure (Figure 4.12) so that we can have the strong Fabry-Perot (F-P) resonance formed between the reflecting electrodes [18]. The device produces high absorption of a certain wavelength component while reflecting the complementary spectrum. By simply varying the thickness of a-Si layer inside the F-P resonator, different colors can be obtained. For example, in Figure 4.13, in order to create the cyan, magenta, or yellow (CMY) colors, a-Si layers of 27, 18, and 10 nm thicknesses were used, respectively, and the corresponding resonances (reflection dip) are found at 630, 560, and 480 nm. Figure 4.13 shows the measured and simulated reflection spectra at the normal incidence, which shows excellent agreement between the two. It is worth noting that the a-Si absorption becomes insignificant toward longer wavelength, which results in lessened propagation loss through the a-Si film, accordingly narrowing the

bandwidth. Therefore the cyan colored device has the sharpest resonance among the three colors shown in Figure 4.13.

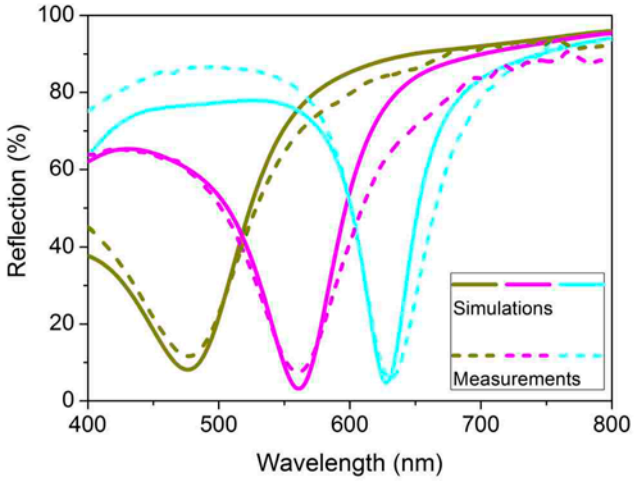


Figure 4.13. Calculated (solid lines) and measured (dotted lines) reflection spectra of cyan, magenta, and yellow (CMY) colors at normal incidence. The thicknesses of a-Si layer for CMY colors are 27, 18, and 10 nm, respectively, given fixed thicknesses of all the other layers in Figure 4.12.

In the anode structure (Figure 4.12), a thin Ag layer (23 nm) forms a semi-transparent anode, and also provides sufficient reflectivity necessary to form the F-P resonance with the thick Ag cathode reflector. Additionally, the thickness of Ag determines conductivity of the anode, of which sheet resistance is below 6 ohm/□. A wetting layer, perylenetetracarboxylic bis-benzimidazole (PTCBI) [6], is utilized for continuous Ag film formation, which can reduce the scattering loss significantly. Even though the bandgap of PTCBI is 2.2 eV, it is found that the absorption loss of a few nanometers PTCBI layer is trivial. We should point out that the behavior is quite different if the PTCBI is replaced by Ge, a commonly used seed layer for thin Ag film [6], as Ge

causes much more significant absorption in the visible range, which we explain similarly in Chapter 4.1. All the anode and cathode materials, except ICBA, were thermally evaporated for the same thicknesses, regardless of device types, without breaking the vacuum below $1x10^{-6}$ mbar. The ICBA was spin casted as described in Chapter 2.2. The undoped a-Si layers were deposited by a plasma enhanced chemical vapor deposition (PECVD) tool (Chapter 1.2) for colored PV devices.


Figure 4.14. Light incident angle behaviors for reflective colors: Images of the fabricated devices showing obvious CMY colors. The colored cells clearly demonstrate the angle insensitive performance at large angles of incidence (15°, 30°, and 60°).

In terms of the reflective colors created by a-Si hybrid PVs (Figure 4.14), they show strong angle-independent colors maintaining the reflection spectra in Figure 4.13. The pictures of the fabricated colored PVs at different angles of incidence (15°, 30°, and 60°) are illustrated as well in Figure 4.14 and the CMY colors show high contrast and do not change their color appearance even at high viewing angle. The reason for the strong angle-independent resonance is same as what has been already discussed in Chapter 4.1 regarding the transmissive colored PVs. The a-Si ultra-thin cavity where the thickness of the absorbing material is much smaller than the wavelength of the incident light enables

the angle insensitivity [19]-[22]. Experimentally, the angular behaviors are measured and confirmed by a variable angle spectroscopic ellipsometer (VASE) from angle of 15° to 60°.

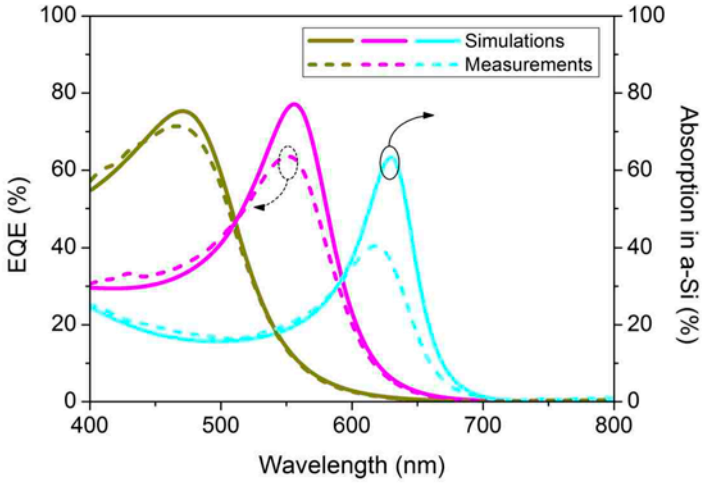


Figure 4.15. Electrical characterizations of fabricated dual-function devices: Measured external quantum efficiency (EQE) spectra and calculated absorption profiles in a-Si layers for three individual colors, cyan, magenta, and yellow.

Next we introduce the benefit of the hybrid cell structure in facilitating the photogenerated charge extraction to the electrodes with significantly reduced recombination. In Figure 4.15, the simulated absorption spectra of a-Si active layers for the CMY colored cells are compared with the measured external quantum efficiency (EQE) for these devices. Overall the two spectra match remarkably well. This means that most of the absorbed photons are harvested and contribute to the photocurrent with negligible electron-hole recombinations. This is because the active layer thickness is much smaller than the typical charge diffusion length in a-Si as experimentally attained in Chapter 3.2 [9], [17], thus most photogenerated charges are efficiently extracted to

electrodes via the organic/inorganic (electron/hole) transporting layers. Towards the longer wavelength peak of absorption, the EQE spectrum shows a little lower profile than the simulated a-Si absorption. This discrepancy is attributed to the broadened density of states of a-Si, inducing more trap-assisted transport, nearby energy band edge as explained in Chapter 1.2. Even if photons get absorbed by a-Si at longer wavelength, showing quite good match between the calculated and the measured (Figure 4.13), the photogenerated charge transport cannot be as efficient as shorter wavelength due to the low-quality transport mechanism, such as hopping from site to site.

Considering the EQE characteristics of the hybrid cells illustrated in Figure 4.15, we expect to have a fairly similar electric current performance from the yellow cell (10 nm) and the magenta cell (18 nm) even though their thicknesses are almost twice different. For experimental evidence, the current density-voltage curves in Figure 4.16 show the average efficiency performance measured from multiple devices for each color type (cyan, magenta, or yellow). The yellow device has very similar current density (6.50 $mA/cm^2$) to the magenta one (6.79 $mA/cm^2$), having comparable fill factor above 60 %. Importantly the magenta device generates almost 3 % power efficiency with only 18 nm of undoped a-Si active layer. This is a remarkable result if comparing with the 10 % record efficiency obtained from a single-junction cell by using 250 nm intrinsic a-Si layer [17], which is over 10 times thicker than our device. It shows that the efficient photon management by optical resonance and the reduced charge recombination in ultra-thin a-Si plays a crucial role in our reflective colored cells. Notably, all three types of devices, regardless of their thicknesses (10 - 27 nm), operated well having fill factor over 60%.

The devices for both optical and electric performance evaluations were all fabricated in the same process.

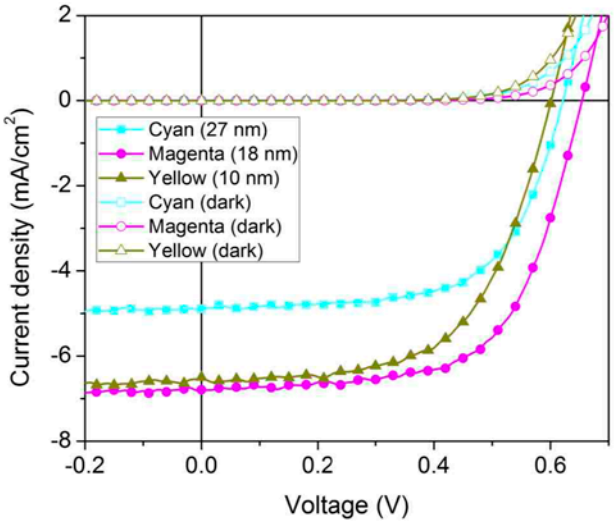


Figure 4.16. Electrical characterizations of fabricated dual-function devices: Measured current density-voltage (J-V) characteristics of individual colored cells under both AM1.5 illumination and dark conditions.

As a demonstration, we fabricate the electric power-generating University of Michigan (U of M) logo (3 inch by 2.3 inch) by designing four different shadow masks as described in Figure 4.17.

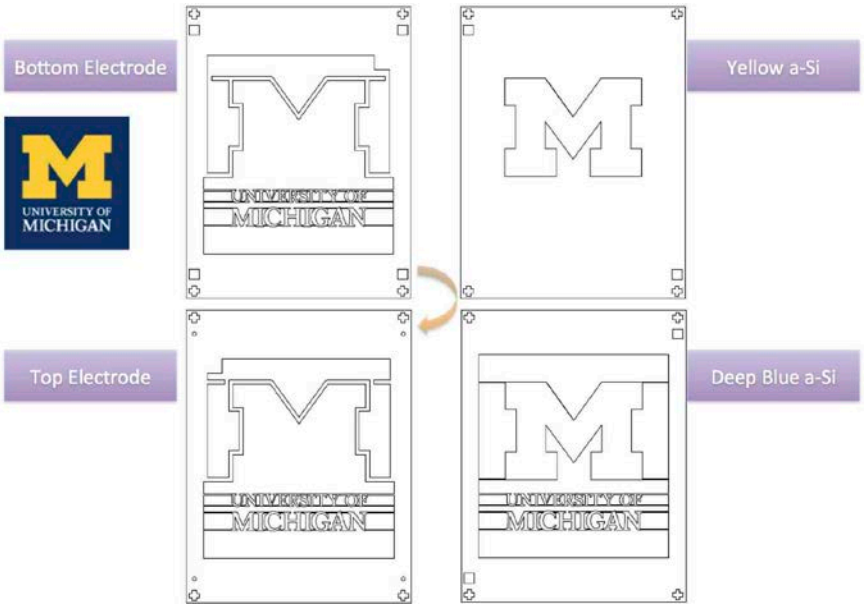


Figure 4.17. Four different shadow masks designs for bottom electrode, yellow (maize) color region, deep blue color region, and top electrode, combined to fabricate the power-generating University of Michigan (U of M) logo photovoltaics.

The overlapped image of the four different shadow masks (Figure 4.17) is illustrated to predict an overall design of the power-generating U of M logo in Figure 4.18.

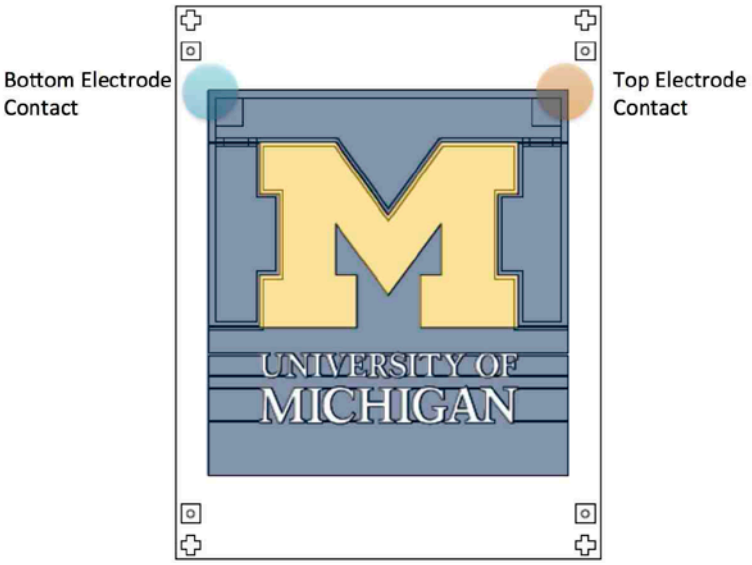


Figure 4.18. The overlapped shadow masks to emulate an overall design when the power-generating U of M logo is fabricated to operate as a solar panel.

As a real fabricated solar panel, the vivid maize and blue colors and patterns on the U of M logo panel are shown in the picture (Figure 4.19). The current density-voltage performances of 1 mm diameter devices are depicted in Figure 4.20. In principle, any colored images can be designed by using shadow masks for colored PVs.


Figure 4.19. The demonstration of the electric power-generating U of M logo: Photograph of the U of M logo panel consisting of maize and blue colors, which is successfully realized with generating electric power.

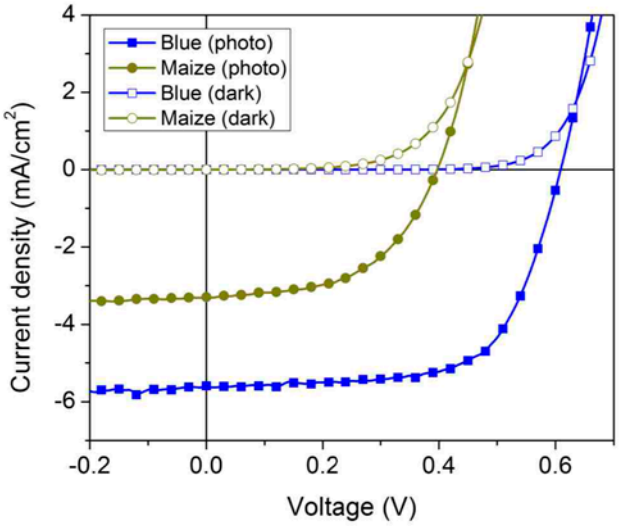


Figure 4.20. Current density-voltage characteristics of the maize and blue colored 1 mm diameter devices on the power-generating U of M logo panel under AM1.5 illumination.

Finally we suggest another innovative use of the reflective colored PVs. Recently there have been increased interests in the spectrum splitting approach to spread the solar spectrum into multiple bands and use the semiconductor PVs with the appropriate bandgap for each band. This approach has the potential to reach record high efficiency without having to engineer the sophisticated vertical tandem cell structures for broadband absorption. However spectrum-splitting approaches always require a specifically designed external element to spread the spectrum, such as filter [23], grating [24], prism [25], or beam splitter [26]. Such external element is not required for our proposed cascaded configuration as shown in Figure 4.21: owing to the strong resonance behavior, our colored PV device can absorb a certain spectral band of the solar light and naturally reflect its complementary spectrum, which can be harvested by another cell with different resonance wavelength.

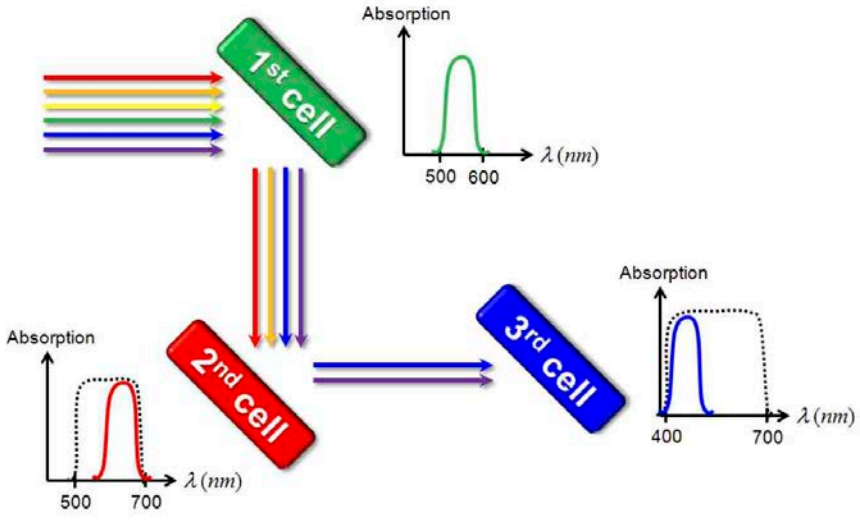


Figure 4.21. The realization of photon recycling with the spectrum splitting of the cascaded light absorption: A schematic showing the arrangement of each cell. The light is reflected by the first cell, which mainly absorbs the green spectrum (thus reflecting magenta color that encompasses the blue and red spectral regions) and goes toward the second cell having a resonance corresponding to the absorption peak at the red, which

harvest the longer wavelength components. By putting the third cell with the creation of yellow color (absorption peak at the blue), the remaining part of incident light, which still contains strong blue spectrum, is recycled.

Simply altering the thickness of a-Si layer in the PV cell enables the resonance to be shifted in a controllable manner. The angle-insensitive behavior is also advantageous for cascading multiple stages of PV cells. As a demonstration, we construct a cascaded solar cell platform by a spectrum splitting as illustrated in Figure 4.21, thus spanning a wide range of wavelengths. We designed and fabricated three cells with different thickness of a-Si, showing different resonance. Light is incident at an oblique angle on the first cell absorbing the green band, and hence reflecting its complementary colors. The longer wavelengths in the unabsorbed spectrum are re-utilized by the second cell whose resonance is at 630 nm. Lastly, the third cell harvests the remaining photons in blue region. Note that the color of each cell in Figure 4.21 represents its primary absorption area. The accumulated absorption spectra are denoted by dotted curves.

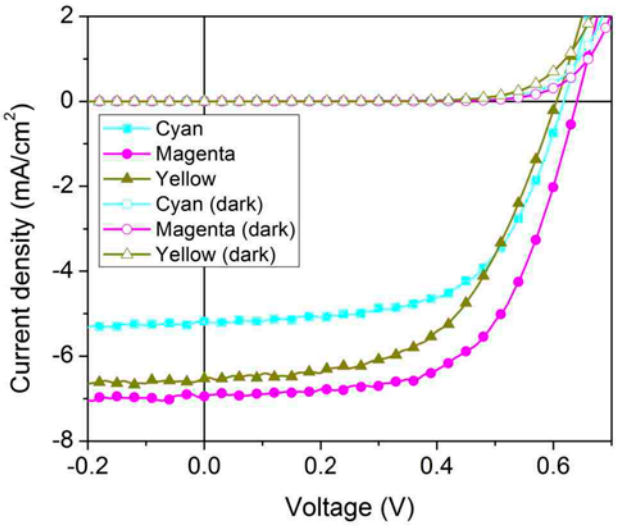


Figure 4.22. The realization of photon recycling with the spectrum splitting of the cascaded light absorption: Current density-voltage (J-V) characteristic of the individual CMY cell under AM1.5 illumination.

The individual cells, without being in the cascaded formation, show current density-voltage (J-V) characteristics as depicted in Figure 4.22. Based on these individual cells, in order study further the optical and electrical characteristics of the cascaded system, we calculated the absorption spectrum in a-Si, and measured EQE of the three cells, which are compared in Figure 4.23. In general, the calculated spectra are quite consistent with the experimental EQE data with a discrepancy at longer wavelengths, which was explained earlier (See the explanation related to Figure 4.15).

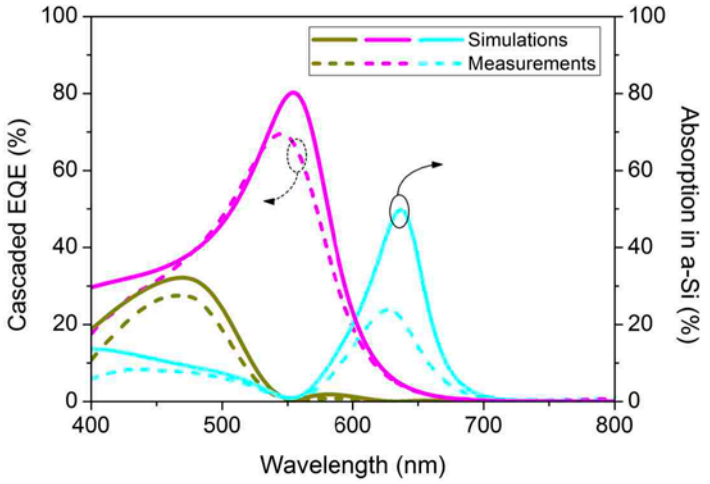


Figure 4.23. The realization of photon recycling with the spectrum splitting of the cascaded light absorption: After the application of the cascaded platform, the experimentally achieved external quantum efficiency (EQE) data and the corresponding numerical absorption spectra in ultra-thin a-Si layer are illustrated.

From the overall EQE and a-Si absorption spectra shown in Figure 4.24 (sum of three profiles), it is obvious that broad range of incident light from 400 to 700 nm can be harvested to generate electric power, which validates the cascaded cell concept.

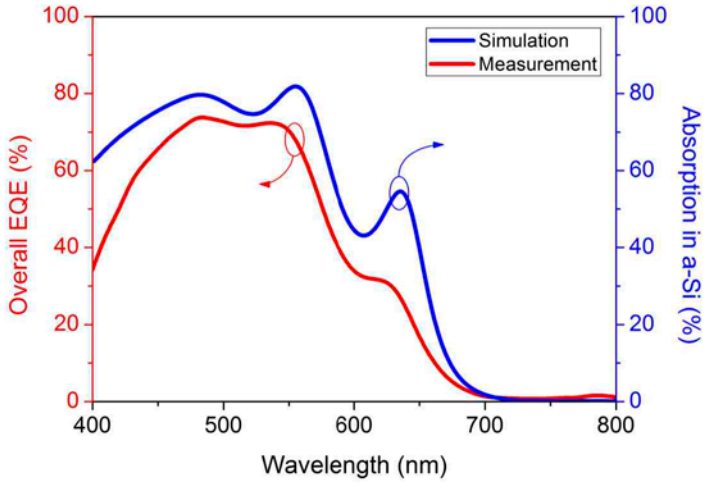


Figure 4.24. The realization of photon recycling with the spectrum splitting of the cascaded light absorption: Overall EQE profile is attained by adding three individual EQE spectra, and associated simulation result of total absorption in three a-Si layers is compared.

However, in the current density-voltage (J-V) characteristics of the cascaded cells (Figure 4.25), they clearly show that the short circuit current density of the second and third cells gets further reduced as the consecutive cells receive less amount of light for a-Si absorption, compared to the first cell.

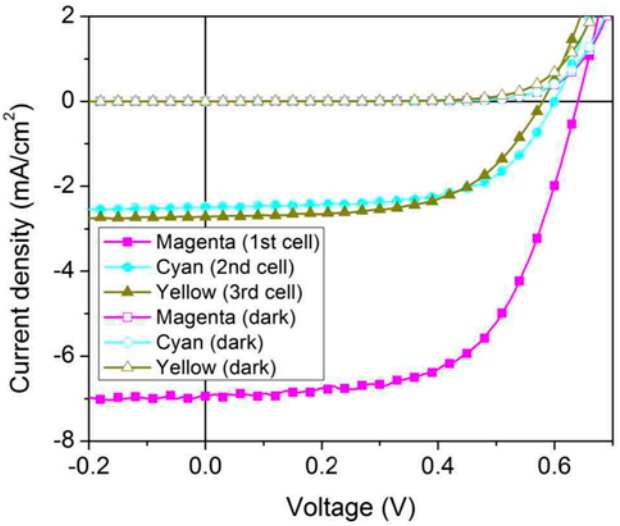


Figure 4.25. The realization of photon recycling with the spectrum splitting of the cascaded light absorption: Current density-voltage (J-V) performances of the three cells are also measured in the cascaded platform, depicting photon recycling for electric current in consecutive cells.

## 4.4 Towards a Few Nanometer a-Si PV

A single nanometer-thick a-Si hybrid cell performs as a diode responding to AM 1.5 simulated light compared to dark condition (Figure 4.26). Albeit its reverse current in dark shows less rectifying property, the device provides the short circuit current density ($J_{sc}$) and open circuit voltage ($V_{oc}$) under light illumination, obviously manifesting that the single nanometer cell works as phovoltaics. We compared the performance of a 4 nm-thick hybrid cell in the same figure, which explains a few nanometer thicker a-Si photoactive layer helps the device give better photovoltaic characteristics. External

quantum efficiency (EQE) of the devices was also explored along with the numerically calculated a-Si absorption (Figure 4.27).

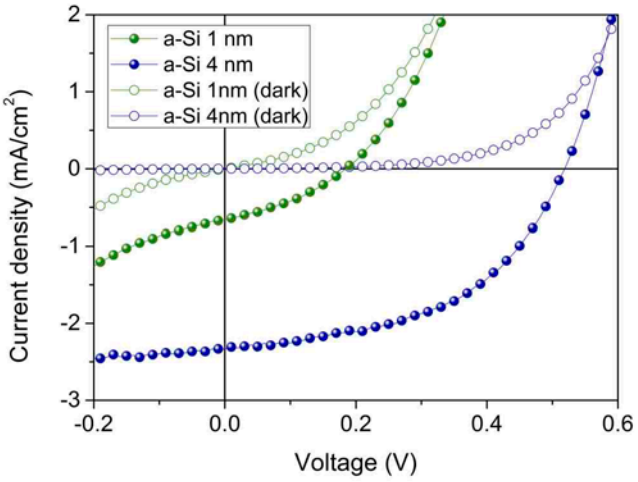


Figure 4.26. A single nanometer-thick amorphous silicon (a-Si) solar cells with inorganic/organic hybrid charge transport layers: Current density-voltage (J-V) characteristics of a few nanometer-thick a-Si hybrid cells under AM 1.5 simulated light (solid circle) and dark conditions (open circle). The thicknesses of a-Si are 1 nm and 4 nm with thick silver (Ag) cathode.

The EQE spectrum of 4 nm-thick cell (Figure 4.27) fits very well with the a-Si absorption profile calculation proving that the extremely thin a-Si photoactive layer prevents any possible charge recombination processes. This also implies that all the photogenerated charges are extracted without recombination, which allows the ultra-thin PV devices perform in a designed manner. However, for a single nanometer-thick hybrid cell, we note that there is a slight discrepancy between EQE and a-Si absorption, especially at shorter wavelength region. We believe that this is because the comparable thickness of a-Si to its surface roughness causes device pinholes as well as light

scattering, which will be verified by device transmission and surface morphology measurements later in this chapter.

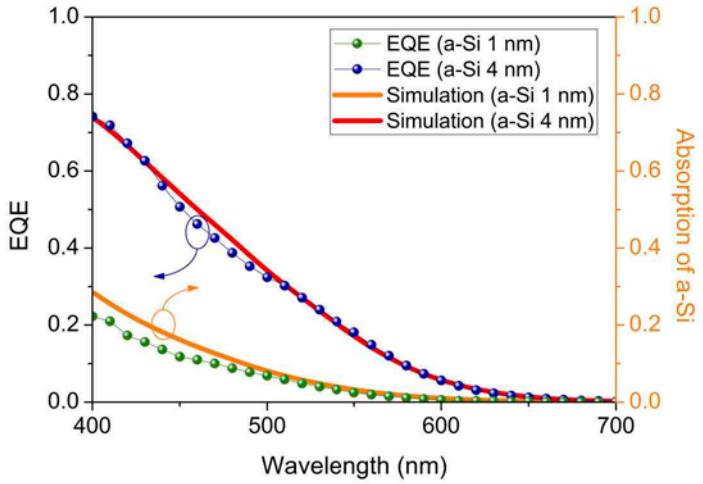


Figure 4.27. A single nanometer-thick amorphous silicon (a-Si) solar cells with inorganic/organic hybrid charge transport layers: Calculated a-Si absorption (colored solid lines) and measured external quantum efficiency (EQE) (colored solid circles) of 1 and 4 nanometer-thick a-Si hybrid cells with thick Ag cathode.

The few nanometer-thick a-Si hybrid cells are fabricated on indium-tin oxide (ITO) substrates (Figure 4.28). The structures have vanadium(V) oxide ($V_2O_5$) for holes transport and indene-$C_{60}$ bisadduct (ICBA) for electrons as in Chapter 4.1 and 4.2, which are around 5 nm-thick for each. Followed by ICBA, another 5 nm organic material of bis-adduct fullerene surfactant ($C_{60}$ surfactant) is used to reduce the work function of silver (Ag) electrode, offering ohmic contact between Ag and the electron transport layer. The two different thicknesses of a-Si photoactive layers, 1 and 4 nanometers, are used for photovoltaic device study.

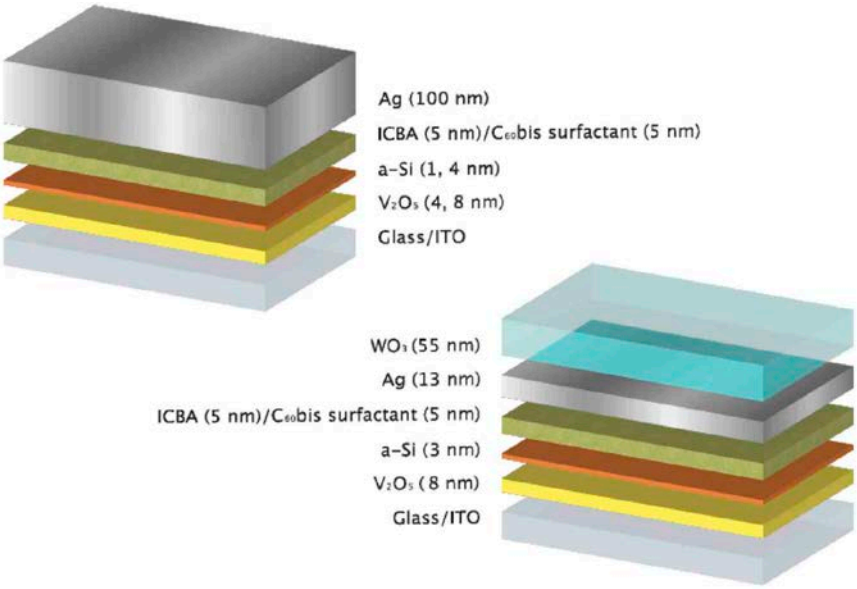


Figure 4.28. A single nanometer-thick amorphous silicon (a-Si) solar cells with inorganic/organic hybrid charge transport layers: A device structure of proposed a few nanometer-thick hybrid cells. A cathode comprises thick Ag or Ag (13 nm)-tungsten trioxide ($WO_3$) (55 nm) with organic electron transport layers, and indium-tin oxide (ITO) with vanadium(V) oxide ($V_2O_5$) (8 nm) hole transport layer for an anode. Between the two electrodes, a few nanometer a-Si is located.

In addition, as a demonstration, we built a transparent a-Si (3 nm) inorganic/organic hybrid cells by properly designing Ag-tungsten trioxide ($WO_3$) cathode (Figure 4.28) as illustrated in the device picture taken on campus (Figure 4.29). Additionally, we calculate the color coordinate (x,y) under AM 1.5 illumination, which is depicted in the CIE 1931 chromaticity diagram to estimate the transparency perception of the 3 nm a-Si hybrid cell as shown in Figure 4.29. The calculated color coordinate is (0.358, 0.360), demonstrating good transparency that is close to the coordinate representation of the white light (0.33, 0.33).

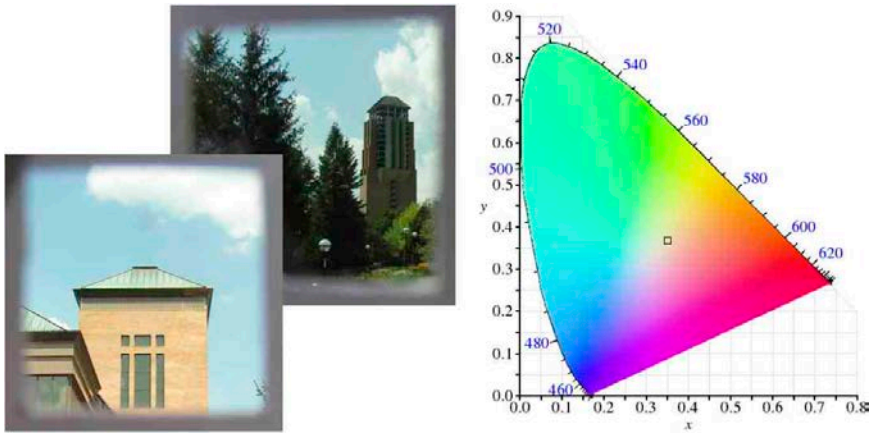


Figure 4.29. A single nanometer-thick amorphous silicon (a-Si) solar cells with inorganic/organic hybrid charge transport layers: Image of the fabricated a-Si (3 nm) hybrid cells with Ag-$WO_3$ cathode shows obvious transparency (70 % average) enough to see a tower and a fountain through on campus. The CIE 1931 chromaticity diagram estimates transparency by giving the color coordinate at (0.358, 0.360), close to white light coordinate (0.33, 0.33).

Benefited by a few nanometer-thick a-Si hybrid cells, we can design fairly transparent solar cell structures by incorporating metal-dielectric transparent cathode instead of conventional thick metal film (Figure 4.30). The 3 nm of a-Si was utilized for a photoactive layer along with the cathode of silver (Ag) and tungsten trioxide ($WO_3$), 13 nm and 55 nm, respectively.

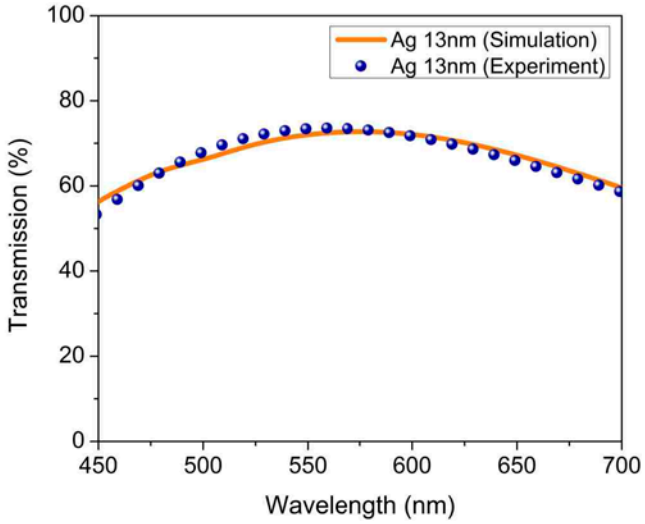


Figure 4.30. A few nanometer-thick a-Si hybrid cells for transparent electric power generators: Measured transmission (dotted line) fits well with the calculated transmission of the hybrid cells, showing around 70 % average transmission.

The optical transmission featuring a flat and broad spectrum obtained by the numerical simulation is well matched with the experimentally measured profile as described in Figure 4.30. Such a flat and broad transmission characteristics is primarily due to a resonance formed in a cavity consisting of a highly absorptive material (a-Si) with an extremely thin cavity length as well as poor quality factor (Q-factor) arising from the weak reflection at the interfaces (i.e. $V_2O_5$/a-Si and thin Ag/$C_{60}$ surfactant).

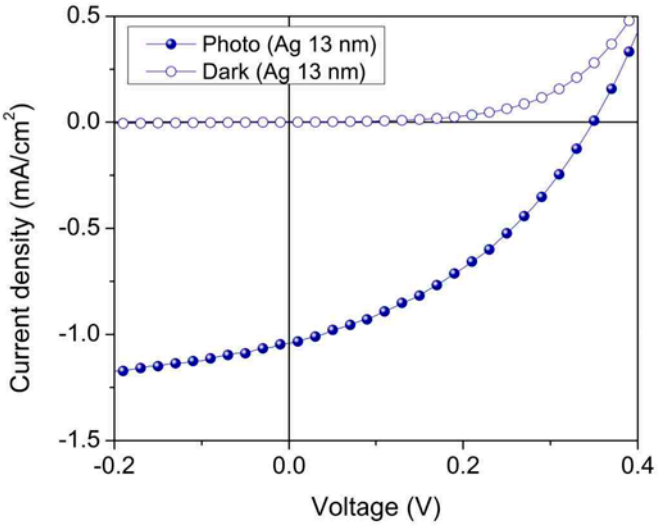


Figure 4.31. A few nanometer-thick a-Si hybrid cells for transparent electric power generators: Current density-voltage characteristics are studied for electric power generating performance under AM 1.5 illumination and dark condition.

Even with highly transparent property averaging around 70 % transmission, our hybrid cells generate electricity under AM 1.5 simulated light with the suppressed dark current as shown in Figure 4.31. The hybrid cells provide around 1.0 mA/cm$^2$ and 0.35 V, $J_{sc}$ and $V_{oc}$, respectively. The electric power-generating performance was verified further by comparing the simulated a-Si absorption spectrum to the measured EQE profile, which presents a great agreement (Figure 4.32). This good match provides explicit evidence, indicating that any type of our hybrid device structures with a few nanometer-thick a-Si shows almost negligible photogenerated charge recombination. As a result of the absence of charge recombination, we can eventually eliminate the light-induced degradation issue that conventional a-Si solar cells have struggled for many years [12], [27], [28]. We believe our transparent hybrid solar cell technology has the potential for

various applications such as clear windows or modern architectural building components that supply electric power as well.

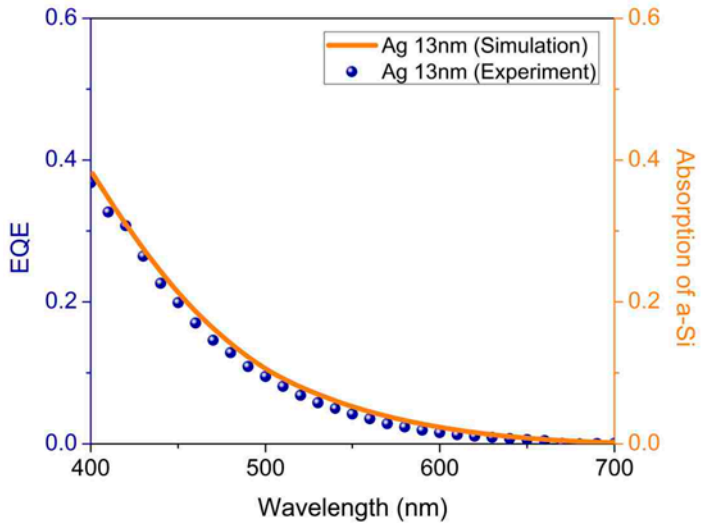


Figure 4.32. A few nanometer-thick a-Si hybrid cells for transparent electric power generators: Measured external quantum efficiency (EQE) spectrum (dotted line) shows a good match with the simulated absorption curve (solid line) in 3 nm-thick a-Si photoactive layer, supporting negligible photogenerated charge recombination in devices.

Since we utilize $V_2O_5$ hole transporting property instead of p-doped layer, we investigate further on device performances according to various anode conditions. As depicted in Figure 4.33-4.44, two different $V_2O_5$ thicknesses (4 and 8 nm), with or without 300 °C 10-minute thermal annealing process, detailed discussion in Chapter 2.2, are explored for current density-voltage (J-V) characteristics. All the devices are prepared as thermally evaporated $V_2O_5$ on ITO substrates, some of which are later annealed in a rapid thermal annealing equipment. In case of 4 nm $V_2O_5$, the annealing process affects J-V performance in terms of $V_{oc}$ and $J_{sc}$, which is observed clearer in 4 nm a-Si devices. The J-V performances of a single nanometer a-Si cells with 4 nm $V_2O_5$ (annealed/non-

annealed) are shown in Figure 4.33. Furthermore, the insets of Figure 4.33 shows J-V curves in wider voltage range, depicting a single nanometer-thick hybrid cells work as diodes regardless of the $V_2O_5$ variations.

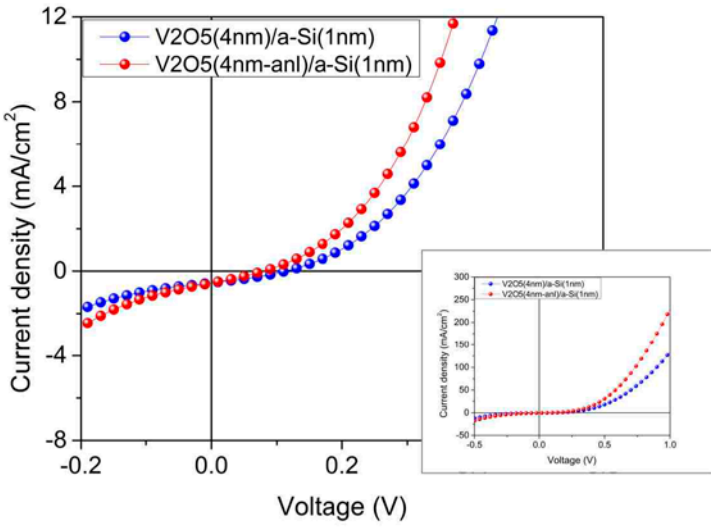


Figure 4.33. Current density-voltage (J-V) characteristics of a few nanometer-thick hybrid cells with different properties of the hole transport layer: A single nanometer-thick a-Si photoactive layer incorporates with two different conditions (non-anneal and thermal annealing at 300 °C) of $V_2O_5$ (4 nm) in order to allow the hybrid cells to perform as light-responding diodes under AM 1.5 simulated light (inset: J-V curves under wider voltage bias range).

The current density-voltage characteristic of a single nanometer a-Si hybrid cell (Figure 4.33) is supported by experimentally measured EQE spectra (Figure 4.34). The measured EQE curves are compared to the numerically calculated a-Si absorption spectra, which allow us to study how efficiently photogenerated charges are extracted.

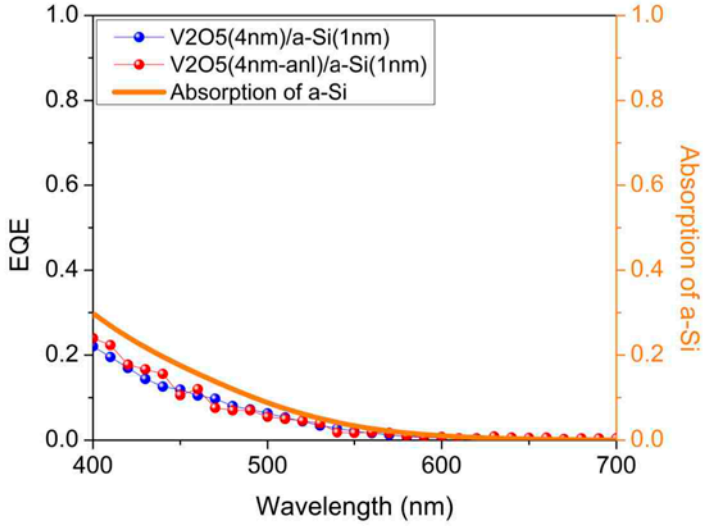


Figure 4.34. External quantum efficiency (EQE) characterizations of fabricated few nanometer-thick a-Si hybrid devices: A single nanometer-thick a-Si photoactive layer incorporates with two different conditions (non-anneal and thermal annealing at 300 °C) of $V_2O_5$ (4 nm). The experimentally measured EQE spectra (dotted lines) show a good agreement with the numerically calculated a-Si absorption curves (solid lines).

In order to verify the thickness of a-Si layer, we performed normal incidence transmission measurements for 1 nm of a-Si film deposited on 4 nm of $V_2O_5$ layer, which is built on top of the fused silica substrate. The measured (blue sphere) and corresponding simulated (red solid lines) transmission spectra of each case are shown in Figure 4.35. The experimental data show great agreement with the simulation results. The small difference between simulations and measurements, particularly at the shorter wavelength regime, is attributed to the roughness of 1 nm a-Si surface, thus inducing small scattering loss. This comparable surface roughness to the thickness of a-Si (1 nm) layer will be revisited later in this chapter by providing atomic force microscopy (AFM) characteristics.

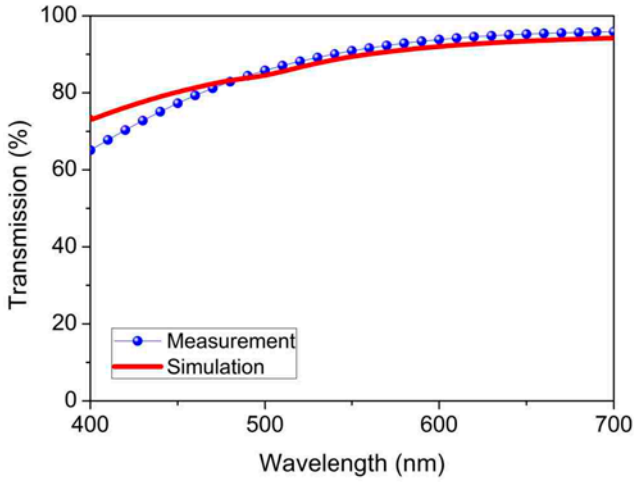


Figure 4.35. Numerically simulated and experimentally measured transmission of a few nanometer a-Si on top of $V_2O_5$: Experimentally measured transmission (dotted line) of a single nanometer a-Si on the hole transport layer $V_2O_5$ (4 nm) verifies a-Si thickness indirectly by compared with numerically calculated transmission (solid line).

With the same $V_2O_5$ layer property, 4 nm of a-Si films used for PV operation in Figure 4.36. We assume that the thermal annealing process changed $V_2O_5$ property mainly on the surface by nitrogen/oxygen gases but if $V_2O_5$ is too thin as 4 nm, whole layer property varies causing a big $V_{oc}$ change (Figure 4.36). As $V_2O_5$ thermal annealing is known to reduce its bandgap [29], inducing phase transition, we observe that $V_2O_5$ energy band levels play a major role in determining the $V_{oc}$ of the few nanometer-thick a-Si hybrid cells.

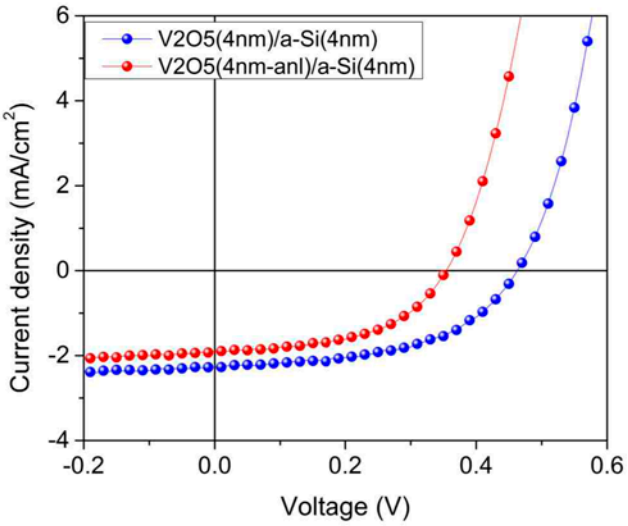


Figure 4.36. Current density-voltage (J-V) characteristics of a few nanometer-thick hybrid cells with different properties of the hole transport layer: The photoactive layer of a-Si (4 nm) is used for further verification of better photovoltaic performance in terms of short circuit current density ($J_{sc}$) and open circuit voltage ($V_{oc}$) with two different conditions (non-anneal and thermal annealing at 300 °C) of $V_2O_5$ (4 nm).

Since photogenerated electron charges are not effectively blocked by the thin $V_2O_5$ (4 nm) to the anode, charge recombination loss is observed in Figure 4.37, compared to the thicker $V_2O_5$ (8 nm), which will be introduced later.

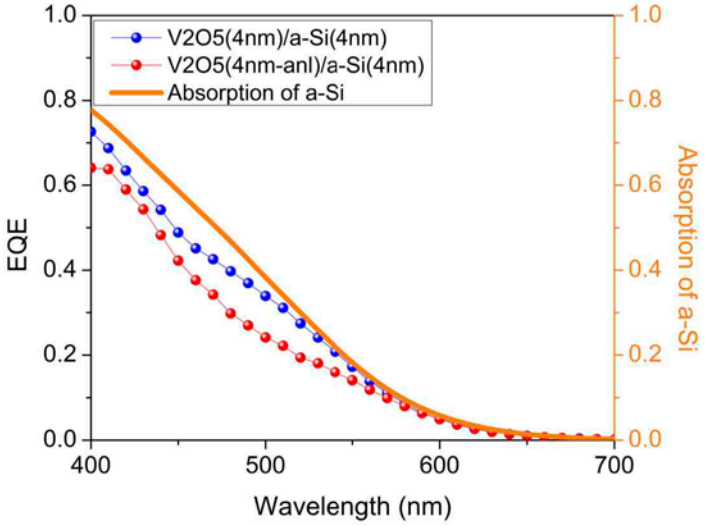


Figure 4.37. External quantum efficiency (EQE) characterizations of fabricated few nanometer-thick a-Si hybrid devices: A 4 nm a-Si photoactive layer incorporates with two different conditions (non-anneal and thermal annealing at 300 °C) of $V_2O_5$ (4 nm). The experimentally measured EQE spectra (dotted lines) show a good agreement with the numerically calculated a-Si absorption curves (solid lines).

In Figure 4.38, the 4 nm a-Si on the hole transport layer $V_2O_5$ (4 nm) verifies a-Si thickness indirectly by compared with numerically calculated transmission (solid line).

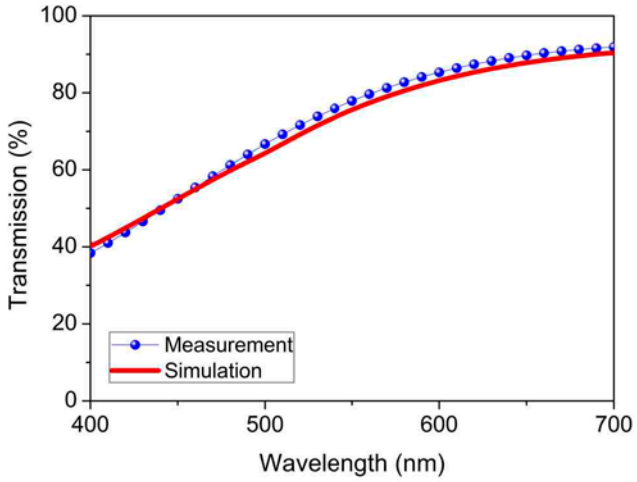


Figure 4.38. Numerically simulated and experimentally measured transmission of a few nanometer a-Si on top of $V_2O_5$: Experimentally measured transmission (dotted line) of a 4 nm a-Si on the hole transport layer $V_2O_5$ (4 nm) verifies a-Si thickness indirectly by compared with numerically calculated transmission (solid line).

Moreover, we discovered that the thickness of $V_2O_5$ is also important for higher $V_{oc}$ of the cells since the thicker $V_2O_5$ (8 nm) prevents photogenerated electron charges in the a-Si active layer from being lost to the anode (Figure 4.39), compared to the ones with $V_2O_5$ (4 nm) in Figure 4.33. Even if the annealing of $V_2O_5$ still changes the device performance in 8 nm $V_2O_5$, the variation is comparably smaller than the 4 nm $V_2O_5$ devices.

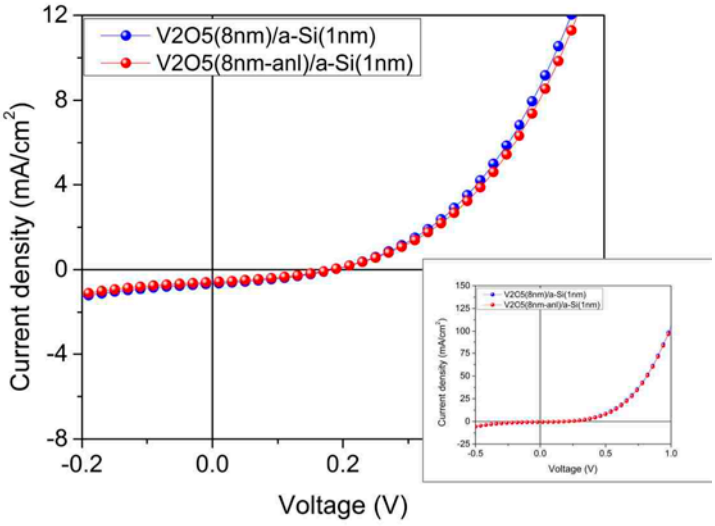


Figure 4.39. Current density-voltage (J-V) characteristics of a few nanometer-thick hybrid cells with different properties of the hole transport layer: A single nanometer-thick a-Si photoactive layer incorporates with two different conditions (non-anneal and thermal annealing at 300 °C) of $V_2O_5$ (8 nm) in order to allow the hybrid cells to perform as light-responding diodes under AM 1.5 simulated light (inset: J-V curves under wider voltage bias range).

In Figure 4.40 compared with 4.34, we note that a-Si (1 nm) hybrid cells, regardless of $V_2O_5$ conditions, show deviations between EQE and a-Si absorption. We attribute this to the comparable $V_2O_5$ surface roughness to the a-Si photoactive layer thickness, therefore inducing the parasitic pinholes in the devices. Later AFM images will show the $V_2O_5$ surface roughness.

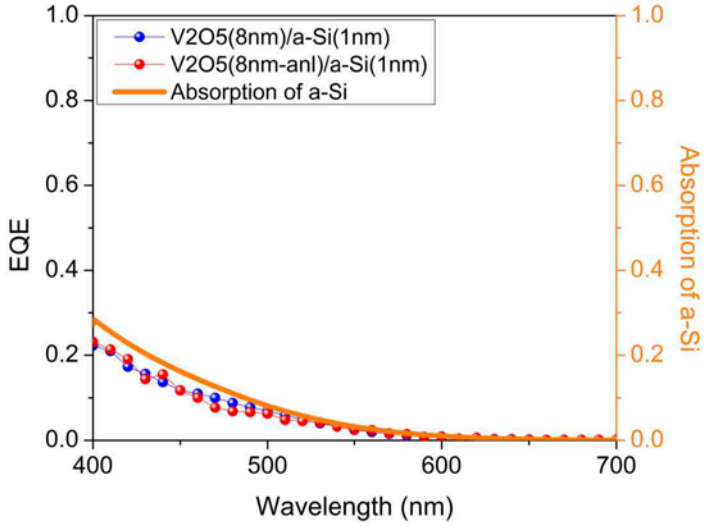


Figure 4.40. External quantum efficiency (EQE) characterizations of fabricated few nanometer-thick a-Si hybrid devices: A single nanometer-thick a-Si photoactive layer incorporates with two different conditions (non-anneal and thermal annealing at 300 °C) of $V_2O_5$ (8 nm). The experimentally measured EQE spectra (dotted lines) show a good agreement with the numerically calculated a-Si absorption curves (solid lines).

The transmission discrepancy for 1 nm of a-Si film deposited on 8 nm of $V_2O_5$ layer is also observed in Figure 4.41 similarly to Figure 4.35, which is due to the comparable surface roughness to the thickness of a-Si (1 nm). It is noted that the simulated transmission spectra in this study are obtained by using the transfer matrix method and the calculation is carried out based on the refractive indices of a-Si and $V_2O_5$ measured by an ellipsometer [1].

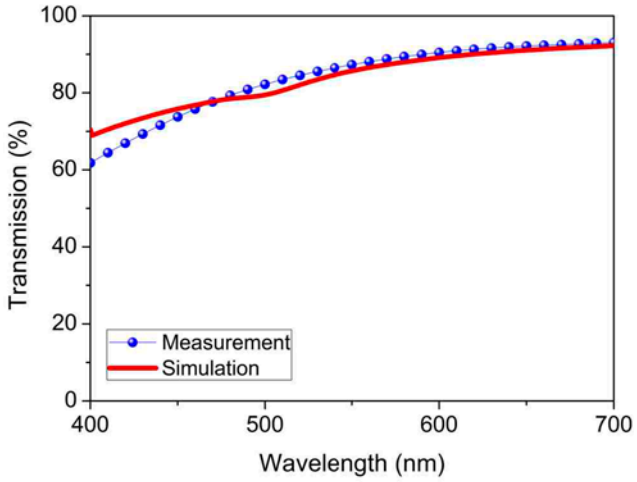


Figure 4.41. Numerically simulated and experimentally measured transmission of a few nanometer a-Si on top of $V_2O_5$: Experimentally measured transmission (dotted line) of a single nanometer a-Si on the hole transport layer $V_2O_5$ (8 nm) verifies a-Si thickness indirectly by compared with numerically calculated transmission (solid line).

In Figure 4.42, the a-Si (4 nm) devices with the thicker $V_2O_5$ (8 nm) compared to the ones with thinner $V_2O_5$ (4 nm) (Figure 4.36) show better PV performances and more stable $V_{oc}$ values regardless of annealing, which is ascribed to better Schottky contact between a-Si and $V_2O_5$.

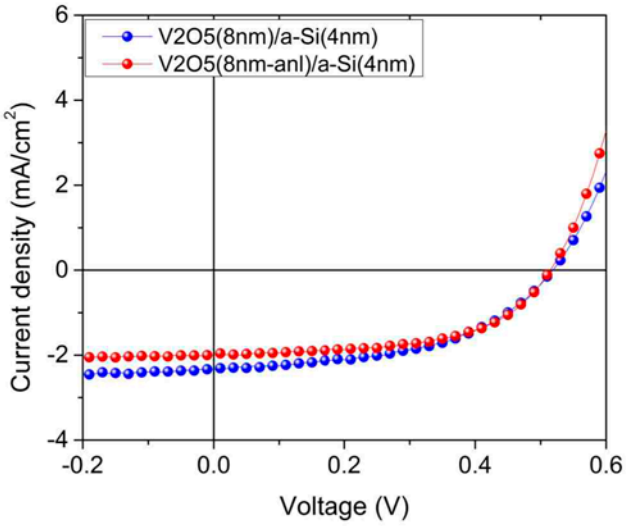


Figure 4.42. Current density-voltage (J-V) characteristics of a few nanometer-thick hybrid cells with different properties of the hole transport layer: The photoactive layer of a-Si (4 nm) is used for further verification of better photovoltaic performance in terms of short circuit current density ($J_{sc}$) and open circuit voltage ($V_{oc}$) with two different conditions (non-anneal and thermal annealing at 300 °C) of $V_2O_5$ (8 nm).

The a-Si (4 nm) absorption and EQE difference is less significant with $V_2O_5$ (8 nm) in Figure 4.43 since $V_2O_5$ (8 nm) is anticipated to work better as an electron block and hole transport layer than $V_2O_5$ (4 nm) (Figure 4.37). Also, with $V_2O_5$ (8 nm without annealing), the measured EQE of the a-Si (4 nm) hybrid cell fits pretty well with a-Si absorption calculation due to the suppressed charge recombination benefited by a very thin nanometer-thick photoactive layer (Figure 4.43). Overall, thermally annealed $V_2O_5$ for extremely thin a-Si is less efficient in extracting photogenerated charges since the EQE spectra reveal larger discrepancy with the numerically simulated a-Si absorption.

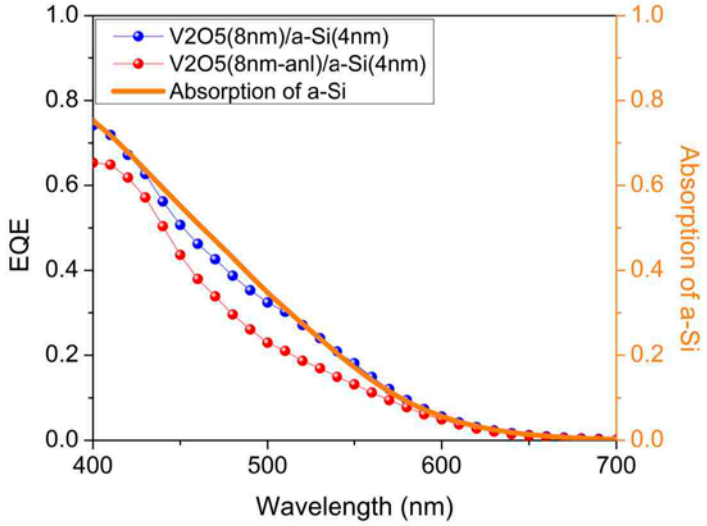


Figure 4.43. External quantum efficiency (EQE) characterizations of fabricated few nanometer-thick a-Si hybrid devices: A 4 nm a-Si photoactive layer incorporates with two different conditions (non-anneal and thermal annealing at 300 °C) of $V_2O_5$ (8 nm). The experimentally measured EQE spectra (dotted lines) show a good agreement with the numerically calculated a-Si absorption curves (solid lines).

Again, In Figure 4.44, the 4 nm a-Si on the hole transport layer $V_2O_5$ (8 nm) verifies a-Si thickness indirectly by compared with numerically calculated transmission (solid line), which shows very good fit as on $V_2O_5$ (4 nm) in Figure 4.38.

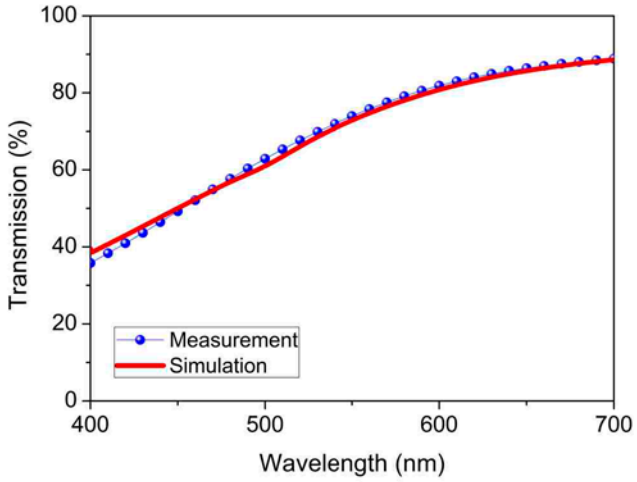


Figure 4.44. Numerically simulated and experimentally measured transmission of a few nanometer a-Si on top of $V_2O_5$: Experimentally measured transmission (dotted line) of a 4 nm a-Si on the hole transport layer $V_2O_5$ (8 nm) verifies a-Si thickness indirectly by compared with numerically calculated transmission (solid line).

We analyzed the surface roughness of $V_2O_5$ on crystalline silicon substrates; and compared it with the morphology of a few nanometer a-Si (1 and 4 nm) deposited on $V_2O_5$ by employing atomic force microscopy (AFM). Three-dimensional surface morphology figures by AFM are depicted in Figure 4.45a-d, incorporating the inset information of Gaussian surface profile distribution for each.

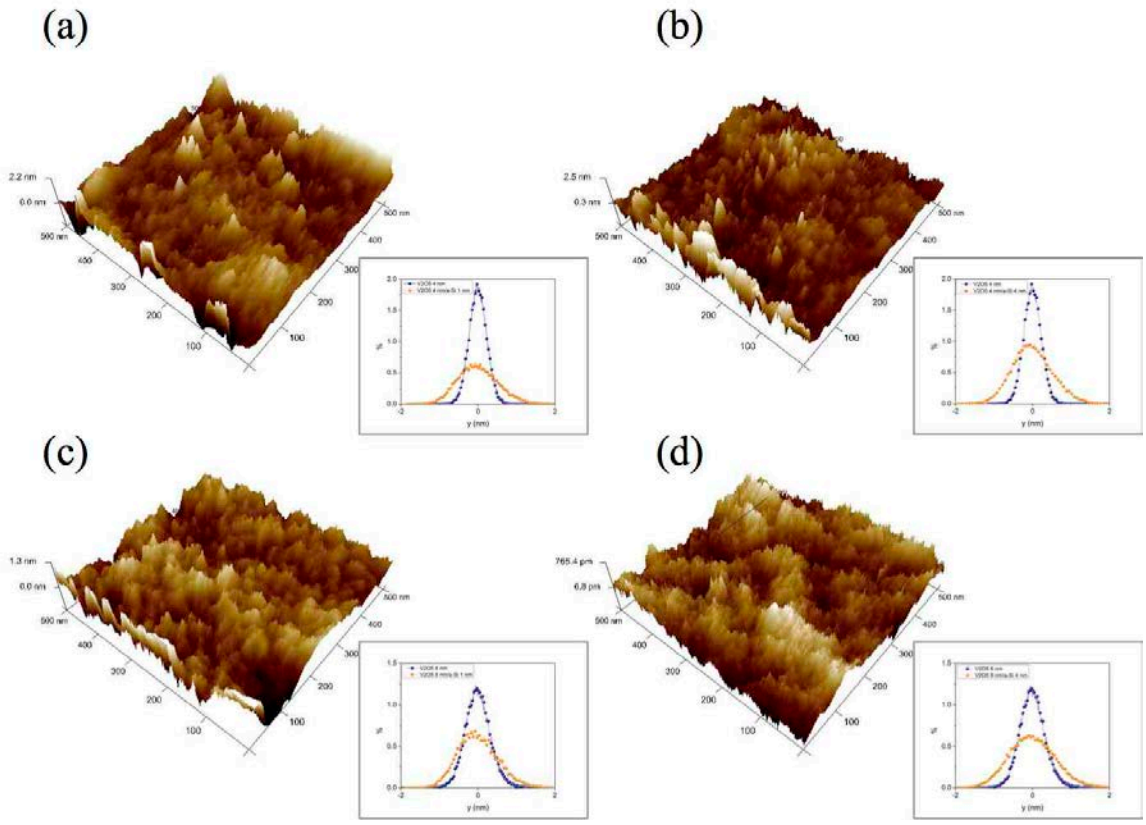


Figure 4.45. Surface roughness characterization of a few nanometer a-Si on top of $V_2O_5$ by atomic force microscopy (AFM): (a) Experimentally measured three-dimensional surface morphology by AFM show the surface roughness of a single nanometer a-Si on the hole transport layer $V_2O_5$ (4 nm) (inset: root-mean-square (rms) roughness Gaussian distribution profile showing blue dots in $V_2O_5$ roughness profile, and orange dots for a-Si on $V_2O_5$). (b) The surface morphology of a-Si (4 nm) instead on the same thickness of $V_2O_5$ as in (a). (c)-(d) The surface roughness of a few nanometer a-Si (1 and 4 nm) on 8 nm $V_2O_5$ was characterized in the same manner of (a)-(b).

The $V_2O_5$ 4 nm and 8 nm layers on silicon substrates show the root-mean-square (rms) roughness of 0.28 nm and 0.44 nm, respectively. Once the a-Si is deposited on top of the $V_2O_5$ layers, the roughness becomes a little bigger as described with red curves in the inset figures, showing the similar rms roughness ranging from 0.58 nm to 0.68 nm. As we anticipated in the previous experimental results, the surface roughness is a lot comparable to 1 nm a-Si, which can cause charge leakage directly via pinholes between

anode and cathode. We conclude that, within a few nanometer a-Si thickness ranges, the surface roughness of hole transport and photoactive layers determines the diode characteristics of the nanometer-thick hybrid cells as analyzed in various ways above.

## 4.5 Conclusion

To summarize, we have demonstrated that ultra-thin amorphous silicon (a-Si) hybrid cells with varied undoped a-Si layer thickness can pass blue, green, and red colors. Simultaneous power generation is achieved with efficiency approaching 2 %. The use of ultra-thin a-Si layer leads to high angular tolerance of the transmitted colors. Notably, most of the absorbed photons in the undoped a-Si layer were converted to the electric charges benefited by the suppressed electron-hole recombination in the ultra-thin a-Si layer. We have also showed dual-function a-Si hybrid photovoltaic (PV) devices that can create angle-insensitive (up to 60°) reflected colors with high color purity. The ultra-thin a-Si reflective colored cells can generate electricity with a power conversion efficiency of up to 3 %. As in the transmissive colored devices, most photons absorbed in the ultra-thin undoped a-Si film can contribute to the collected photocurrent, which can significantly mitigate the light-induced degradation of a-Si solar cells as well. Furthermore, a cascaded arrangement scheme exploiting these angle-invariant color resonances enables the efficient harvesting of a wide range of incident light energy. Lastly, we have experimentally revealed a single nanometer-thick a-Si solar cell that was previously unachievable with conventional a-Si PV structure, incorporating doped layers. We have

obtained 1.0 mA/cm$^2$ of short circuit current density and 0.35 V of open circuit voltage by 3 nm-thick a-Si hybrid device, simultaneously creating 70 % of average transmittance throughout the entire visible band. We believe that this novel ultra-thin hybrid PV principle can be easily employed in different inorganic materials systems as well.

# References


[1] J. Y. Lee, K.-T. Lee, S. Seo, and L. J. Guo, "Decorative power generating panels creating angle insensitive transmissive colors," *Sci. Rep.*, vol. 4, Feb. 2014.

[2] X. Guo, J. Lin, H. Chen, X. Zhang, Y. Fan, J. Luo, and X. Liu, "Ultrathin and efficient flexible polymer photovoltaic cells based on stable indium-free multilayer transparent electrodes," *J. Mater. Chem.*, vol. 22, no. 33, pp. 17176–17182, 2012.

[3] H. Jin, C. Tao, M. Velusamy, M. Aljada, Y. Zhang, M. Hambsch, P. L. Burn, and P. Meredith, "Efficient, Large Area ITO-and-PEDOT-free Organic Solar Cell Sub-modules," *Adv. Mater.*, vol. 24, no. 19, pp. 2572–2577, Apr. 2012.

[4] J. Meyer, K. Zilberberg, T. Riedl, and A. Kahn, "Electronic structure of Vanadium pentoxide: An efficient hole injector for organic electronic materials," *J. Appl. Phys.*, vol. 110, no. 3, p. 033710, 2011.

[5] B. E. Lassiter, G. Wei, S. Wang, J. D. Zimmerman, V. V. Diev, M. E. Thompson, and S. R. Forrest, "Organic photovoltaics incorporating electron conducting exciton blocking layers," *Appl. Phys. Lett.*, vol. 98, no. 24, p. 243307, 2011.

[6] Logeeswaran VJ, N. P. Kobayashi, M. S. Islam, W. Wu, P. Chaturvedi, N. X. Fang, S. Y. Wang, and R. S. Williams, "Ultrasmooth Silver Thin Films Deposited with a Germanium Nucleation Layer," *Nano Lett.*, vol. 9, no. 1, pp. 178–182, Jan. 2009.

[7] Y. He, H.-Y. Chen, J. Hou, and Y. Li, "Indene−C 60Bisadduct: A New Acceptor

for High-Performance Polymer Solar Cells," *J. Am. Chem. Soc.*, vol. 132, no. 4, pp. 1377–1382, Feb. 2010.

[8] K. M. O'Malley, C.-Z. Li, H.-L. Yip, and A. K.-Y. Jen, "Enhanced Open-Circuit Voltage in High Performance Polymer/Fullerene Bulk-Heterojunction Solar Cells by Cathode Modification with a C60 surfactant," *Adv. Energy Mater.*, vol. 2, pp. 82–86, 2012.

[9] M. Goerlitzer, N. Beck, P. Torres, J. Meier, N. Wyrsch, and A. Shah, "Ambipolar diffusion length and photoconductivity measurements on '"midgap"' hydrogenated microcrystalline silicon," *J. Appl. Phys.*, vol. 80, no. 9, p. 5111, 1996.

[10] E. A. Schiff, "Low-mobility solar cells: a device physics primer with application to amorphous silicon," *Solar Energy Materials and Solar Cells*, vol. 78, no. 1, pp. 567–595, Jul. 2003.

[11] X. Deng and E. A. Schiff, "Amorphous Silicon–based Solar Cells," *Handbook of Photovoltaic Science and Engineering (Edited by A. Luque and S. Hegedus)*, pp. 505–565, Mar. 2003.

[12] D. L. Staebler and C. R. Wronski, "Reversible conductivity changes in discharge-produced amorphous Si," *Appl. Phys. Lett.*, vol. 31, no. 4, p. 292, 1977.

[13] H. M. Branz, "Hydrogen collision model: Quantitative description of metastability in amorphous silicon," *Phys. Rev. B*, vol. 59, no. 8, pp. 5498–5512, 1999.

[14] M. G. Deceglie, V. E. Ferry, A. P. Alivisatos, and H. A. Atwater, "Design of Nanostructured Solar Cells Using Coupled Optical and Electrical Modeling," *Nano Lett.*, vol. 12, no. 6, pp. 2894–2900, Jun. 2012.

[15] D. E. Carlson and C. R. Wronski, "Amorphous silicon solar cell," *Appl. Phys. Lett.*, vol. 28, no. 11, p. 671, 1976.

[16] A. V. Shah, H. Schade, M. Vanecek, J. Meier, E. Vallat-Sauvain, N. Wyrsch, U. Kroll, C. Droz, and J. Bailat, "Thin-film silicon solar cell technology," *Prog. Photovolt: Res. Appl.*, vol. 12, pp. 113–142, 2004.

[17] S. Benagli, D. Borrello, E. Vallat-Sauvain, J. Meier, U. Kroll, J. Hoetzel, J.

Bailat, J. Steinhauser, M. Marmelo, G. Monteduro, and L. Castens, "High-efficiency amorphous silicon devices on LPCVD-ZnO TCO prepared in industrial KAI$^{TM}$-M R&D reactor," *24$^{th}$ European PVSC*, 3BO.9.3., Sept. 2009.

[18] K.-T. Lee, J. Y. Lee, S. Seo, and L. J. Guo, "Colored ultrathin hybrid photovoltaics with high quantum efficiency," *Light: Science & Applications*, vol. 3, p. e215, 2014.

[19] K.-T. Lee, S. Seo, J. Y. Lee, and L. J. Guo, "Strong Resonance Effect in a Lossy Medium-Based Optical Cavity for Angle Robust Spectrum Filters," *Adv. Mater.*, vol. 26, no. 36, pp. 6324–6328, Jul. 2014.

[20] K.-T. Lee, S. Seo, J. Y. Lee, and L. Jay Guo, "Ultrathin metal-semiconductor-metal resonator for angle invariant visible band transmission filters," *Appl. Phys. Lett.*, vol. 104, no. 23, p. 231112, Jun. 2014.

[21] M. A. Kats, R. Blanchard, P. Genevet, and F. Capasso, "Nanometre optical coatings based on strong interference effects in highly absorbing media," *Nature Materials*, vol. 11, no. 10, pp. 1–5, Oct. 2012.

[22] M. A. Kats, D. Sharma, J. Lin, P. Genevet, R. Blanchard, Z. Yang, M. M. Qazilbash, D. N. Basov, S. Ramanathan, and F. Capasso, "Ultra-thin perfect absorber employing a tunable phase change material," *Appl. Phys. Lett.*, vol. 101, no. 22, p. 221101, 2012.

[23] C. N. Eisler, E. D. Kosten, E. C. Warmann, and H. A. Atwater, "Polyhedral specular reflector design for ultra high spectrum splitting solar module efficiencies (>50%)," presented at the *SPIE Solar Energy + Technology*, 2013, vol. 8821, pp. 88210B–88210B–3.

[24] M. D. Escarra, S. Darbe, E. C. Warmann, and H. A. Atwater, "Spectrum-Splitting Photovoltaics: Holographic Spectrum Splitting in Eight-Junction, Ultra-high Efficiency Module," *39$^{th}$ IEEE PVSC,* pp. 1852–1855, 2013.

[25] M. Stefancich, A. Zayan, M. Chiesa, S. Rampino, D. Roncati, L. Kimerling, and J. Michel, "Single element spectral splitting solar concentrator for multiple cells CPV system," *Optics Express*, vol. 20, no. 8, pp. 9004-9018, Apr. 2012.

[26] B. Mitchell, G. Peharz, G. Siefer, M. Peters, T. Gandy, J. C. Goldschmidt, J. Benick, S. W. Glunz, A. W. Bett, and F. Dimroth, "Four-junction spectral beam-

splitting photovoltaic receiver with high optical efficiency," *Prog. Photovolt: Res. Appl.*, vol. 19, no. 1, pp. 61–72, Dec. 2010.

[27] D. E. Carlson, K. Rajan, and D. Bradley, "Irreversible light-induced degradation in amorphous silicon solar cells," *26th IEEE PVSC,* pp. 595–598, 1997.

[28] S. Guha, "On light-induced effect in amorphous hydrogenated silicon," *J. Appl. Phys.*, vol. 52, no. 2, p. 859, 1981.

[29] D. Liu, Y. Liu, B. B. Garcia, Q. Zhang, A. Pan, Y.-H. Jeong, and G. Cao, "V2O5 xerogel electrodes with much enhanced lithium-ion intercalation properties with N2 annealing," *J. Mater. Chem.*, vol. 19, no. 46, pp. 8789–8795, 2009.

# Chapter 5

# Pursuing High Power Efficiency by Undoped a-Si Hybrid Cells

## 5.1 Introduction

Alongside the effort to create the new functionality of a-Si hybrid photovoltaics (PVs), as introduced in Chapter 5, we have been working on enhancing the power conversion efficiency of proposed PV device by utilizing nanostructured substrate. The substrate has been optimized to give light scattering effect to the a-Si hybrid device. The light scattering turned out to be very efficient in the undoped a-Si active layer since the absorption enhancement occurs right at the nanostructure interface with intrinsic a-Si where conventionally doped a-Si has been located. Due to efficient photon to electric charge conversion in the undoped a-Si, we are able to harvest the most of absorbed photons for electric PV power efficiency.

## 5.2 Efficiency Enhancement by Nanoparticles Embedded Substrate

The a-Si/organic hybrid cells have been built on glass substrates followed by silica NPs solution casting with thermal annealing (200 °C for 15 minutes) afterwards as described in Figure 5.1. The average diameter of the silica NPs is ~135 nm, which are dissolved in water by the 30 wt% concentration. We have diluted the NPs concentration further by adding water with the two different volume ratios of 1:2 and 1:4; and compared their PV performances according to the NPs concentration. Indium-tin oxide (ITO) is sputtered about 180 nm on top of silica NPs for transparent anode. For hole transport, $V_2O_5$ (10 nm) is thermally evaporated [1], [2]. Plasma enhanced chemical vapor deposition (PECVD) tool is utilized to deposit undoped a-Si on $V_2O_5$ [3]. Finally, led by indene-$C_{60}$ bisadduct (ICBA) spin casting for efficient electron transport on a-Si [4], [5], the cathode is completed with $Alq_3$/LiF/Al configuration (Figure 5.1), which has been experimentally evaluated to be efficient low work function electrode in our previous report [6].

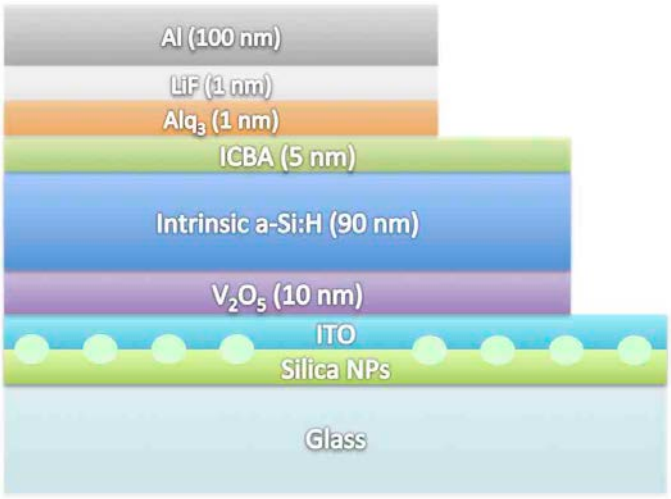


Figure 5.1. Device schematics of undoped a-Si (~90 nm) PVs with inorganic/organic hybrid charge transport layers based upon the silica NPs embedded ITO substrates.

Figure 5.2 shows the simplified energy band diagram of the proposed hybrid device structure as we introduced in Chapter 2.1.

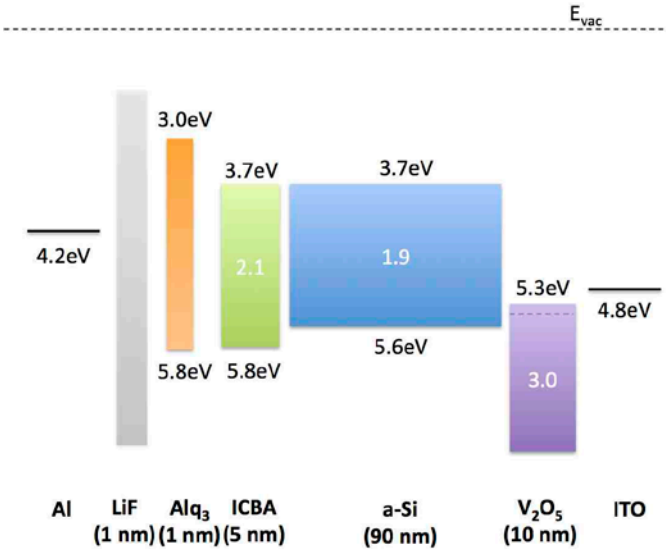


Figure 5.2. Simplified energy band diagram of the proposed a-Si hybrid device structure.

In order to characterize the NPs embedded a-Si hybrid devices, we perform the current density-voltage (J-V) measurement under AM1.5 illumination, whose set up is discussed in Chapter 2.2, and investigate the external quantum efficiency (EQE) characteristics. The schematic diagram of EQE characterization set up is described in Figure 5.3.

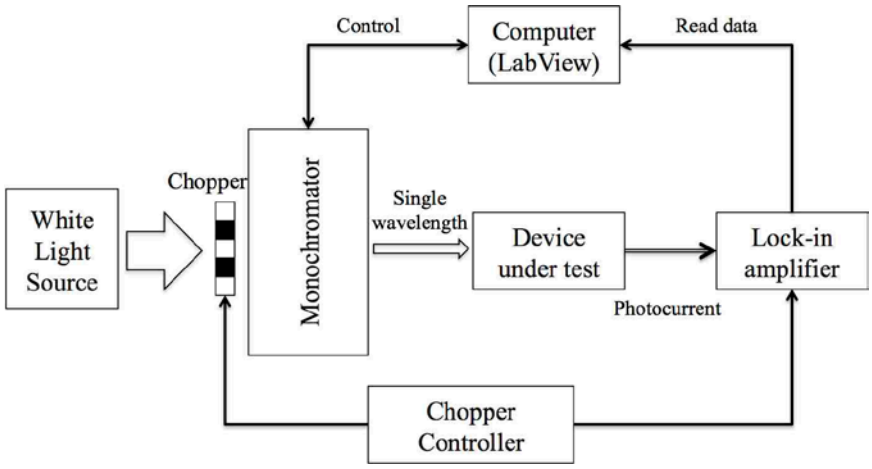


Figure 5.3. A schematic diagram of external quantum efficiency (EQE) characterization setup: A white light source, a chopper, a chopper controller, a monochromator, a lock-in amplifier to acquire photocurrent date with the suppressed noise helped by the chopper and the chopper controller, a computer equipped with LabView hardware/software, and a device on an optical stage.

In the EQE characterization set up, a white light is illuminated to a monochromator via a chopper in order to create a single wavelength visible light input to a device. Here a chopper controller operates the chopper synced with a lock-in amplifier, which suppress a signal noise greatly by filtering only the signal with reference frequency (chopper rotation frequency). The computer equipped with LabView hardware/software controls the monochromator in order to manage the single wavelength light sweep and collect photocurrent data from the lock-in amplifier. Lastly, the device is set up on a

properly implemented optical stage and probed with xyz-positioned manipulators for cathode and anode contacts. With the support from the characterization tools, the J-V and EQE performances of the NPs embedded a-Si hybrid devices are studied and shown in Figure 5.4 and 5.5.

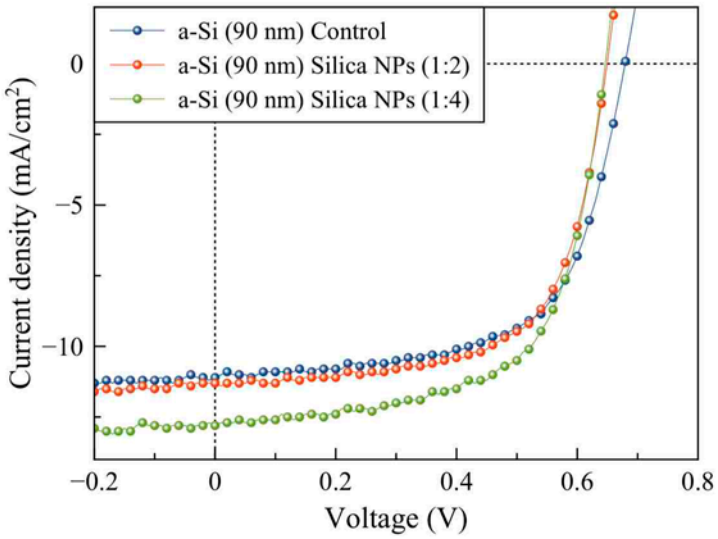


Figure 5.4. PV performance of a-Si hybrid cells with three different substrates (flat ITO/glass, 1:2 diluted NPs embedded, and 1:4 diluted NPs embedded substrates): J-V characteristics of the three different hybrid cells under AM1.5 illumination.

Three different device types are compared for electrical performance, which are composed of control device on flat ITO/glass substrate, 1:2 diluted NPs embedded cell, and 1:4 diluted one. According to J-V curve (Figure 5.4), we observe that short circuit current density ($J_{sc}$) of all the NPs embedded cell is larger than the control one. Especially, the 1:4 diluted hybrid cells improve $J_{sc}$ by around 15 %, which is confirmed by EQE data in Figure 5.5. According to EQE curves, we have noticed that the more concentrated NPs (1:2 diluted) induce EQE increase only in very short wavelength region

under 500 nm. However, in this wavelength range, since the number of photons is not a lot, $J_{sc}$ increase is not that noticeable.

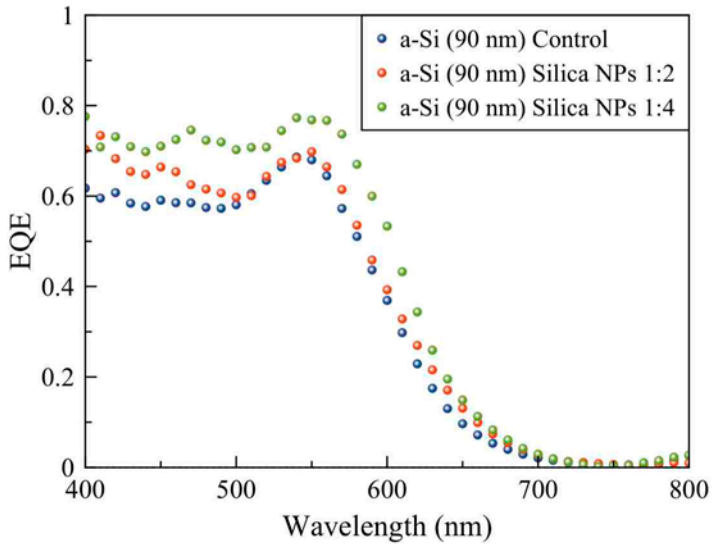


Figure 5.5. PV performance of a-Si hybrid cells with three different substrates (flat ITO/glass, 1:2 diluted NPs embedded, and 1:4 diluted NPs embedded substrates): EQE profiles of the hybrid cells showing that 1:4 diluted NPs embedded device outperforms in broad wavelength range over the flat substrate one.

On the other hand, the notable broad EQE increase by the 1:4 diluted NPs embedded hybrid cell has been empirically investigated (Figure 5.5), which explains ~15 % $J_{sc}$ increase compared to the control cell. In order to study the possible contribution of the light scattering effect of NPs embedded substrate for the power efficiency enhancement, we take a look at the scanning electron microscopy (SEM) image of silica NPs is depicted in Figure 5.6, which shows the diameter of the NPs ranges from ~100 nm to ~150 nm.

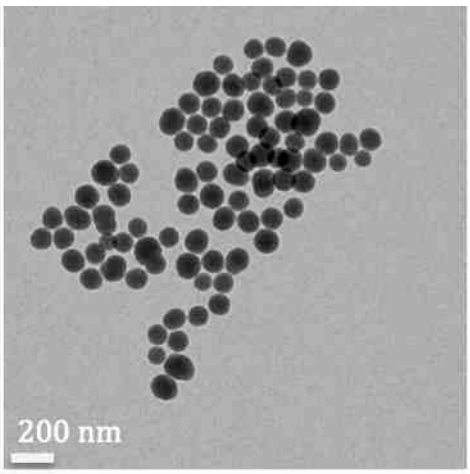


Figure 5.6. The SEM image of silica NPs provided by King Abdullah University of Science and Technology (KAUST) in Saudi Arabia.

In Figure 5.7, the surface morphology of flat ITO/glass substrate, measured in a small area of 2 μm by 2 μm by atomic force microscopy (AFM), is shown to be relatively smooth compared to the following a-Si hybrid PV device structure based on silica NPs embedded ITO substrate. ITO is deposited by sputtering for 180 nm target thickness.

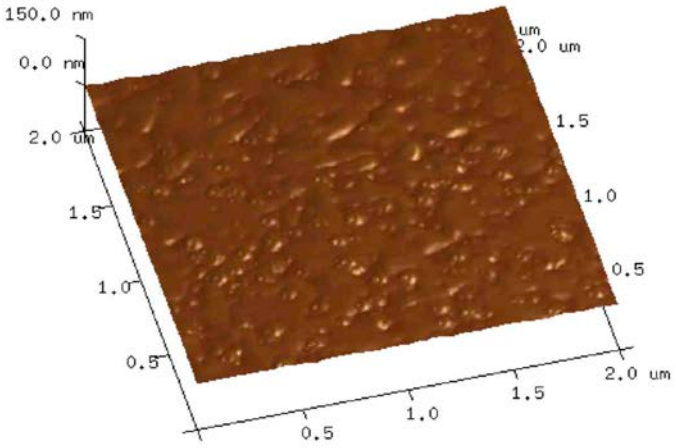


Figure 5.7. The surface morphology characteristic of flat ITO/glass substrate in 2 μm by 2 μm area, measured by atomic force microscopy (AFM).

Based upon the dilution of silica NPs water solution (20 wt%) with deionized water by the ratio of 1 to 4 by weight, we measured surface morphology of the diluted NPs embedded ITO substrate by AFM as shown in Figure 5.8. The diluted NPs solution is spin-casted for 30 seconds at 3000 rpm on top of fused silica substrate. The casted NPs are well distributed on the substrate and further annealed for 15 minutes at 200 °C on a hot plate. On top of the silica NPs, ITO gets deposited to form a NPs embedded substrate. A few NPs are shown in an area of 2 μm by 2 μm in Figure 5.8.

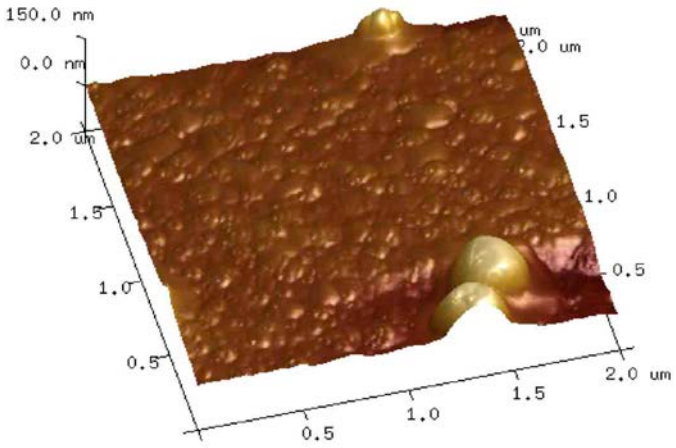


Figure 5.8. Surface morphology characteristics of silica NPs embedded ITO and a-Si hybrid cells before cathode deposition, measured in 2 μm by 2 μm by atomic force microscopy (AFM): Silica NPs are diluted with deionized water by 1:4 and get embedded in ITO layer on fused silica substrate, which clearly visualize ~135 nm diameter NPs.

In Figure 5.9, the surface morphology of a whole a-Si hybrid PV structure (Figure 5.1) without silica NPs before cathode deposition is depicted in a comparably large area of 10 μm by 10 μm, which is shown to be relatively smooth similar to Figure 5.7.

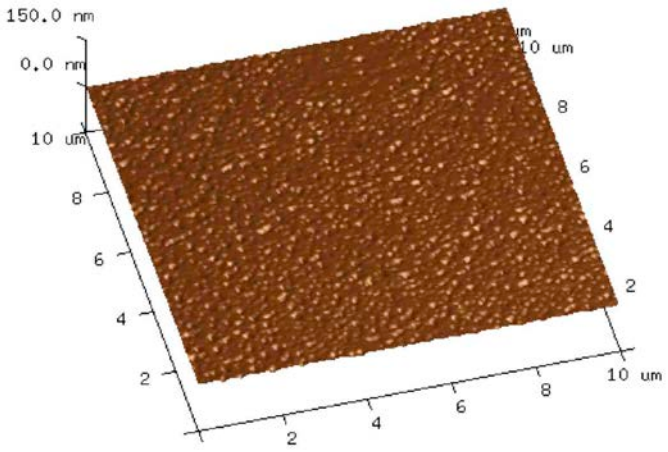


Figure 5.9. Surface morphology characteristic of whole device structure with flat ITO/glass substrate before Al cathode deposition in 10 μm by 10 μm area, measured by atomic force microscopy (AFM).

With the same dilution of silica NPs as Figure 5.8, we produce NPs embedded ITO substrate and finish a whole hybrid PV structure just before Al cathode deposition. In an area of 10 μm by 10 μm, the surface morphology of the hybrid structure is measured by AFM as shown in Figure 5.10. Due to the larger scanning area than the one in Figure 5.8, more NPs are observed in the target area. We anticipate that the embedded NPs induce light scattering effect in the a-Si hybrid PV device, thereby enhancing light absorption in undoped a-Si photoactive layer. The power conversion efficiency improvement by the NPs embedded ITO substrate has been demonstrated and discussed in Figure 5.4 and 5.5.

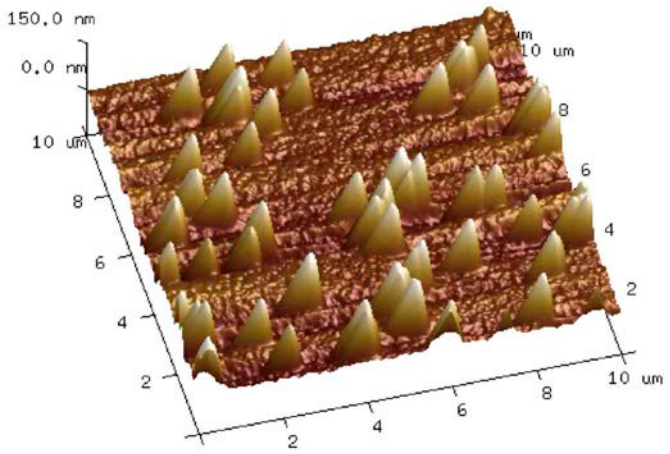


Figure 5.10. Surface morphology characteristics of silica NPs embedded ITO and a-Si hybrid cells before cathode deposition, measured by AFM in 10 μm by 10 μm: The surface of whole structure, Al cathode excluded, with 1:4 diluted NPs embedded ITO on fused silica substrate.

We have also explored that how efficiently the transmitted light through the NPs embedded ITO/glass substrate is converted to electrical PV efficiency compared to flat ITO/glass device as shown in Figure 5.11 and 5.12. With the flat ITO/glass substrate, we are able to find that there is a quite difference between the substrate transmittance and EQE from 400 nm to 550 nm (Figure 5.11).

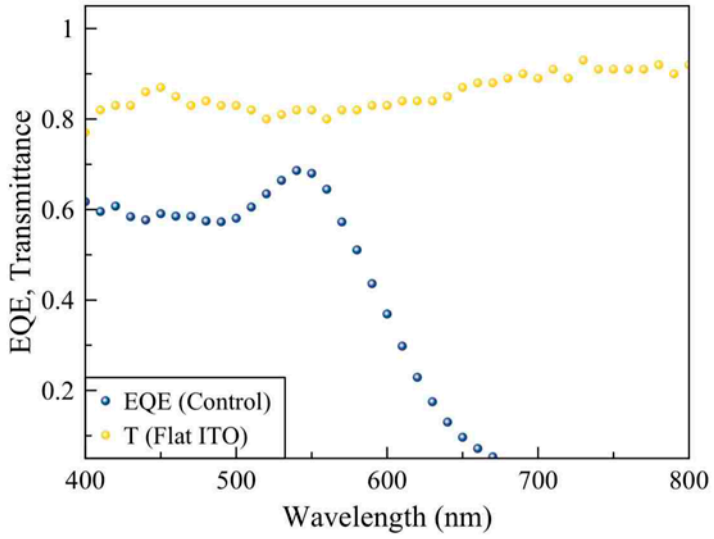


Figure 5.11. The a-Si hybrid PV EQE profiles compared with incident light transmittance through flat ITO/glass and 1:4 diluted NPs embedded substrates: Control device built on flat ITO/glass substrate and the flat ITO/glass transmittance.

However, given the 1:4 diluted NPs embedded in the hybrid cells, the EQE and transmittance gap in that wavelength range is notably reduced (Figure 5.12). At the wavelength of 550 nm, even all the transmitted photons through the substrate seem to be converted to photo-carriers and get extracted for power efficiency. This is remarkable since internal quantum efficiency is almost reaching 100 % in 90 nm-thick intrinsic a-Si photoactive layer, as we discussed in Chapter 1.3. Here we should note that the a-Si thickness used in this study is comparable to the diffusion length of ~80 nm, which has been reported in Chapter 3.2.

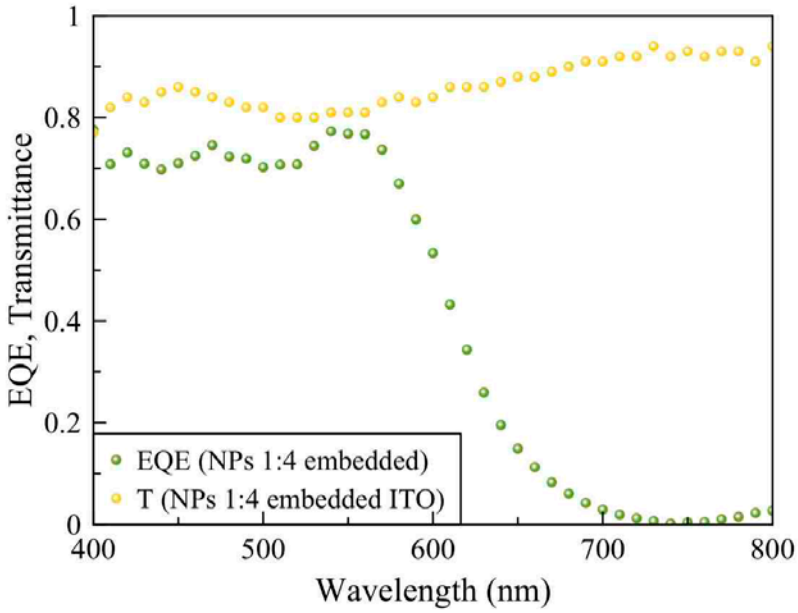


Figure 5.12. The a-Si hybrid PV EQE profiles compared with incident light transmittance through flat ITO/glass and 1:4 diluted NPs embedded substrates: 1:4 diluted NPs embedded hybrid cell and the NPs embedded ITO/glass transmittance.

Thus we believe that the NPs embedded a-Si hybrid cells suppress the unwanted electron-hole recombination well throughout photoactive layers. Without significant charge loss, as most photogenerated charges are efficiently extracted to electrodes in both control and NPs embedded devices, the EQE enhancement is solely attributed to a-Si absorption increase benefited by the light management structures made by the silica NPs.

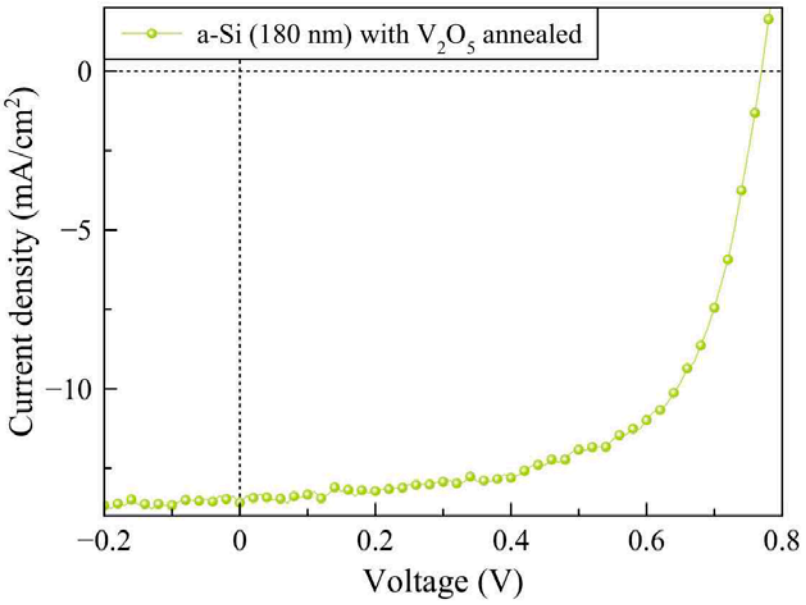


Figure 5.13. The J-V performance of high efficiency a-Si hybrid cell with 180 nm-thick undoped a-Si photoactive layer, additionally optimized by thermal annealing $V_2O_5$ hole transport layer.

The proposed a-Si hybrid cells, introduced above throughout various characterizations, have quite impactful advantages over traditional p-i-n a-Si photovoltaic cells [3], [6]-[10]. However, for solar energy harvesting purpose, electric power conversion efficiency (PCE) is the most important factor in practical [11]-[17]. By developing our hybrid cell for high efficiency cell, we are able to project how high efficiency we ultimately expect to reach when applying the NPs embedded light management structure. For high PCE performance, we have employed 180 nm a-Si photoactive layer and have thermal annealed $V_2O_5$ for better hole conductivity at anode as demonstrated in Figure 5.13. The a-Si thickness is twice larger than the previously measured diffusion length (~80 nm), which believed to be improved further by enhancing intrinsic a-Si quality in our future work. The J-V curve represents the average efficiency

of 6.7 % of the 180 nm a-Si hybrid cells on flat ITO/glass substrates. The average $J_{sc}$ of 13.6 mA/cm$_2$, open circuit voltage ($V_{oc}$) of 0.77, and fill factor of 64 % have been obtained. If we assume that the ~15 % $J_{sc}$ increase is applied to the 180 nm-thick hybrid cell as in 100 nm-thick device, we anticipate to have almost 8 % a-Si PVs using a half thick a-Si of conventional ones without any doping processes. As we mentioned earlier, we need to optimize intrinsic a-Si quality and investigate the high efficiency a-Si hybrid cells, which can potentially compete with the current thin-film a-Si solar panels in the market.

## 5.3 Aluminum Foil for Light Scattering Surface

In Chapter 5.1, we observed that light scattering effect by the silica nanoparticles (NPs) embedded ITO underneath of undoped a-Si helps to improve power efficiency performance by enhancing short circuit current density ($J_{sc}$) performance. Encouraged by the light scattering effect on the a-Si hybrid cells, we began looking into possible light scattering substrates. One of the easily accessible materials, a commercial Al-foil has matte look on a backside, which potentially implies that light gets scattered on the Al-foil surface. Thus we take a look at the confocal optical image of the backside Al-foil by using the surface roughness measurement mode of three-dimensional measuring laser microscope (Olympus LEXT), as shown in Figure 5.14. We can easily notice that the Al-foil surface has randomly roughened morphology, which is anticipated to induce light scattering and matte look. Since the laser microscope image is in 130 μm by 130 μm, we

characterize a smaller area of Al-foil surface by atomic force microscopy (AFM) in order to measure roughness height within wavelength range of absorbed light by a-Si (400 – 600 nm).

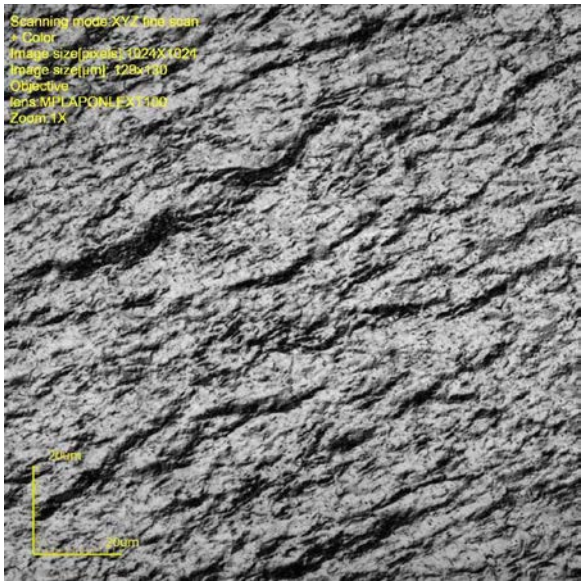


Figure 5.14. The roughness analysis of commercial Al-foil in 130 μm by 130 μm by three-dimensional measuring laser microscope (Olympus LEXT model) equipped with confocal optical system.

In Figure 5.15, we can find a randomly roughened surface of Al-foil measured by AFM in 2 μm by 2 μm. Here the roughness height shows very wide range of variation ranging up to 50 nm. According to the random roughness and height variation, we believe the Al-foil surface morphology will help a-Si trap and absorb more light scattered, which will eventually improve $J_{sc}$ and power conversion efficiency of our a-Si hybrid cells.

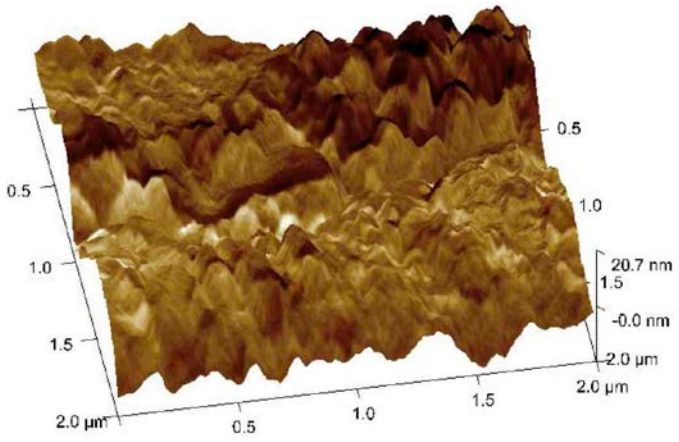


Figure 5.15. The AFM image of commercial Al-foil in 2 µm by 2 µm showing randomly roughened surface of Al-foil, which potentially induces light scattering.

The various fabricated Al-foil based devices are shown in Figure 5.16. A whole a-Si hybrid cell structure, including a 1 mm diameter metal cathode, is fabricated on backside of Al-foil substrate as depicted at the center of Figure 5.16. Next in order the light to be incident on the Al-foil pattered ITO anode side, we etch Al-foil by Al etchant with silicon dioxide ($SiO_2$) etch mask, which will be discussed in Figure 5.17. After Al-foil etching, the fabricated a-Si hybrid devices with 1 mm diameter cathodes are exposed through the etched substrates (Figure 5.16). We see the hybrid devices through ITO anode with Al-foil opened as round shaped. Also, as the Al-foil is very light and flexible with ultra-thin a-Si hybrid cell layers, we expect the Al-foil based hybrid cells can be used for various applications where light-weighted flexibility is required. But the fabrication scalability should be verified further, as always, for commercial large-area production.

Figure 5.16. The images of Al-foil substrate based undoped a-Si hybrid photovoltaic devices: The random light scattering surface morphology of Al-foil is used after etching of the Al-foil substrate (shown as round shaped on the Al-foil in the images).

Figure 5.17 depicts the fabrication process of the Al-foil based a-Si hybrid cells, which potentially support scalability for commercial applications. The fabrication starts from Al-foil substrate with the backside (matte look) up. We first deposit 1 μm silicon dioxide ($SiO_2$) to utilize for the support of whole structure after Al-foil etching and for a etch mask. Beginning with 200 nm ITO, we finish whole a-Si hybrid device structure with 1 mm diameter Al cathode on top. In order to open a light path through ITO anode, we etch Al-foil by Al etchant for about 10 minutes at around 75 °C on a hot plate in a fume hood where acidic gas byproduct detained. If we want to increase the speed of etching, we can use higher temperature for etching, but sudden stress change in the ultra-thin film would cause cracks throughout the film. After the Al etching process, we wash the ITO anode and $SiO_2$ side substrate with deionized water to get rid of any etchant and

its byproducts, which would later induce continuous chemical attack on the oxide film. The ultra-thin film is further protected by optically transparent UV-curable Norland Optical Adhesives (NOA) [18], which supports the whole hybrid structure as a plastic substrate. The 100 W UV cures the casted NOA by illuminating about 5 minutes, which depends on UV power and the NOA type. With the fabricated a-Si hybrid cells, we analyze the $J_{sc}$ and power conversion efficiency of the Al-foil based cells compared to the ones on flat glass substrates.

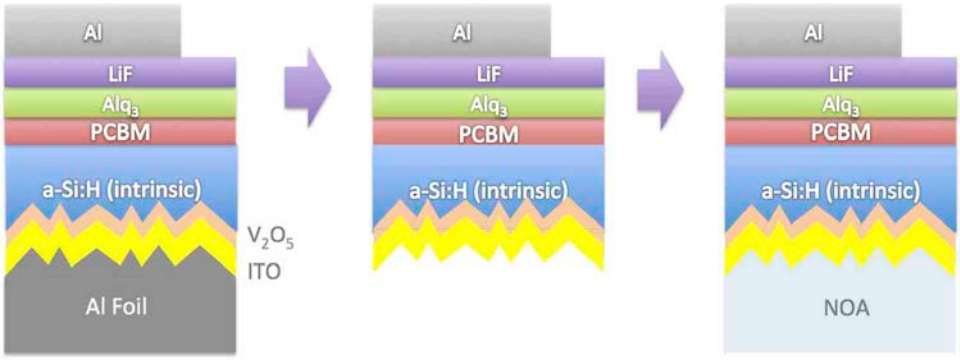


Figure 5.17. The fabrication process of intrinsic a-Si hybrid devices on Al-foil substrates: Based on Al-foil substrates, around 200 nm of ITO with 1 μm silicon dioxide ($SiO_2$) beneath is deposited. All the layers of the a-Si hybrid cells are fabricated on top with the Al cathode in the last step. The Al-foil substrate is etched by Al etchant for about 10 minutes at around 75 °C on a hot plate. After the etching and washing in the etched area, we build an optically transparent plastic substrate by casting UV-curable Norland Optical Adhesives (NOA).

The current density-voltage (J-V) curves of Figure 5.18 show about 30 % improvement in $J_{sc}$ of the hybrid cell on the Al-foil patterned substrate compare to the one on a flat glass substrate. The $J_{sc}$ of the Al-foil based hybrid cell is over 14 $mA/cm^2$ thereby producing around 6 % power conversion efficiency with 100 nm a-Si active layer. This very noticeable enhancement in $J_{sc}$ and power efficiency is further supported

by external quantum efficiency (EQE) curves in Figure 5.19, which illustrates broad absorption increase in whole visible wavelength range.

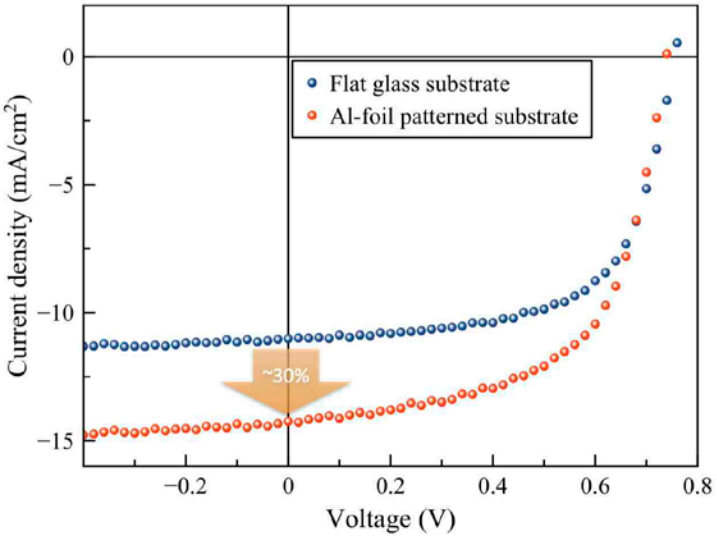


Figure 5.18. The J-V performance of high efficiency a-Si hybrid cell with 100 nm-thick undoped a-Si photoactive layer with the Al-foil surface patterned light scattering substrate: The current density of an Al-foil substrate based hybrid cell is improved by around 30 % compared to a control hybrid cell on a flat glass substrate.

In Figure 5.19, we observe the broad enhancement in EQE throughout whole visible wavelength region, which a-Si absorbs strongly. We believe the broadness is from the random nanostructures patterned by Al-foil creating light scattering inside a-Si photoactive layer [12]-[17], [19].

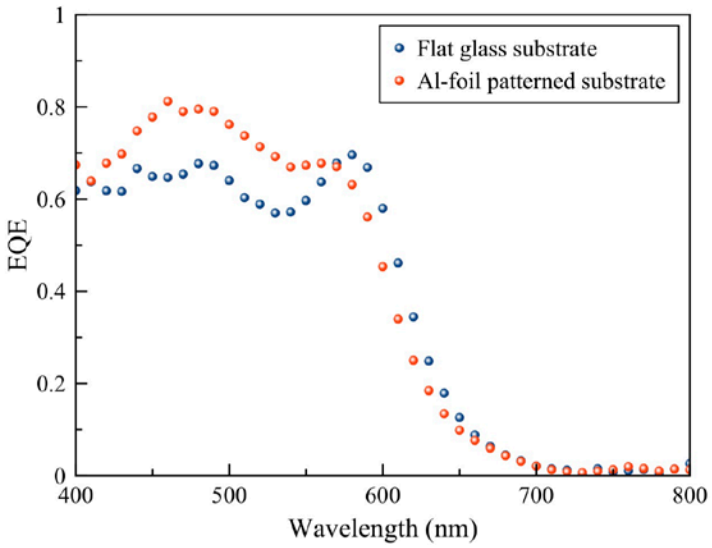


Figure 5.19. The EQE performance of high efficiency a-Si hybrid cell with 100 nm-thick undoped a-Si photoactive layer with the Al-foil surface patterned light scattering substrate: The broad enhancement is observed in the 400-600 nm range of the EQE spectrum for an Al-foil substrate based hybrid cell compared to a control hybrid cell on a flat glass substrate.

We suggest the use of Al-foil backside (matte look) for randomly roughened light scattering pattern, which demonstrates $J_{sc}$ and EQE improvement for our undoped a-Si hybrid photovoltaic devices. The commercial Al-foil is low-cost and easily accessible component for the fabrication process, which is a big benefit especially when we think of potential production scalability. With the use of Al-foil surface pattern for light scattering, we believe that more optimization of the layers in a-Si hybrid devices, incorporating different types of electrodes as introduced in Chapter 1.6, will guide to higher power efficiency towards 10 % [8].

## 5.4 Conclusion

In this chapter, we have studied the undoped a-Si hybrid photovoltaics (PVs) with enhanced light absorption by the silica nanoparticles (NPs) embedded indium-tin oxide (ITO) substrates. By optimizing the NPs concentration before solution casting, we have improved $J_{sc}$ by ~15 % over the hybrid cell on flat ITO/glass substrate. The external quantum efficiency (EQE) characteristics and their comparison to the light transmittance through the NPs embedded and flat ITO substrates empirically support the light absorption increase in undoped a-Si photoactive layer. Since, in practical use, high power efficiency of the hybrid cell is important, we optimized the hybrid structure with 180 nm-thick undoped a-Si, thus producing ~6.7 % power conversion efficiency. Provided by the efficient light management structures studied in this chapter, we can anticipate efficiency increase up to almost 8 %. As another way to create light scattering in the a-Si hybrid cells, we employed commercial Al-foil, which has the matte look surface on its backside. The rough surface was characterized by three-dimensional measuring laser microscopy as well as atomic force microscopy (AFM). The Al-foil surface could be patterned on ITO substrate after Al-foil substrate is etched. As a result, the Al-foil based hybrid cell attained around 14 $mA/cm^2$ of $J_{sc}$, thereby achieving over 6 % power efficiency with 100 nm a-Si layer, which was about 30 % improvement compared to the cell on a flat glass substrate. Therefore we believe that the proposed intrinsic a-Si hybrid cells are beneficial for enhanced a-Si light absorption by light scattering effect, consequently leading to higher power conversion efficiency.

# References


[1] J. Meyer, K. Zilberberg, T. Riedl, and A. Kahn, "Electronic structure of Vanadium pentoxide: An efficient hole injector for organic electronic materials," *J. Appl. Phys.*, vol. 110, no. 3, p. 033710, 2011.

[2] S. Krishnakumar and C. S. Menon, "Optical and electrical properties of vanadium pentoxide thin films," *Phys. Stat. Sol*, vol. 153, pp. 439–444, 1996.

[3] J. Loffler, R. Groenen, J. L. Linden, M. C. M. van de Sande, and R. E. I. Schropp, "Amorphous silicon solar cells on natively textured ZnO grown by PECVD," *Thin Solid Films*, vol. 392, pp. 315–319, 2001.

[4] Y. He, H.-Y. Chen, J. Hou, and Y. Li, "Indene−C 60Bisadduct: A New Acceptor for High-Performance Polymer Solar Cells," *J. Am. Chem. Soc.*, vol. 132, no. 4, pp. 1377–1382, Feb. 2010.

[5] H.-L. Yip and A. K. Y. Jen, "Recent advances in solution-processed interfacial materials for efficient and stable polymer solar cells," *Energy Environ. Sci.*, vol. 5, no. 3, pp. 5994–6011, 2012.

[6] J. Y. Lee, T. Lee, H. J. Park, and L. J. Guo, "Improved solar cell performance by adding ultra-thin Alq3 at the cathode interface," *Organic Electronics*, vol. 15, no. 11, pp. 2710–2714, Nov. 2014.

[7] J. Y. Lee, K.-T. Lee, S. Seo, and L. J. Guo, "Decorative power generating panels creating angle insensitive transmissive colors," *Sci. Rep.*, vol. 4, Feb. 2014.

[8] T. Söderström, F. J. Haug, X. Niquille, and C. Ballif, "TCOs for nip thin film silicon solar cells," *Prog. Photovolt: Res. Appl.*, vol. 17, no. 3, pp. 165–176, May 2009.

[9] S. Il Park, S. Jae Baik, J.-S. Im, L. Fang, J.-W. Jeon, and K. Su Lim, "Towards a high efficiency amorphous silicon solar cell using molybdenum oxide as a window layer instead of conventional p-type amorphous silicon carbide," *Appl. Phys. Lett.*, vol. 99, no. 6, p. 063504, 2011.

[10] X. Deng and E. A. Schiff, "Amorphous Silicon–based Solar Cells," *Handbook of*

*Photovoltaic Science and Engineering (Edited by A. Luque and S. Hegedus)*, pp. 505–565, Mar. 2003.

[11] A. V. Shah, H. Schade, M. Vanecek, J. Meier, E. Vallat-Sauvain, N. Wyrsch, U. Kroll, C. Droz, and J. Bailat, "Thin-film silicon solar cell technology," *Prog. Photovolt: Res. Appl.*, vol. 12, pp. 113–142, 2004.

[12] H. Tan, R. Santbergen, A. H. M. Smets, and M. Zeman, "Plasmonic Light Trapping in Thin-film Silicon Solar Cells with Improved Self-Assembled Silver Nanoparticles," *Nano Lett.*, vol. 12, no. 8, pp. 4070–4076, Aug. 2012.

[13] M. G. Deceglie, V. E. Ferry, A. P. Alivisatos, and H. A. Atwater, "Design of Nanostructured Solar Cells Using Coupled Optical and Electrical Modeling," *Nano Lett.*, vol. 12, no. 6, pp. 2894–2900, Jun. 2012.

[14] X. Chen, B. Jia, J. K. Saha, B. Cai, N. Stokes, Q. Qiao, Y. Wang, Z. Shi, and M. Gu, "Broadband Enhancement in Thin-Film Amorphous Silicon Solar Cells Enabled by Nucleated Silver Nanoparticles," *Nano Lett.*, vol. 12, no. 5, pp. 2187–2192, May 2012.

[15] C. Battaglia, C.-M. Hsu, K. Söderström, J. Escarré, F.-J. Haug, M. Charrière, M. Boccard, M. Despeisse, D. T. L. Alexander, M. Cantoni, Y. Cui, and C. Ballif, "Light Trapping in Solar Cells: Can Periodic Beat Random?," *ACS Nano*, vol. 6, no. 3, pp. 2790–2797, Mar. 2012.

[16] C. Battaglia, J. Escarré, K. Söderström, M. Charrière, M. Despeisse, F.-J. Haug, and C. Ballif, "Nanomoulding of transparent zinc oxide electrodes for efficient light trapping in solar cells," *Nature Photonics*, vol. 5, no. 9, pp. 535–538, Aug. 2011.

[17] C. Battaglia, J. Escarré, K. Söderström, L. Erni, L. Ding, G. Bugnon, A. Billet, M. Boccard, L. Barraud, S. De Wolf, F.-J. Haug, M. Despeisse, and C. Ballif, "Nanoimprint Lithography for High-Efficiency Thin-Film Silicon Solar Cells," *Nano Lett.*, vol. 11, no. 2, pp. 661–665, Feb. 2011.

[18] J. Yoon, L. Li, A. V. Semichaevsky, J. H. Ryu, H. T. Johnson, R. G. Nuzzo, and J. A. Rogers, "Flexible concentrator photovoltaics based on microscale silicon solar cells embedded in luminescent waveguides," *Nature Communications*, vol. 2, pp. 343–8, Jun. 2011.

[19] V. E. Ferry, M. A. Verschuuren, M. C. V. Lare, R. E. I. Schropp, H. A. Atwater, and A. Polman, “Optimized Spatial Correlations for Broadband Light Trapping Nanopatterns in High Efficiency Ultrathin Film a-Si:H Solar Cells,” *Nano Lett.*, vol. 11, no. 10, pp. 4239–4245, Oct. 2011.

# Chapter 6

# Potential Applications of Ultra-thin a-Si Hybrid Cells

## 6.1 Introduction

Lastly, Chapter 6 suggests that the ultra-thin a-Si device can be a very effective structure for various applications including high-speed photo-detectors and ultraviolet (UV) light-blocking windows. Based on the transient photocurrent and phovoltage characteristics of the undoped a-Si hybrid devices in Chapter 3.2, we have found the ultra-thin a-Si hybrid devices have very fast responses to the stimulated light input, thereby potentially applicable for high-speed photo-detectors. As experimentally verified in Chapter 6.1, the proposed device shows very suppressed dark current as well, which will eventually improve signal-to-noise ratio of the photo-detector device. We have fabricated and operated a-Si hybrid photo-detector arrays in order to demonstrate the high-speed performance. We also show that the a-Si hybrid photo-detector arrays can be built for a transparent human touch interactive screen where photocurrent density shifts if the detector cell touched or blocked from surrounding light. Since the ultra-thin a-Si (a few nanometer-thick) hybrid device provides optical transparency, the hybrid device can

operate as UV light-blocking windows, creating electric power as well, due to strong UV light absorption by even a single nanometer a-Si.

## 6.2 High-speed Photo-detector Application

In Figure 6.1, we propose a photo-detector device structure incorporating tungsten oxide ($WO_3$)/silver (Ag)/tungsten oxide ($WO_3$) transparent anode as introduced in Chapter 1 [1]-[4]. The same charge transport materials of vanadium pentoxide (V2O5) and indene-C60 bisadduct (ICBA) are used for photogenerated charge extraction as in the other chapters (from Chapter 3 to Chapter 5) [5], [6]. As an interfacial layer with aluminum (Al) for Ohmic contact, *tris*(8-hydroxyquinoline) aluminum ($Alq_3$) 2 nm is thermally evaporated right before Al deposition [7]. Here we use $Alq_3$ (2 nm) instead of $Alq_3$ (1 nm)/LiF (1 nm) since, regarding photo-detector performance, the former provides very similar photocurrent generation performance to the latter. The undoped a-Si thickness ranges from 50 nm to 100 nm relying on the amount of photocurrent needed for various purposes. The photo-detector arrays are formed with crossbar type cathode and anode, whose schematic is simplified in Figure 6.1.

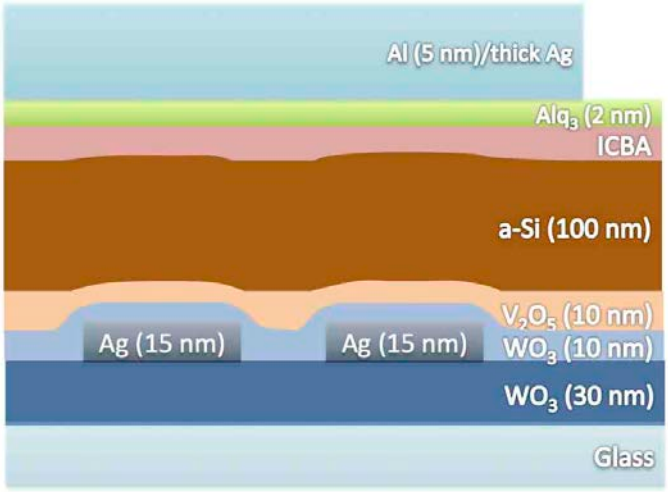


Figure 6.1. Proposed device structure for a-Si hybrid photo-detector arrays.

Since ultra-thin a-Si hybrid device structure shows very fast photo-response as proved in Chapter 3.2, we investigate the hybrid devices further for high-speed photo-detector applications. The outstanding photo-response, either photocurrent or photovoltage (Chapter 3.2), provides transient rise and fall time within 1 μs (photocurrent in Figure 6.2), which greatly outperforms the recently reported fastest response of 0.3 msec in a-Si/$MoS_2$ photo-detectors [8]. Moreover, the ultra-thin a-Si hybrid structure satisfies commercial photo-detector sensitivity requirement as well by producing high quantum efficiency over low dark current density (> $5\times10^{-8}$ $cm^2$/A) [9].

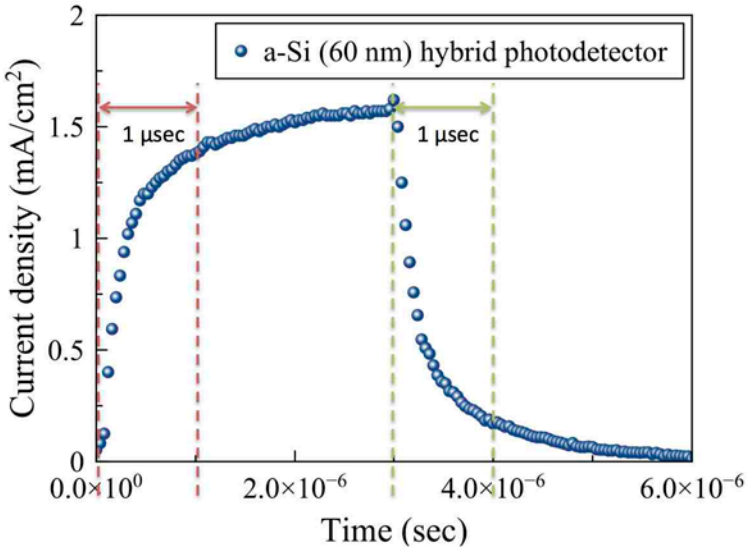


Figure 6.2. High-speed photo-response of the rise and fall time, less than 1 µsec, in the current density of the a-Si hybrid photo-detector.

With the proposed device structure in Figure 6.1, we demonstrate 4 by 4 arrays as depicted in Figure 6.3 by implementing data-read analog circuits and user interface software. With the input light (520 nm green LED) source illuminating the photo-detector arrays, the proposed photo-detector arrays should be able to recognize the light intensity distribution and respond with the corresponding amplitude of electric current at short circuit condition (Figure 6.3).

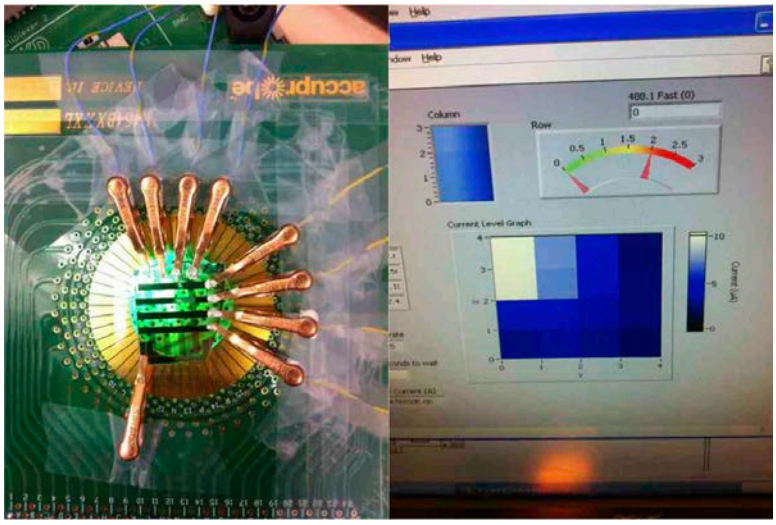


Figure 6.3. 4 by 4 a-Si hybrid photo-detector array experimental set-up and real-time detection (over 700 frames/sec) user interface on computer screen.

We believe that the high-speed a-Si hybrid photo-detector arrays can be applied to higher resolution real-time imaging system as illustrated in Figure 6.4. Potentially, the real-time imaging system can be also designed to run faster by central processing unit (CPU) and input/output peripherals of field programmable gate arrays (FPGAs). With integrating the a-Si hybrid detector arrays with system-on-a-chip such as FPGA, in medical application as an example, the digital radiography can employ the hybrid photo-detector array solution in flat panel detectors (FPDs) [10]-[12]. If we assume an optimized scintillator, which converts X-ray to visible light in the wavelength range of 500 ~ 600 nm [9], [12], is equipped, the a-Si hybrid photo-detector arrays receive continuous frames of a video in real time (Figure 6.3). Here the major figures of merits for photo-detectors in FPDs are the sensitivity and speed of the visible light detection [8], [12]. We believe that faster response by the a-Si hybrid photo-detectors along with high

sensitivity leads to high frame-rate video with short X-ray exposure time and dose in the surgical imaging system [11].

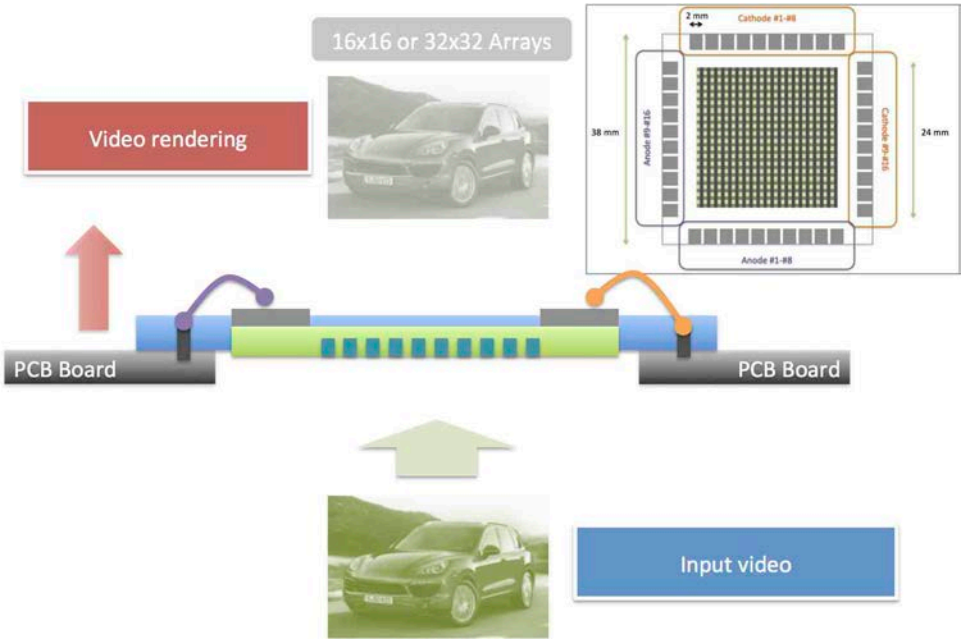


Figure 6.4. Higher resolution imaging system by using a-Si hybrid photo-detector arrays: The arrays of photo-detector pixels are denoted as 16 by 16 or 32 by 32.

As we discussed in the previous chapters, for the undoped a-Si hybrid devices, the high internal quantum efficiency (IQE) is attributed to the ultra-thin a-Si thickness, which is much smaller than charge diffusion length, which calculated in Chapter 3.2 [13], thereby suppressing possible electric charge losses. For the reduced dark current (Figure 6.5), the hybrid charge transport layers contribute to selective charge extraction at electrodes, mitigating unwanted charge leakage. At electron charge transporting interface, we show that the ICBA layer double sandwiched by $Alq_3$ layers with one $Alq_3$ (2 nm) right next to aluminum electrode provide much suppressed dark current. Moreover,

according to the ultra-thin a-Si engineered by the undoped principle, the accurate optical design to maximize EQE in any visible wavelength is also available regardless of scintillator type in medical imaging [12], [14]. In addition, the simplicity of fabrication is another merit of this work, which will guide us to scale the device to large-size detector panel.

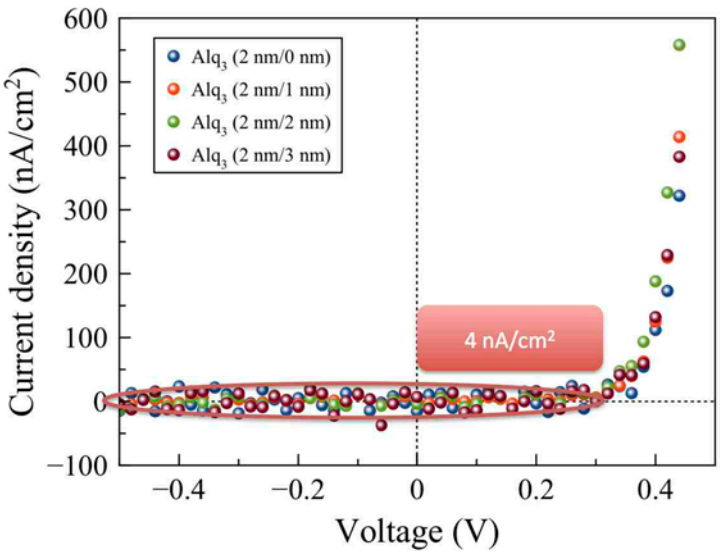


Figure 6.5. Suppressed dark current with $Alq_3$ (2 nm) interfacial layer at aluminum cathode in the a-Si hybrid device structure: Additional $Alq_3$ layer (0-3 nm) applied beneath ICBA to reduce the dark current as such.

We investigate the photodiode performance of ultra-thin a-Si photo-detector by comparing with crystalline silicon (c-Si) photodiode features as listed in Table I. Notably, the a-Si hybrid photo-detector operates at zero bias without any reverse bias voltage, which is required for c-Si photodiode. Also, photo-response spectrum can be easily modulated by optically designing the multi-layer a-Si hybrid structures, thereby tuning a-Si absorption spectrum accordingly. Since we deposit a-Si by plasma enhanced chemical

vapor deposition (PECVD) in vacuum with solution-casting and thermal evaporation for the other layers, the fabrication of the hybrid photo-detector arrays is scalable, which does not apply to c-Si photodiode. As we discussed in Figure 6.6, the a-Si hybrid photo-detector has well suppressed dark current density, thus it is very comparable even to c-Si detector just by around one order of magnitude difference.

Table 6.I. Performance comparison between crystalline silicon photodiode and ultra-thin a-Si (60 nm) diode, emphasizing the benefits of the ultra-thin a-Si hybrid device.

| | Crystalline Si photodiode* | Ultra-thin a-Si (60 nm) diode |
|---|---|---|
| Maximum spectrum range [nm] | 190 ~ 1100 | 150 ~ 700 |
| Photo sensitivity [A/W] @ 520 nm | 0.3 | 0.15 |
| Dark current density [nA/cm$^2$] | 0.4 @ -1 V | 4 @ -1 V |
| Operation bias [V] | -20 ~ -1 | 0 |
| Rise time [nsec] | 10 ~ 250 | 1000 |
| Cut-off frequency [MHz] | 10 ~ 2000 @ Reverse bias | 1 @ Zero bias |
| Various photo-response spectrum | Filter is needed | Tunable |
| Large area diode | Up to 3 cm by 3 cm | Determined by vacuum chamber size |
| Integration with a system | Complex | Easy |

(* Sources: Hamamatsu, Inc., OSI optoelectronics)

Based on the device structure in Figure 6.1, we can easily design to fabricate transparent ultra-thin a-Si hybrid photo-detectors. We believe that, if the transparent a-Si photo-detectors are integrated with an interactive screen as shown in Figure 6.6, the

transparent detector arrays can detect human touch, and harvest light energy at the same time if needed.

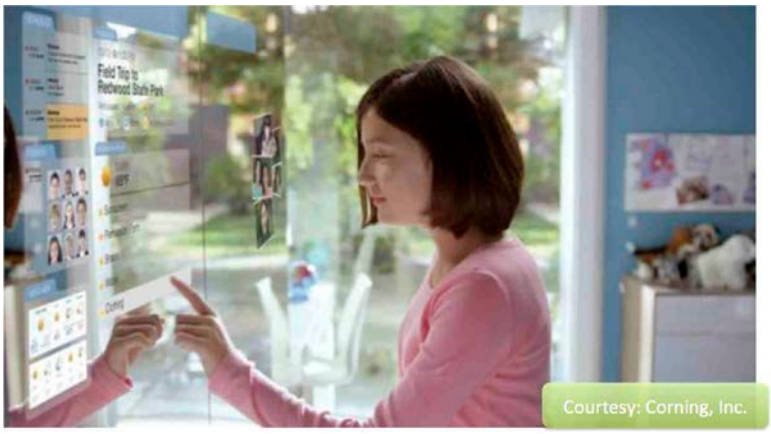


Figure 6.6. Human touch interactive transparent screen products. (Source: Corning, Inc.)

The device structure of transparent a-Si hybrid photo-detector arrays is depicted in Figure 6.7 where both cathode and anode are applied as transparent electrodes.

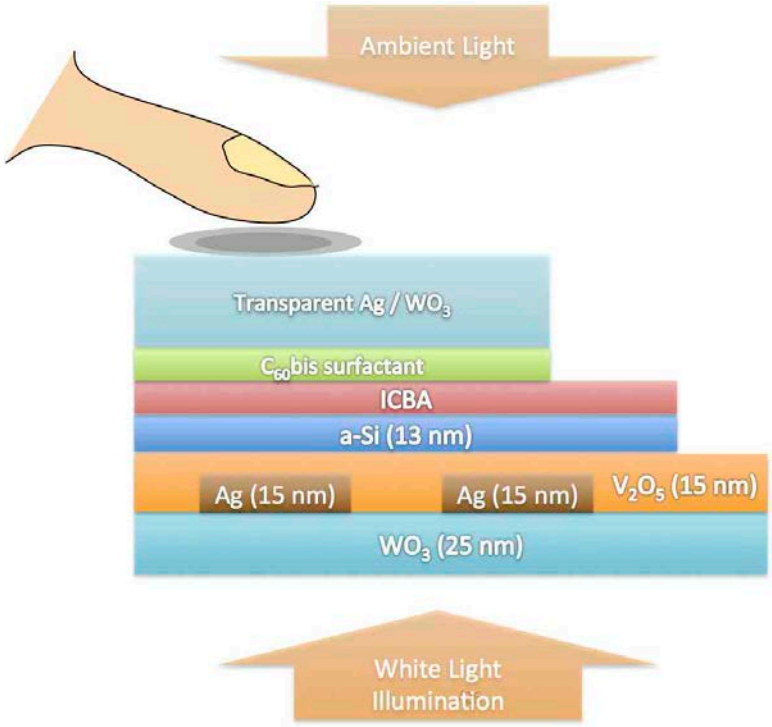


Figure 6.7. Transparent a-Si hybrid photo-detector arrays for human touch interactive screen products, harvesting light energy for electric power as well.

From Figure 6.7, we can observe that, if a human finger approaches or touches the transparent cathode, the a-Si hybrid photo-detector senses it by recording the photocurrent density shift regardless of ambient light on top of the detectors. The photocurrent density varies as described in Figure 6.8. The photocurrent characteristics clearly show that, with a touch on the photo-detector cathode, about 15 % photocurrent shift is detected, which is believed to be big enough to sense whether the detector pixel is indicated or not. In the experiment, we use white light illumination as a back light source for a general display screen. With the approached finger on the photo-detector pixel, the white light gets reflected from the finger skin so that the a-Si of the pixel absorbs more light to increase the current density. Here the photosensitivity of 50 mA/W plays an

important role in touch sensitivity. Certainly, we admit that this operation or principle can vary according to the display system where the photo-detector arrays get implemented.

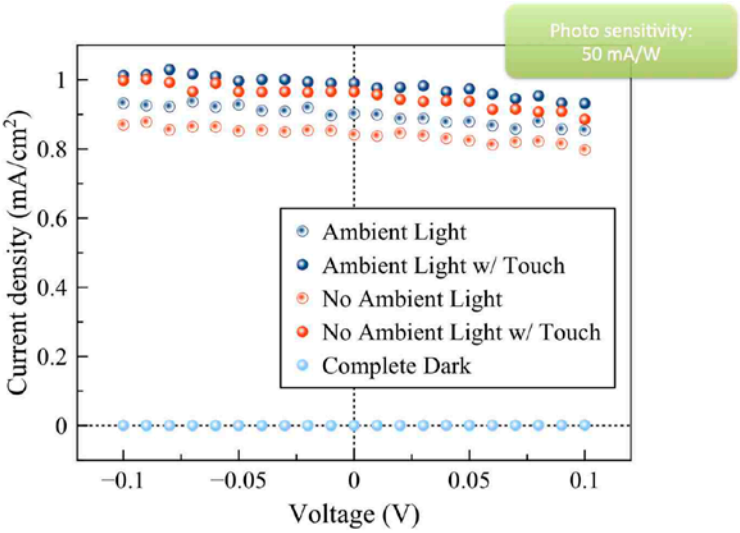


Figure 6.8. The photocurrent of transparent a-Si hybrid photo-detector varies according to human touch on the photo-detector arrays (Photo sensitivity: 50 mA/W).

Since recent or future displays are continuously getting bigger, the photo-detector arrays should be scalable in production. As we discussed earlier in this chapter, the ultra-thin a-Si photo-detector arrays incorporate the scalable materials and deposition methods. Figure 6.9 illustrates the fabrication of the transparent arrays with a-Si sandwiched by crossbar type cathode and anode grids that are transparent as well. The two-dimensional arrays collect the information where a finger touch point is on the opposite side from backlight illumination as indicated with x and y axes lines in Figure. 6.9.

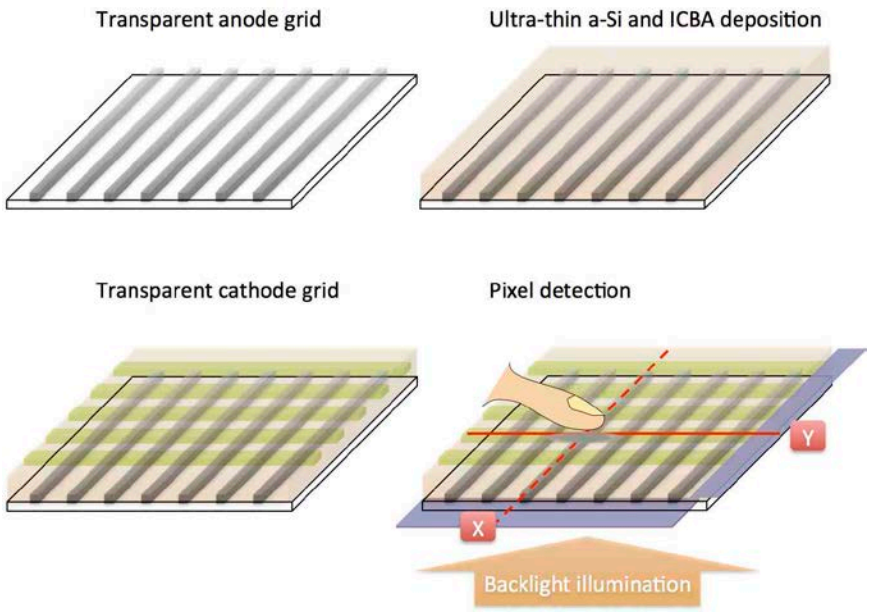


Figure 6.9. Fabrication schematics of the transparent ultra-thin a-Si hybrid photo-detector arrays with an illustration of finger touch on a (x) by (y) pixel.

## 6.3 Ultraviolet light-blocking Transparent Power-generating Windows

The transparent power-generating feature of the ultra-thin a-Si hybrid cells can be well utilized for building windows as we introduced in Chapter 4.3. In this chapter, we suggest another use of the power-generating transparent window in harmful ultraviolet (UV) light blocking. The efficient and strong UV light absorption, while transmitting other visible wavelengths, is designed to be available by unprecedented few-nanometer a-Si hybrid cells without any doped layers, which have not been expected to work for many years [15]-[19]. Before designing the transparent a-Si hybrid structures, we first verify that a few nanometer (1-4 nm) a-Si in the hybrid structures absorbs UV light well as shown in Figure 6.10.

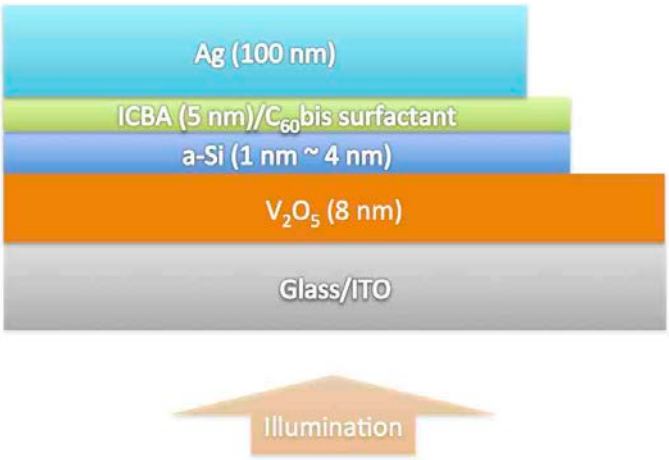


Figure 6.10. Proposed device structure for a few nanometer a-Si hybrid devices as efficient ultraviolet (UV) light absorbers as well as electric power-generating cells.

As evidences of the few nanometer a-Si hybrid devices absorbing UV light and power-generating, we run electrical characterizations such as current density-voltage (J-V) (Figure 6.11) and external quantum efficiency (EQE) (Figure 6.12) characteristics. As reported in Figure 6.11, even a-Si (1 nm) hybrid cell harvest light energy for electric energy. As easily expected, the thicker a-Si (3 or 4 nm) shows higher short circuit current density ($J_{sc}$) as we discussed in Chapter 4.3.

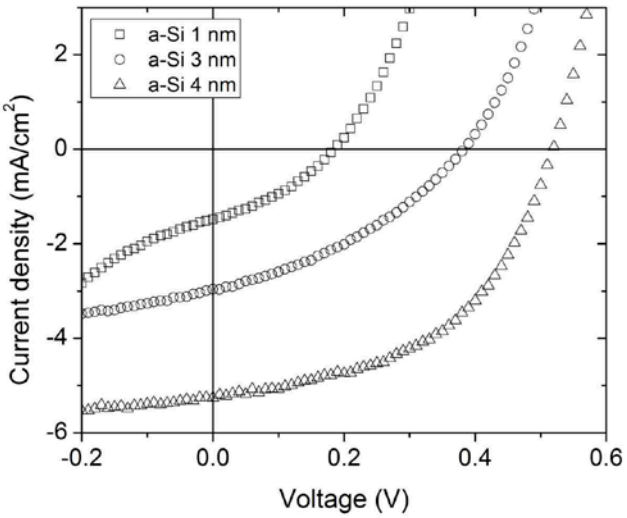


Figure 6.11. The current density-voltage (J-V) characteristics of proposed few nanometer-thin a-Si power-generating UV light absorbers.

Since we are interested in UV light absorption by a few nanometer a-Si alongside power-generation (Figure 6.11), the EQE curves of the a-Si hybrid cells are provided in Figure 6.12. Even if the wavelength axis covers 400-700 nm, we clearly see the EQE increases gradually towards UV region regardless of a-Si thickness. As the ultra-thin a-Si hybrid cells have almost 100 % internal quantum efficiency as we observed in Chapter 4, we can define the EQE spectra as a-Si absorption. From the undoped a-Si (3 nm) hybrid cell, we expect to block 60~70 % UV light (Figure 6.12), generating electric power at the same time (Figure 6.11).

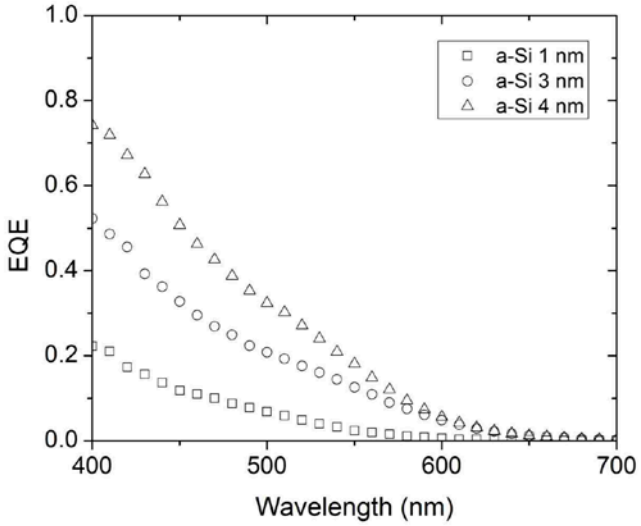


Figure 6.12. The external quantum efficiency (EQE) characteristics of proposed few nanometer-thin a-Si power-generating UV light absorbers.

As we already confirmed that a few nanometer a-Si hybrid cells are efficient UV light absorbers while transmitting visible wavelengths, we design whole structure transparent a-Si hybrid cells with the undoped a-Si (3 nm) as described in Figure 6.13.

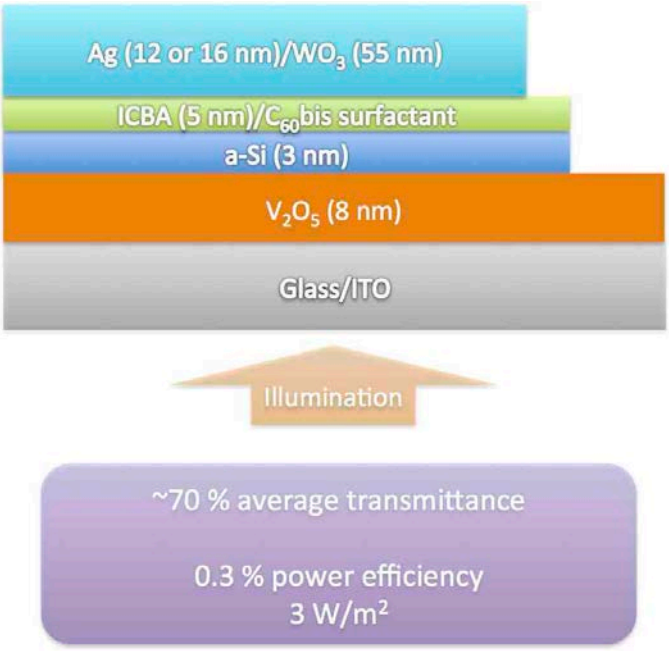


Figure 6.13. Proposed device schematics of transparent power-generating UV light-blocking windows, providing 3 W/m$^2$ electric power and about 70 % transmittance. Two different silver (Ag) thicknesses are used for cathode: window-1 (Ag 12 nm) and window-2 (Ag 16 nm).

Transparent cathode and anode of silver (Ag)/tungsten oxide ($WO_3$) and indium tin oxide (ITO), respectively [1], [7], [14], [20], are incorporated in the transparent a-Si (3 nm) hybrid cells for power-generating UV light-blocking window application. By differentiating Ag thickness to two (12 and 16 nm), we build two different types of windows: window-1 (Ag 12 nm) and window-2 (16 nm). The EQE characteristics of the two types of windows with different thicknesses of Ag will verify whether UV light absorption is affected by the reflection from Ag layer or one-time path absorption before reaching to the Ag/$WO_3$ cathode. First of all, the images of two different windows on campus show how transparent the windows are in Figure 6.14: window-1 (left) and window-2 (right).

Figure 6.14. The images of the left window-1 (Ag 12 nm) and the right window-2 (Ag 16 nm): The window-2 shows a little yellowish transparency compared to window-1.

In Figure 6.14, we observe that, with bare eyes, both windows are so transparent themselves that we can see through the windows. However, if we compare the two windows side-by-side, we easily notice that window-2 (Ag 16 nm) gives a bit yellowish transparency due to the less flattened and lower transmittance than window-1 (Ag 12 nm) as described in Figure 6.15.

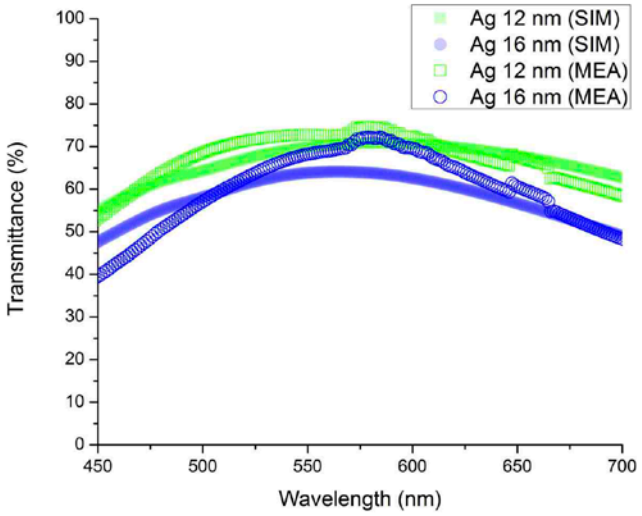


Figure 6.15. The transmittance curves of the window-1 (Ag 12 nm) and the window-2 (Ag 16 nm): The window-1 gives higher and flatter transmittance over window-2.

On the other hand, EQE curves between window-1 and window-2 are not very different, which proves that different Ag thicknesses do not affect the a-Si absorption, thereby giving similar EQE performance. In other words, the absorbed light by a-Si, incorporating UV light and shorter visible wavelength, mostly get absorbed in a single path in the a-Si active layer before even reaching to Ag to be reflected. This experimental result directly supports that a few nanometer a-Si hybrid cells are very appropriate candidates for efficiently UV-blocking transparent windows, which harvest light energy simultaneously, for such as high-rise buildings in Figure 6.17.

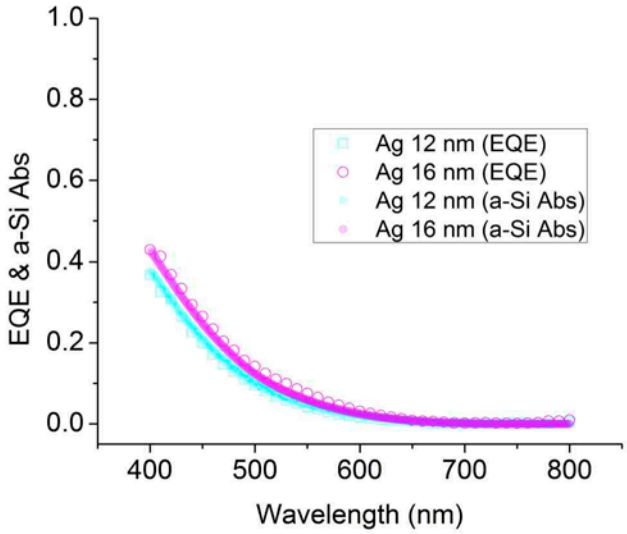


Figure 6.16. The EQE (dotted lines) and a-Si absorption (solid lines) curves of the window-1 (Ag 12 nm) and the window-2 (Ag 16 nm): The window-1 gives higher and flatter transmittance over window-2.

The transparent UV-blocking windows can be very important to keep the hazardous sunlight UV away from our living environment. Also, if the power-generating transparent a-Si hybrid cells cover the vast surface area of high-rise buildings, the generated electricity will help to provide additional renewable energy to the buildings. At the same time, since the transparent windows block UV light, they can prevent issues from affecting people and interior furnishings as reported in Figure 6.17. Using our two types of UV light-blocking windows, we test practically how efficiently the windows absorb UV light by using a real UV source and an optical power meter as illustrated in Figure 6.18.


Figure 6.17. The high-rise buildings covered with enormous amount of windows and the bad effects, such as fading of interior furnishing and possible skin damage, due to the transmitted UV light. (Source: GP Systems (UK) Ltd - www.gpwindowfilms.com)

Figure 6.18 shows that window-1 and window-2 block a great amount of UV light by about 60~70 %. As window-2 has thicker Ag than window-1, it absorbs a little more UV light as anticipated from the EQE and a-Si absorption spectra in Figure 6.16. Here we can find that most UV light passes through the normal glass window as tested. Thus, if we consider any UV light-blocking film or more advanced glass product, our transparent a-Si hybrid cells integrated windows can be a good alternative as they harvest the absorbed UV energy for additional electric power simultaneously. Likewise, we have been opening up various applications, which have never been addressed due to the limit of a-Si thickness, thus spreading the use of ultra-thin a-Si hybrid cells widely from energy harvesters to high-speed photo-detectors.

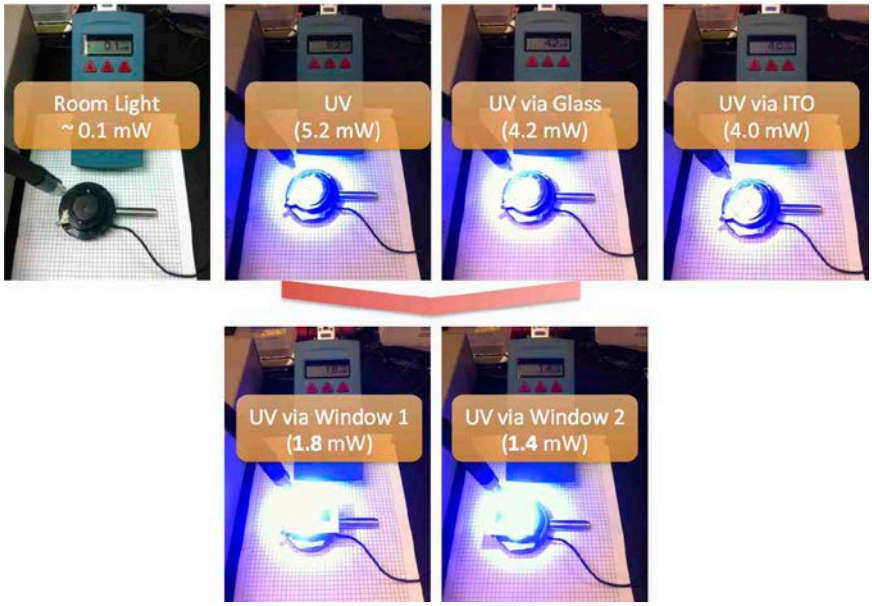


Figure 6.18. The images of UV light-blocking efficiency tests by window-1 (Ag 12 nm) and the window-2 (Ag 16 nm), which are compared to UV light pass through a bare glass substrate or the ITO coated glass.

## 6.4 Conclusion

In summary, we have demonstrated the photo-detector arrays built with undoped amorphous silicon (a-Si) hybrid structures incorporating crossbar type cathode and anode. By utilizing fast photo-response under 1 μsec in the rise and fall time, we were able to run real-time photo-sensing by over 700 frames/sec with 4 by 4 a-Si hybrid photo-detector arrays. We believe to enhance the frame rate further by employing field programmable gate arrays (FPGAs), which are equipped with central processing unit (CPU) and input/output peripherals. With the larger number of pixels for higher resolution, integrated in flat panel detectors (FPDs), real-time medical imaging can be

potentially available. Here the a-Si hybrid cells also have advantage in the suppressed dark current density, below 4 nA/cm$^2$, which is quite comparable to crystalline silicon photodiode. As both anode and cathode can be designed as transparent electrodes, we implemented human touch interactive screen panels as well. With the photo sensitivity of 50 mA/W, the transparent a-Si hybrid photo-detectors showed around 15 % current density variation when a finger approaches so that we can detect the finger indicating point. Moreover, benefited from strong ultraviolet (UV) absorption by a-Si, the transparent a-Si hybrid cells can be applied to UV light-blocking windows with 70 % transmittance, providing 3 W/m$^2$ electric power. We also experimentally investigated that silver (Ag) thickness in the transparent cathode affects both transmittance and UV blocking efficiency, but not in huge difference.

# References


[1] K. Hong, K. Kim, S. Kim, I. Lee, H. Cho, S. Yoo, H. W. Choi, N.-Y. Lee, Y.-H. Tak, and J.-L. Lee, "Optical Properties of WO 3/Ag/WO 3Multilayer As Transparent Cathode in Top-Emitting Organic Light Emitting Diodes," *J. Phys. Chem. C*, vol. 115, no. 8, pp. 3453–3459, Mar. 2011.

[2] L. Shen, Y. Xu, F. Meng, F. Li, S. Ruan, and W. Chen, "Semitransparent polymer solar cells using V2O5/Ag/V2O5 as transparent anodes," *Organic Electronics*, vol. 12, no. 7, pp. 1223–1226, Jul. 2011.

[3] C. Tao, G. Xie, C. Liu, X. Zhang, W. Dong, F. Meng, X. Kong, L. Shen, S. Ruan, and W. Chen, "Semitransparent inverted polymer solar cells with MoO[sub 3]/Ag/MoO[sub 3] as transparent electrode," *Appl. Phys. Lett.*, vol. 95,

no. 5, p. 053303, 2009.

[4] B. Tian, G. Williams, D. Ban, and H. Aziz, “Transparent organic light-emitting devices using a MoO3/Ag/MoO3 cathode,” *J. Appl. Phys.*, vol. 110, no. 10, p. 104507, 2011.

[5] Y. He, H.-Y. Chen, J. Hou, and Y. Li, “Indene−C 60Bisadduct: A New Acceptor for High-Performance Polymer Solar Cells,” *J. Am. Chem. Soc.*, vol. 132, no. 4, pp. 1377–1382, Feb. 2010.

[6] J. Meyer, K. Zilberberg, T. Riedl, and A. Kahn, “Electronic structure of Vanadium pentoxide: An efficient hole injector for organic electronic materials,” *J. Appl. Phys.*, vol. 110, no. 3, p. 033710, 2011.

[7] J. Y. Lee, T. Lee, H. J. Park, and L. J. Guo, “Improved solar cell performance by adding ultra-thin Alq3 at the cathode interface,” *Organic Electronics*, vol. 15, no. 11, pp. 2710–2714, Nov. 2014.

[8] M. R. Esmaeili-Rad and S. Salahuddin, “High Performance Molybdenum Disulfide Amorphous Silicon Heterojunction Photodetector,” *Sci. Rep.*, vol. 3, Aug. 2013.

[9] T. Agostinelli, M. Campoy-Quiles, J. C. Blakesley, R. Speller, D. D. C. Bradley, and J. Nelson, “A polymer/fullerene based photodetector with extremely low dark current for x-ray medical imaging applications,” *Appl. Phys. Lett.*, vol. 93, no. 20, p. 203305, 2008.

[10] J. A. Seibert, “Flat-panel detectors: how much better are they?,” *Pediatr Radiol*, vol. 36, no. 2, pp. 173–181, Jul. 2006.

[11] J. H. Siewerdsen and D. A. Jaffray, “A ghost story: Spatio-temporal response characteristics of an indirect-detection flat-panel imager,” *Med. Phys.*, vol. 26, no. 8, p. 1624, 1999.

[12] P. R. Granfors and D. Albagli, “Scintillator-based flat-panel x-ray imaging detectors,” *J. Soc. Inf. Display*, vol. 17, no. 6, pp. 535–1, 2009.

[13] M. Goerlitzer, N. Beck, P. Torres, J. Meier, N. Wyrsch, and A. Shah, “Ambipolar diffusion length and photoconductivity measurements on ‘“midgap”’ hydrogenated microcrystalline silicon,” *J. Appl. Phys.*, vol. 80, no. 9, p. 5111, 1996.

[14] J. Y. LEE, K.-T. Lee, S. Seo, and L. J. Guo, "Decorative power generating panels creating angle insensitive transmissive colors," *Sci. Rep.*, vol. 4, Feb. 2014.

[15] A. V. Shah, H. Schade, M. Vanecek, J. Meier, E. Vallat-Sauvain, N. Wyrsch, U. Kroll, C. Droz, and J. Bailat, "Thin-film silicon solar cell technology," *Prog. Photovolt: Res. Appl.*, vol. 12, pp. 113–142, 2004.

[16] X. Deng and E. A. Schiff, "Amorphous Silicon–based Solar Cells," *Handbook of Photovoltaic Science and Engineering (Edited by A. Luque and S. Hegedus)*, pp. 505–565, Mar. 2003.

[17] D. E. Carlson and C. R. Wronski, "Amorphous silicon solar cell," *Appl. Phys. Lett.*, vol. 28, no. 11, p. 671, 1976.

[18] J. Loffler, R. Groenen, J. L. Linden, M. C. M. van de Sande, and R. E. I. Schropp, "Amorphous silicon solar cells on natively textured ZnO grown by PECVD," *Thin Solid Films*, vol. 392, pp. 315–319, 2001.

[19] T. Söderström, F. J. Haug, X. Niquille, and C. Ballif, "TCOs for nip thin film silicon solar cells," *Prog. Photovolt: Res. Appl.*, vol. 17, no. 3, pp. 165–176, May 2009.

[20] B. O'Connor, C. Haughn, K.-H. An, K. P. Pipe, and M. Shtein, "Transparent and conductive electrodes based on unpatterned, thin metal films," *Appl. Phys. Lett.*, vol. 93, no. 22, p. 223304, 2008.

# Chapter 7

# Summary and Future Plan

In this dissertation, we extensively studied ultra-thin intrinsic amorphous silicon (a-Si) hybrid structure with inorganic/organic materials. The a-Si hybrid structure has been first introduced in our investigation. In Chapter 2, we proposed the hybrid structure with an undoped a-Si photoactive layer with electron and hole transport layers. The photogenerated charges in undoped a-Si active layer are extracted via the deliberately designed electron and hole transport materials. Optimally, the electron transport layer is built with an organic interfacial layer, indene-$C_{60}$ bisadduct (ICBA); and, for a hole transport layer, we employed metal oxide of vanadium(V) pentoxide ($V_2O_5$) with high work function in order to maximize work function difference between cathode and anode. We name this structure as hybrid device due to inorganic metal oxides used for hole transport (anode) and organic materials for electron transport (cathode). The photovoltaic (PV) performance of the proposed a-Si hybrid devices was assessed by the current density-voltage (J-V) characterization. We experimentally showed how the carefully designed anode and cathode electrical contacts play important roles in determining the power efficiency of the hybrid structures. By optimizing both interfacial layers, we could

achieve about 6 % power conversion efficiency by around 50 nm undoped a-Si on a flat glass substrate.

Based upon the novel ultra-thin a-Si hybrid structure, in Chapter 3, we found and investigated the open circuit voltage variation of a-Si hybrid photovoltaic cells with different undoped a-Si thicknesses (15 nm, 30 nm, and 180 nm). We confirmed the larger ideality factor of the thinner cells in ultra-thin a-Si regime by observing larger $V_{oc}$ change under varied sun concentration. According to our theoretical analysis, image charge effect causes energy barrier reduction at the anode, inducing the thinner hybrid cells to turn on at earlier forward bias under dark condition, and to contain larger saturation current at reverse bias. This analysis has been further supported by empirical characteristics of capacitance-voltage (C-V). We also have reported that a-Si thickness affects photovoltaic power efficiency, especially fill factor in the proposed a-Si hybrid solar cell structure. Larger decrease of fill factor has been observed in a-Si 180 nm device compared to a-Si 30 nm one towards higher solar concentration up to 7 sun. The a-Si thickness dependence on fill factor is further supported by ambipolar carrier diffusion length (~ 80 nm) characteristic by transient response at open circuit condition. We believe that the various characterizations of the undoped a-Si hybrid cells in ultra-thin a-Si regime provide guidelines how to design the undoped hybrid cells for improved power conversion efficiency.

In ultra-thin a-Si regime, the intrinsic a-Si hybrid photovoltaic structure opened up new applications that conventional solar cells could have not been able to challenge.

In Chapter 4, we demonstrated various decorative and transparent amorphous silicon (a-Si) hybrid cells with varied undoped a-Si layer thickness, which generated up to 2 % efficiency in transmissive device and 3 % in the reflective. The use of ultra-thin a-Si layer leads to high angular tolerance of the transmitted and reflected colors (up to around 60°) with high color purity. Notably, most of the absorbed photons in the undoped a-Si layer were converted to the electric charges benefited by the suppressed electron-hole recombination in the ultra-thin a-Si layer, which can significantly mitigate the light-induced degradation of a-Si solar cells as well. We also showed that a cascaded arrangement, exploiting the angle-invariant reflective colored cells, enabled the efficient harvesting of a wide range of incident light energy. Lastly, we experimentally built and proved a single nanometer-thick a-Si solar cell that is unachievable with currently existing a-Si photovoltaic platform owing to primarily relying on doping processes. We also showed that 1.0 $mA/cm^2$ of short circuit current density and 0.35 V of open circuit voltage were accomplished by 3 nm-thick transparent a-Si hybrid device, simultaneously featuring 70 % of average transmittance throughout the entire visible band. We believe that this new principle can be easily employed in different inorganic materials systems as well so that the power-generating decorative panels can be applied widely.

For electric power-generation purpose of photovoltaic (PV) cells, power conversion efficiency is another very important feature along with various applications that we introduced in the previous chapter. In order to address high power efficiency, in Chapter 5, we studied the undoped a-Si hybrid PVs with improved light absorption by the silica nanoparticles (NPs) embedded indium-tin oxide (ITO) substrates. By optimizing

the NPs concentration before solution casting, we have improved $J_{sc}$ by ~15 % over the hybrid cell on flat ITO/glass substrate. The external quantum efficiency (EQE) characteristics and their comparison to the light transmittance through the NPs embedded and flat ITO substrates empirically support the light absorption increase in undoped a-Si photoactive layer. The NPs embedded scattering surface morphology was measured by atomic force microscopy (AFM). As another way to create light scattering on the a-Si hybrid cells, we employed commercial Al-foil, which has the matte look surface on its backside. The rough surface was characterized by three-dimensional measuring laser microscopy as well as AFM. The Al-foil surface could be patterned on ITO substrate after Al-foil substrate is etched. As a result, the Al-foil based hybrid cell attained around 14 $mA/cm^2$ of $J_{sc}$, thereby achieving over 6 % power efficiency with 100 nm a-Si layer, which was about 30 % improvement compared to the cell on a flat glass substrate. We suggest that proposed intrinsic a-Si hybrid cells are beneficial for utilizing light scattering effect for enhanced a-Si light absorption, consequently leading to higher power conversion efficiency.

Besides phovoltaic cells, we also introduced various other potential applications by ultra-thin a-Si hybrid devices. In Chapter 6, we demonstrated the photo-detector arrays built with undoped a-Si hybrid structures, incorporating crossbar type cathode and anode. By utilizing fast photo-response under 1 μsec in the rise and fall time, we were able to run real-time photo-sensing by over 700 frames/sec with 4 by 4 a-Si hybrid photo-detector arrays. In addition, the a-Si hybrid cells also have benefits in the suppressed dark current density, below 4 $nA/cm^2$, which is quite comparable to crystalline silicon

photodiode. As both anode and cathode can be designed as transparent electrodes, we implemented human touch interactive screen panels as well. With the photo sensitivity of 50 mA/W, the transparent a-Si hybrid photo-detectors showed around 15 % current density variation when a finger approaches so that we can detect the finger touch point. In addition, attributed to the strong ultraviolet (UV) absorption by a-Si, the transparent a-Si hybrid cells can be also applied to UV light-blocking windows with 70 % transmittance, providing 3 $W/m^2$ electric power.

For a future plan, we will study and implement field programmable gate arrays (FPGAs) for undoped a-Si hybrid photo-detector arrays to further improve the real-time photo-sensing capability in higher resolution. Since the FPGAs are equipped with central processing unit (CPU) and input/output peripherals, the computing power, supporting the hybrid photo-detector arrays, will be much enhanced. Also, with the larger number of pixels for higher resolution, we can demonstrate the potential feasibility of the a-Si hybrid high-speed photo-detector arrays for the flat panel detectors (FPDs) in various photo-imaging applications. At last, but not least, intrinsic a-Si quality should be improved further to aim 10 % power conversion efficiency by the proposed a-Si hybrid solar cells, which will lead to satisfy the needs of higher efficiency thin-film photovoltaics.